



Design, Simulation, and Control of a Multicopter Prototyping Platform

DIPLOMA THESIS

Conducted in partial fulfillment of the requirements for the degree of a
Diplom-Ingenieur (Dipl.-Ing.)

supervised by

Univ.-Prof. Dr. techn. A. Kugi
Dipl.-Ing. F. Schausberger
Dipl.-Ing. P. Zips

submitted at the

Vienna University of Technology
Faculty of Electrical Engineering and Information Technology
Automation and Control Institute

by

Michael Buder
Matriculation number 0826581
Blechturmstraße 11/9
1050 Vienna

Vienna, April 2015

Preamble

This diploma thesis with the title *Design, Simulation, and Control of a Multicopter Prototyping Platform* was conducted at the Automation and Control Institute of Vienna University of Technology.

I would like to express my gratitude to my supervisors Dipl.-Ing. Florian Schausberger and Dipl.-Ing. Patrik Zips for their help with words and deeds and I want to thank Univ.-Prof. Dr. techn. Andreas Kugi and all other members of the institute who made this work possible. Further, I want to thank my dear friend Christoph Fröhlich for proofreading this thesis.

Finally, I want to give special thanks to my parents and family who always supported me during my entire studies and to everybody who encouraged and assisted me in this time.

Vienna, April 2015

Abstract

This thesis deals with the design, simulation, and control of a multicopter prototyping platform. In the scope of the work, a multicopter platform based on the commercial available *Mikrokopter Hexa XL* is developed. The multicopter platform is equipped with a computing platform that allows model-based development supported by MATLAB/SIMULINK and a microcontroller board for data collection of the sensor signals. The multicopter platform uses ultrasonic sensors to measure its position in space and an inertial measurement unit for determining its attitude. For the simulation and the model-based control design, a mathematical model of the multicopter platform is formulated. Based on Newton's second law, the dynamical equations of the multicopter are derived. As external forces acting on the multicopter the rotor forces, the gravity, and secondary aerodynamic and gyroscopic effects are considered. Further, a model-based control strategy for position control is derived. As the multicopter is an under-actuated mechanical system, a hierarchical control strategy is used for stabilizing the position at a desired reference trajectory. The control concept consists of an inner attitude controller based on a backstepping approach and an outer position control based on a flatness-based exact feedforward linearisation. Further, two different approaches for state estimation are discussed. The first one uses direct measurements in combination with complementary filters. The second one is based on an extended Kalman Filter.

Kurzzusammenfassung

In dieser Diplomarbeit wird die Entwicklung, Simulation und Regelung eines Multikopters für Testzwecke behandelt. Im Zuge der Arbeit wurde eine Testplattform entwickelt, die auf dem kommerziell erhältlichen Mikrokoopter Hexa XL aufbaut. Die Testplattform ist mit einem Rechner ausgestattet, der eine modellbasierte Entwicklung mit MATLAB/SIMULINK unterstützt, und einer Mikrokontrollerschaltung für die Bereitstellung der Messdaten. Die Testplattform verwendet Ultraschallsensoren für die Positionsbestimmung und einen Inertialsensor für die Bestimmung der Orientierung. Für die Simulation und die modellbasierte Regelung wird ein mathematisches Modell erstellt. Basierend auf dem Impulserhaltungssatz werden die dynamischen Bewegungsgleichungen für den Multikopter hergeleitet. Dafür wird der Multikopter als Starrkörper modelliert. Als externe Kräfte, die auf den Starrkörper wirken, werden die Kräfte der Rotoren und Kräfte, die durch aerodynamische und gyroskopische Effekte hervorgerufen werden, berücksichtigt. Des Weiteren wird eine modellbasierte Regelungsstrategie für die Positionsregelung hergeleitet. Da der Multikopter unteraktuiert ist, wird eine hierarchische Reglerstruktur für die Positionsregelung verwendet. Die Regelung ist aufgeteilt in einen unterlagerten Orientierungsregelkreis basierend auf dem Backstepping Prinzip und einen übergeordneten Positionsregler basierend auf einer flachheitsbasierten Steuerung, der das System um eine Solltrajektorie der Position stabilisiert. Des Weiteren werden zwei verschiedene Methoden zur Ermittlung der Systemzustände vorgestellt. Die erste Methode verwendet direkt Zustandsmessungen in Kombination mit Komplementärfilter. Die zweite Methode basiert auf dem Entwurf eines Extended Kalman Filters als vollständigen Zustandsbeobachter.

Contents

1	Introduction	1
2	Physical setup	3
2.1	Comparison of available platforms	4
2.1.1	Hovering platforms	4
2.1.2	Computing platforms	5
2.1.3	Comparison	7
2.2	Mechanical setup	8
2.3	Electronic flight system	9
2.3.1	Sensor and Interface Board	10
2.3.2	Emergency switch	15
3	Modeling	17
3.1	Hexacopter dynamics	17
3.2	External forces	21
3.2.1	Rotor force model	21
3.2.2	Secondary forces	25
3.3	Complete model	27
3.4	Parameter identification	27
3.4.1	Rotor force model	28
3.4.2	Mechanical parameters	29
4	Control	31
4.1	State estimation	32
4.1.1	Measurements	32
4.1.2	Complementary filter	34
4.1.3	Extended Kalman Filter	36
4.2	Set point value filter	40
4.3	Attitude control	40
4.4	Position control	45
5	Simulation studies and experimental validation	50
5.1	Extended Kalman filter	50
5.2	Attitude control	53
5.3	Position control	57
6	Summary and Outlook	59

A Additional tables

List of Figures

2.1	Illustration of the autopilot used by Ascenting Technologies, showing the task separation of the LLP and the HLP [15].	4
2.2	Interaction of SIMULINK with the executable running on the target hardware [16].	6
2.3	Picture of the Hexacopter flight platform showing position and mounting of the different components.	8
2.4	Overview of the electronic flight system showing all involved components and their connectivity.	9
2.5	Schematic illustration of the Sensor and Interface Board.	11
2.6	Circuit detail C1: battery voltage preparation for analog sensing.	12
2.7	Circuit detail C2: connection of multiple ultrasonic sensors to one bus signal.	13
2.8	Timing of the ultrasonic sensors trigger to avoid multiple access on the serial bus and assignment of the time slots to the corresponding sensors.	14
2.9	Timing and channel assignment for a Pulse Position Modulation signal.	15
2.10	Picture of the emergency switch connected to the Handset via a cable to allow instant use.	16
2.11	Illustration of the emergency switch circuit.	16
3.1	Schematic Hexacopter model illustrating the position and relation of the inertial coordinate frame to the body-fixed frame.	17
3.2	Illustration of ZYX-Euler angles by sequentially performing intrinsic rotations.	18
3.3	DC motor model.	22
3.4	Illustration of the induced drag.	26
3.5	Test setup to obtain measurement data for the static rotor force model.	28
3.6	Identified characteristics for the rotor force.	30
3.7	CAD drawing of the Hexacopter.	30
4.1	Overview of the applied control strategy.	31
4.2	Placement of the ultrasonic sensors and the relation between the measurements and the position of the Center of Mass (CM).	33
4.3	Bode diagram illustrating the complementary filter condition (4.6).	35
4.4	Linear control of the vertical subsystem.	48
4.5	Linear control of the horizontal subsystem.	49
5.1	Estimated states of the Extended Kalman Filter (EKF) in comparison to the real states.	52
5.2	Illustration of the estimation errors of the EKF.	53

5.3	Schematic illustration of the test bench used for the attitude control verification.	54
5.4	Step response of the roll angle.	55
5.5	Reference tracking behavior of the roll angle for a chirp signal from 0.1-1.5 Hz.	56
5.6	Safety arrangement for the free-flight experiment.	57
5.7	Results of the free-flight experiment.	58

List of Tables

2.1	Comparison of different commercially available hovering and computing platforms.	7
A.1	List of possible field bus interfaces that are able to connect to the Cube via the Sensor and Interface Board (SIB) and all permanently connected devices.	61
A.2	List of the components on the SIB.	61
A.3	Rotor parameters for the CFK air blade.	62
A.4	Rotor parameters for the PVC air blade.	62
A.5	Mechanical parameters.	62
A.6	Parameters of the Set-point Value Filter (SVF) for the different reference signals of position and attitude control.	62
A.7	Model parameters for the EKF simulation.	63

List of Abbreviations

UAV	Unmanned Aerial Vehicle
HLP	High Level Processor
LLP	Low Level Processor
SLAM	Simultaneous Localization And Mapping
SBC	Single Board Computer
I2C	Inter-Integrated Circuit
SIB	Sensor and Interface Board
IMU	Inertial Measurement Unit
PCB	Printed Circuit Board
PWM	Pulse Width Modulation
EKF	Extended Kalman Filter
CD-EKF	Continuous-Discrete Extended Kalman Filter
PPM	Pulse Position Modulation
BLDC	Brushless Direct Current
DC	Direct Current
ADC	Analog Digital Converter
CM	Center of Mass
SVF	Set-point Value Filter

1 Introduction

Multicopters have been successfully used in many observation applications because of their ability to carry the payload of a camera, to hover stable and to fly dynamic maneuvers. However, in most applications they remain as passive observers. A further step is to use them not only for observation but rather to interact with their environment to perform certain tasks. In general, tasks that need to be performed in exposed places which are difficult to access or at high altitude are time consuming and need additional safety systems, e. g., harness and support systems or ladders. These tasks are generally more dangerous as the risk of an injury increases significantly and therefore causes higher costs. Remote controlled or even autonomous multicopters which are able to carry out these tasks could solve these problems.

The field of multicopters is extensively studied and plenty of literature is available. Mahony et al. present a tutorial introduction to modeling, estimation, and control for multicopters [1]. They model the multicopter as a rigid body with external forces caused by the rotors and secondary aerodynamic forces as disturbances. As control strategy, they propose a linear controller in a hierarchical control structure with a low level attitude control and an outer position control. For state estimation they propose a non-linear complementary filter. Formentin et al. use a similar hierarchical structure but use a position control based on the differential flatness property of the considered system [2]. Madani et al. divide the multicopter model in a full and an under-actuated subsystem and use a backstepping approach to control the entire system without hierarchical structure [3]. State estimation is typically done by means of data fusion. Leishman et al. discuss the role of the horizontal acceleration measurement and how it can be used to improve state estimation by including a drag force in the rigid body model [4].

The free hovering multicopter is extensively studied, but its interaction with the environment is still an open field of research. An early study is the fire fighting robot of Nishi et al. They developed a propeller driven climbing robot that is able to fly to a wall and climb it up to reach the desired destination [5]. However, the ability to fly was only used to reach the wall in short time and as a safety function if the robot falls of the wall. Albers et al. built a quadrocopter that is capable of applying a force to a wall while maintaining flight stability [6]. They use an additional fifth propeller in the rear to produce a horizontal force against the wall. Lee and Ha study the use of a tool which is rigidly attached to a quadrocopter, e. g. a screwdriver [7]. They use the system dynamics to produce the needed force against the wall and the rotational torque for the screwing process. From 2010 - 2013 the research project AIRobots was working on an air born service robot to support human beings at dangerous, not accessible environments. In the course of this project, Forte et al. use impedance control to accomplish operations

requiring physical interaction [8]. Marconi et al. present a summary of the achieved results of the AIRobots project [9].

In the scope of the presented thesis, a rapid prototyping multicopter platform was built with the perspective to use it for environment interaction. A commercial available multicopter was equipped with a sensor board and a computing platform that allows for a model-based design. Further, a model-based control strategy to stabilize the inherent instable system at a desired position trajectory was developed. Therefore, a mathematical model of the multicopter is derived.

This thesis is structured as follows: First, the physical setup of the development platform will be described in Chapter 2. Then, the complete mathematical model of the Unmanned Aerial Vehicle (UAV) will be derived in Chapter 3. The controller and observer design based on a simplified version of the complete mathematical model will be described in Chapter 4. The performance of the controller and observer will be evaluated by means of simulation studies and test scenarios in Chapter 5. Finally, the work will be summarized and an outlook for possible improvements will be given in Chapter 6.

2 Physical setup

This chapter presents the physical setup of the prototyping platform. First, the requirements for the platform will be outlined. Based on these requirements, different commercial available hovering platforms will be compared. Next, the mechanical setup will be presented followed by the electrical setup. The electrical setup consists of a distributed system including a main computer and a microcontroller board for sensor data collection and communication with the actuators.

The developed prototyping platform has to be able to hover stable in an indoor environment at a desired position. It should offer enough thrust for an additional experimental setup. It is meant to be a platform to test different control algorithms for attitude and position control. In a further scope it should be expandable for research work on UAV interacting with its environment. It is planned to test control concepts such as impedance control in order to apply a force to a rigid wall. A possible scenario would be painting a wall while hovering with a paint roller mounted in the front. As a flying vehicle is potential dangerous for surrounding humans it needs a safety feature to shut down the system in case of an emergency. These features result in specific requirements on the platform. First, the multicopter has to be able to carry enough payload for experimental setups and an endeffector to interact with its surroundings. Therefore, an extra payload of at least 600 g is considered. The platform is meant for testing different control strategies including optimization based algorithms. These algorithms require a sufficiently high CPU frequency. A computing platform with a CPU frequency of at least 100 MHz is considered. To avoid limitations in the achievable dynamics caused by low level controller that are not accessible (e.g. a closed attitude control), the platform has to provide direct access to all sensors and actuators. For rapid testing of different control strategies, it is important to have a modular programming interface that allows to exchange modules without influencing the others. The setup has to be able to log flight data for offline processing as well as to transmit and display live data while the system is operating. As the setup is considered for prototyping, common communication interfaces for additional sensors are necessary. Thus, the hovering platform has to have

- a payload > 600 g, and
- non restricted access to sensors and actuators.

The requirements on the computing platform are:

- CPU frequency > 100 MHz
- modular programming interface,

- visualization of flight data,
- logging flight data for offline processing, and
- support of common communication interfaces.

2.1 Comparison of available platforms

In this section, some commercially available platforms will be presented and compared. Their main features will be outlined before the most suitable platform will be chosen in the end.

2.1.1 Hovering platforms

In the following, the commonly used multicopters of *Ascending Technologies*¹ [10–13] and *Mikrokopter*² [14] are compared.

Perhaps the most common multicopter used in research is the *Hummingbird* of Ascending Technologies, but its maximum payload of 200 g is insufficient for our purpose. Thus, another model of Ascending Technologies is considered, the *Pelican*. Its payload is with 650 g sufficiently large. Copters of Ascending Technologies have an accessible auto pilot board as processing unit which is designed for research. It features two processors, one Low Level Processor (LLP) and one High Level Processor (HLP) (see Figure 2.1). The LLP handles all hardware communication and data fusion. Additionally, a feedback controller

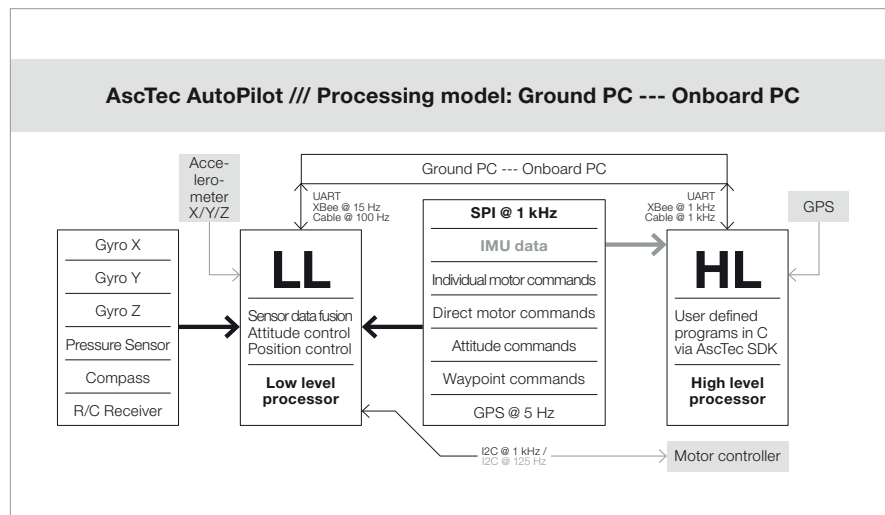


Figure 2.1: Illustration of the autopilot used by Ascending Technologies, showing the task separation of the LLP and the HLP [15].

¹<http://www.asctec.de/asctec-research-line/>

²<http://www.mikrokopter.de/>

is implemented to stabilize the multicopter in an equilibrium. As a safety backup it is always possible to switch back to the LLP in case of an emergency situation [15]. The HLP is free for custom code. This concept allows to send direct motor commands by the HLP or a computing unit connected to HLP's serial interface.

Multicopters from Mikrokopter are originally built for aerial film work, thus designed to lift high payloads. The considered models are the *MK Basicset Quadro XL* and the *MK Basicset Hexa XL*. They are equipped with four and six motor driven rotors, respectively. Each rotor is able to provide $f_{m,max} = 17.5\text{ N}$ thrust (evaluated by measurements), resulting in a total maximal thrust of $f_{t,max} = 70\text{ N}$ for the Quadro XL and $f_{t,max} = 105\text{ N}$ for the Hexa XL. The control variables for a multicopter are its total thrust and the torque around the Center of Mass (CM) produced by the sum of the individual rotor thrusts. For the generation of the maximal control torque, less than half of the thrust should be used for hovering. This leads to a maximum payload of

$$m_{pl} = \frac{f_{t,max}}{2g} - m_e \quad (2.1)$$

where $g = 9.81\text{ m/s}^2$ represents the gravitational acceleration and m_e the empty weight of the multicopter. The empty weight of the Quadro XL is $m_e = 1.7\text{ kg}$ and of the Hexa XL $m_e = 2.2\text{ kg}$. Thus the maximum payload for the Quadro XL is $m_{pl} = 1.87\text{ kg}$ and for the Hexa XL $m_{pl} = 3.15\text{ kg}$. All models of Mikrokopter are equipped with a flight control running on an *AVR* microprocessor. The motor controllers and the flight control are carried out on two different boards connected via an Inter-Integrated Circuit (I2C) bus. This structure allows to directly access the actuators. Thus, the original on-board processing unit can be replaced by a computationally more efficient platform.

2.1.2 Computing platforms

As mentioned before, a modular programming interface is required. This requirement is satisfied by MATLAB/SIMULINK. It allows to implement sensor data processing, actuator excess, and control algorithms in different independent blocksets. The use of SIMULINK also facilitates the approach of model-based design where a physical model of the multicopter is used for simulation to evaluate control strategies. If the controller satisfies the required performance it can be automatically translated in executable code running on the computing platform of the multicopter. In comparison to an approach where the executable code is written separately, it saves time and avoids failures. Further, the use of SIMULINK *external mode*, illustrated in Figure 2.2, satisfies the requirements for logging and online visualization of flight data. SIMULINK external mode uses SIMULINK Coder to generate an executable of the model and link it with I/O drivers provided by Mathworks or the computing platforms manufacturer company. The resulting executable runs on the computing platform under a linux kernel and exchanges data with SIMULINK via a Lan interface.

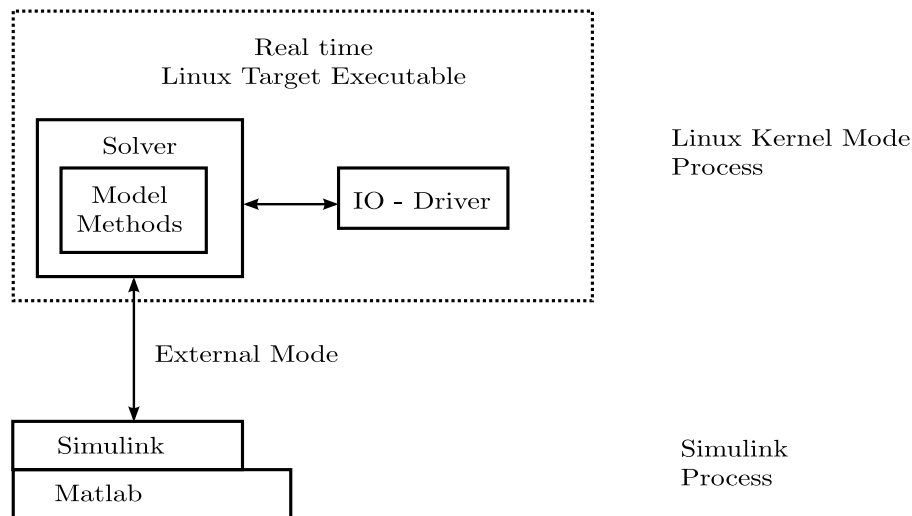


Figure 2.2: Interaction of SIMULINK with the executable running on the target hardware [16].

This allows for:

- *real time signal acquisition*: It is possible to display signals from the real time application while it is running. Signal data is retrieved from the real time application and displayed in the same SIMULINK scope blocks as used for simulating the model.
- *real time parameter tuning*: It is possible to change parameters in the SIMULINK block diagram and have the new parameters passed automatically to the real time application while it is running.
- *offline signal acquisition*: A file with specified variables is generated and saved on the hard disk.

The external mode executable is fully synchronized with a real time clock. All tasks concerning data exchange between the external target and the computing platform are executed with a lower priority. This maintains deterministic real time updates of the main tasks at the selected sampling interval [16].

As described before, a computing platform that supports SIMULINK external mode satisfies the requirements on the programming interface. Most of these platforms are industrial computers in a standard computer housing and are too heavy to be mounted on a hovering platform. The few light weight computing platforms that support SIMULINK external mode will be described in the following. The *Athena 2* Single Board Computer (SBC) of *Diamond Systems* hosts a 800 MHz *VIA Mark* CPU. The concept of a SBC is to gather all functionalities of a computer including power supply, memory and hard disk on a single circuit board without case. This enables the low weight of the *Athena 2* of 150 g. Data exchange is possible via 16 analog inputs, four analog outputs, 24 digital I/O's, and four serial UART interfaces, whereas two of them support 115.2 kBaud and two 460.8 kBaud.

The *Athena 3* features the same functionality as the *Athena 2* with an improved processor, namely the *Intel Atom* 1.6 GHz. However, the *Athena 3* is not supported for SIMULINK external mode yet. It is expected to be released in the near future and is a possible upgrade alternative.

A second light weight computing platform supporting SIMULINK external mode is the *UEISIM 300-1G Cube* of *United Electronic Industries*. It is a small, robust and lightweight industrial computer in a cubic aluminum case hosting a *Freescale 400 MHz* processor. The robust design including the aluminum case leads to a weight of 800 g. For external data exchange it is equipped with four serial RS-485 interfaces supporting a transfer rate up to 1 MBaud each.

2.1.3 Comparison

In the last two sections, different commercially available options for the hovering and computing platform were introduced. In the following, they will be compared and the reason for the chosen setup will be explained. A summary of the features of the discussed hovering and computing platforms is shown in Table 2.1.

	Pelican	Hexa XL	Quadro XL
payload	850 g	3150 g	1870 g
direct motor access	✓	✓	✓
	Cube	Athena 2	Athena 3
CPU Speed	400 MHz	800 MHz	1600 MHz
weight	800 g	150 g	150 g
SIMULINK external mode support	✓	✓	out soon
modular programming interface	✓	✓	✗
visualization of flight data	✓	✓	✗
data logging	✓	✓	✗
communication interfaces	4 x UART	4 x UART 24 x GPIO 4 x Analog In 16 x Analog In	4 x UART 24 x GPIO 4 x Analog In 16 x Analog In

Table 2.1: Comparison of different commercially available hovering and computing platforms.

All presented hovering platforms fulfill the requirement for direct motor access. The main difference between them is their maximal payload. The Pelican of Ascending Technologies is limited to a payload of 650 g, whereas Mikrokopters multicopters are able to lift up to three times more. Another difference is the number of rotors used. The Hexa XL offers six rotors whereas the others use just four. The use of six rotors adds additional degrees of freedom for producing the four control inputs, namely the total thrust and the

torques around the three orthogonal body-frame axes. This additional degrees of freedom can be used in fault scenarios, i. e., when one motor stops working the Hexa XL can still be stabilized. Thus, the Hexa XL, in the remaining text referred to as *Hexacopter*, is chosen as hovering platform.

The UEISIM 300-1G Cube and the Athena 2 board support both the SIMULINK external mode and therefore satisfy the requirements on the programming and debugging interface. The Athena 2 offers a faster processor at a lower weight. However, it is difficult to get hold of it as it is already replaced by its successor, the Athena 3. As this newer platform does not support SIMULINK external mode so far, the UEISIM 300-1G Cube is chosen as main computing platform. In the remaining text it is referred to as *Cube*. The Athena 3 board is included in the comparison as it represent a possible upgrade as soon as SIMULINK external mode support is provided.

2.2 Mechanical setup

A multicopter consists of a frame of star-shaped booms holding motor driven rotors on their ends and a set of electronics, which gather sensor information and perform a control algorithm that stabilizes its flight. The complete setup of the Hexacopter is shown in Figure 2.3. The frame of the original Hexacopter is extended by a safety cage. This safety cage prevents the rotors to touch the surroundings when operating in close proximity

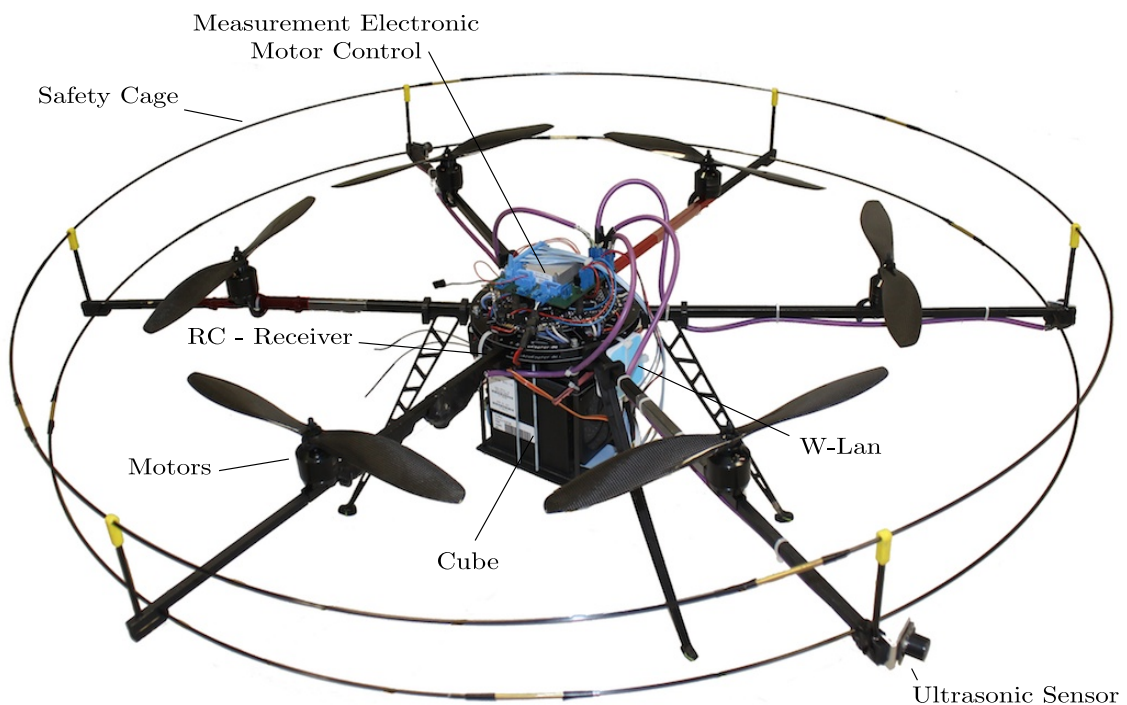


Figure 2.3: Picture of the Hexacopter flight platform showing position and mounting of the different components.

to objects. The flying configuration is chosen in a way that the red boom marks the front of the Hexacopter. Ultrasonic sensors are placed on some booms to determine the position and the orientation around the horizontal axis of the Hexacopter. The position and alignment of the ultrasonic sensors is discussed later in Section 4.1. The Cube is mounted in a sandwich construction below the battery. It allows to remove the case of the Cube to save weight for applications that require higher payload. Above the battery, the original motor controller board is located. A measurement electronic board containing the Inertial Measurement Unit (IMU) is placed on vibration damping elements on top of the motor controller board. A W-Lan access point and a RC-receiver are mounted on the side of the setup.

2.3 Electronic flight system

The electronic flight system, illustrated in Figure 2.4, is a distributed system communicating via different interfaces. Core of the setup is the Cube that performs flow control, feedback control, and sensor fusion. An interface board hosting a microcontroller serves as a gateway between the Cube and all sensors and actuators. The interface board collects all available data of the connected periphery and provides it to the Cube on request. Communication to the base station is possible via two ways. First, SIMULINK external mode is executed via a W-Lan bridge. Second user defined inputs are possible via a radio control handset. As a flying vehicle is potential dangerous for surrounding

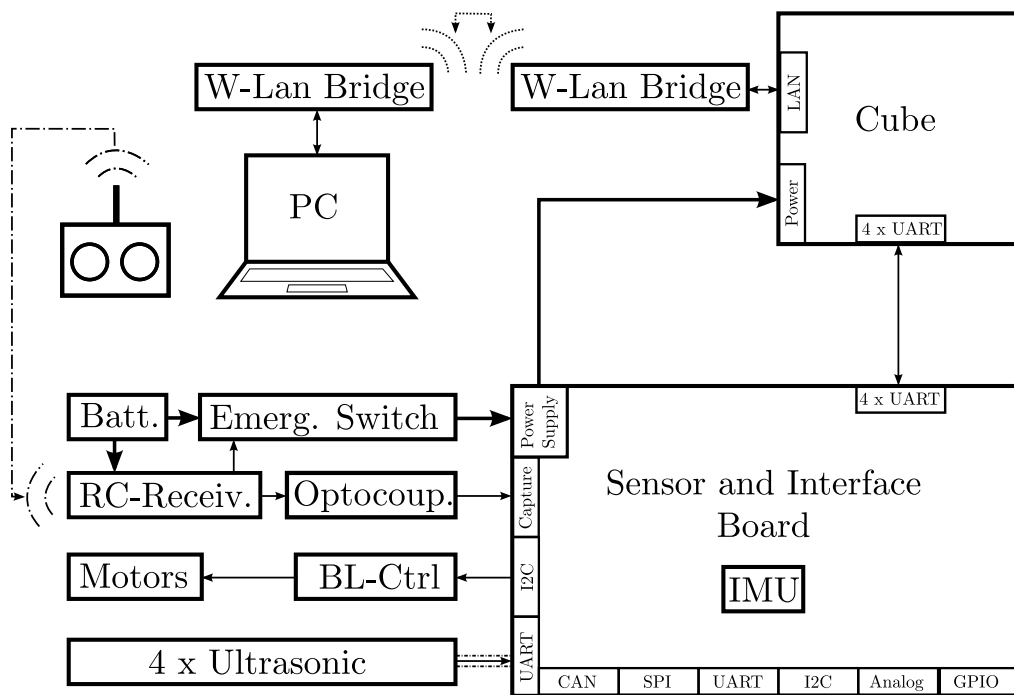


Figure 2.4: Overview of the electronic flight system showing all involved components and their connectivity.

humans, an emergency switch is provided to immediately disconnect the whole electrical system from its power supply. In the following, the components are discussed in more detail.

2.3.1 Sensor and Interface Board

The Sensor and Interface Board (SIB) serves as gateway for the Cube to all sensors and actuators. Focus of the board design was the possibility to expand the system with additional sensors. In its basic configuration it hosts four ultrasonic sensors and an IMU, which includes a 3-axis accelerometer and a 3-axis gyroscope. Further, the SIB handles the communication to the motor controller board and the radio control. It is operating in an environment with electromagnetic noise caused by switching of high currents for the motors. This induces high changing rates of magnetic flux and therefore induction of interference voltages have to be avoided. For this reason, the SIB is built on a 4-layer Printed Circuit Board (PCB), where one of the two middle layers is an uninterrupted ground plane. This acts as an electromagnetic shield and suppresses unwanted coupling of inducted interference voltages. The second middle layer is used as a supply layer with the most used voltage level $V_{DD} = 3.3\text{ V}$. The two outer planes are used for signal routing.

Figure 2.5 shows a schematic illustration of the SIB where the components are labeled according to their functionality. U1 represents the microcontroller with its used communication interfaces. It is possible to program it via the debug adapter *PICkit 3* of *Microchip*. The IMU U2 is directly placed on the SIB and is connected via SPI to the microcontroller. Power supply is provided by the two DC/DC converters U6 and U7. They convert the variable battery voltage to V_{DD} for the supply of the main electronic and $V_5 = 5\text{ V}$ for the supply of the W-Lan Bridge. Communication between the Cube and any other peripheral device takes place via four serial RS-485 interfaces. RS-485 is an industrial standard that specifies the electrical characteristics of a serial data transmission. It uses differential signals to suppress common-mode interferences. This enables high data transmissions up to 16 Mbps. To convert the differential signals into logical signals between V_{DD} and 0 V the four line transceivers U4.1 - U4.4 are used. Two of the Cubes serial interfaces are directly connected to the microcontroller to handle communication between the Cube and the microcontroller. The remaining two are free for further use, whereas one of them can be connected to the I2C master controller U3 via the jumper J1. The I2C master controller is designed to serve as a gateway between the serial interface of the Cube and an I2C bus so that the Cube is able to directly communicate with I2C devices. The board is equipped with one LED L1 to indicate internal states. U5 is a comparator which is used for signal conditioning of the RC-receiver signal. In Appendix A, Table A.1 presents a list of all possible field bus interfaces that are able to connect to the Cube via the SIB and all permanently connected devices. Table A.2 presents a list of all used components.

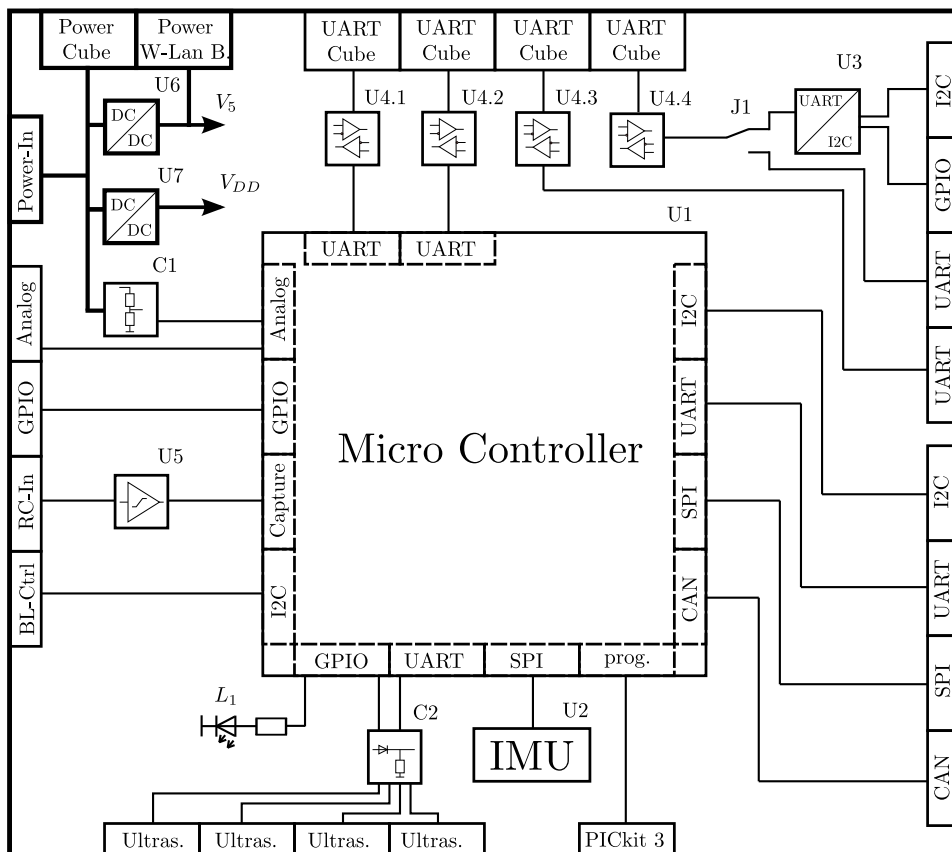


Figure 2.5: Schematic illustration of the Sensor and Interface Board.

The circuit C1, shown in Figure 2.6, is used for measuring the battery voltage. It adapts the battery voltage level (13 V - 16.8 V) to the voltage level of the microcontrollers analog input (0 V - V_{DD}). This is done by the simple voltage divider carried out by the two resistors R_1 and R_2 . To improve the achieved resolution, a Z-Diode D_1 is connected in serial to subtract an offset of the measured voltage and as a consequence increase the used measurement range of the microcontrollers analog input. The measured battery voltage is given by

$$U_{batt} = bU_{adc} + U_{D_1} , \quad (2.2)$$

where U_{adc} is the measured integer value of the Analog Digital Converter (ADC) and $U_{D_1} = 7.56$ V is the reverse voltage of the Z-diode. The ADC operates with 12 bit and a reference voltage of V_{DD} so that the gain b is given by

$$b = \frac{V_{DD}}{2^{12}} \frac{R_1 + R_2}{R_2} = 2.3 \cdot 10^{-3} \text{ V/LSB} . \quad (2.3)$$

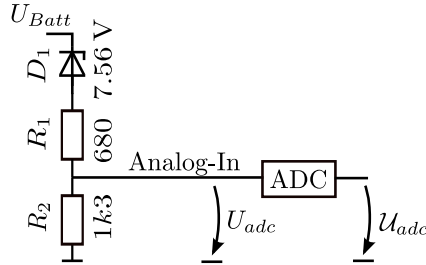


Figure 2.6: Circuit detail C1: battery voltage preparation for analog sensing.

Inertial measurement unit

For determination of the attitude, the IMU *ADIS16480* from *Analog Devices* is used. It includes a 3-axis gyroscope and a 3-axis accelerometer. In addition, it hosts a data processing unit that includes a factory adjusted Extended Kalman Filter (EKF) for attitude estimation in Euler angles. The IMU supports a sample rate up to 2.46 kHz and a high resolution of 32 bit. Readout and configuration takes place via SPI and is built on a register bank orientated structure.

Ultrasonic sensors

The position determination is carried out by measuring the distance to the front wall, the side wall, and the floor with four ultrasonic sensors. The distance to the front wall is measured with two ultrasonic sensors, which are displaced by a fixed distance. This allows to determine the twist around the horizontal axis in addition to the distance to the front wall. The used ultrasonic sensor is the model *HRLV-EZ1* from *MaxSonar*. It features 1 mm resolution at an accuracy of 1%. The range of measurement is between 0.3 m to 5 m with an update rate of 10 Hz. The choice for this sensor is based on the wide sensing range together with the high resolution. Besides, it is light-weighted with only 4 g. Thus,

the asymmetrical mounting does not cause considerable disparity of the weight. Another possibility for range measurement is a laser scanner mounted on the top of the Hexacopter. It can measure the distance to walls in an up to 270° field of view. To this end, it uses several hundreds point measurements with a resolution in the range of mm. The use of a laser scanner requires a location algorithm, such as the Simultaneous Localization And Mapping (SLAM) algorithm, for the determination of the position [17]. In the SLAM algorithm, the location is determined by comparing the current laser scanner reading to a saved map of the surroundings. The advantage of a laser scanner in combination with a location algorithm is that it can be used in more complex environments. Thus, the use of a laser scanner is not restricted to a test scenario with a flat wall to the front and to the side of the Hexacopter. The disadvantage of a laser scanner is that the location algorithm adds more complexity and the processing of several hundreds data points per laser scan adds significant computing effort. However, it is mentioned here as it is a possible upgrade of the Hexacopter's position determination.

The ultrasonic sensors provide their measurement data on a serial interface. Since the microcontroller possesses just four serial interfaces of which two are already in use for the communication with the Cube, all four sensors are combined on one serial bus. This is achieved by the circuit C2 shown in Figure 2.7. It connects the serial interfaces via a diode to a single bus signal. The diode prevents back current to any of the other sensors. The pull down resistor R_3 establishes a low idle state. In this configuration, every sensor is able to set a high voltage level on the bus and is therefore able to send. The circuit realizes a logical *OR* where a simultaneous access of more than one participants leads to a fault and has to be avoided by an appropriate time division bus protocol.

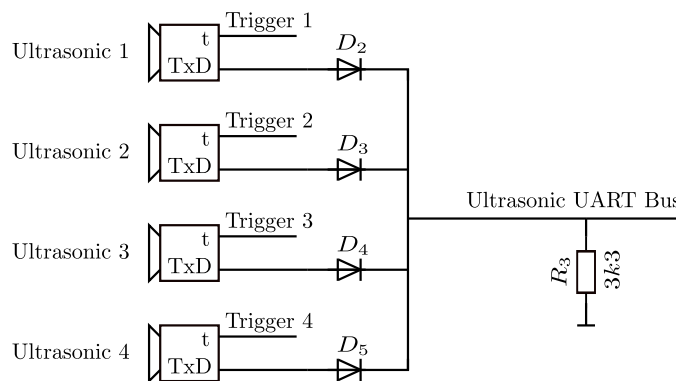


Figure 2.7: Circuit detail C2: connection of multiple ultrasonic sensors to one bus signal.

The measurement timing of one ultrasonic sensor of the type HRLV-EZ1 for a single reading cycle is displayed in the top of Figure 2.8. Measurement data is received in a specified time window between 90 ms - 98 ms after the trigger signal which starts the measurement. To achieve a total sample rate of 10 Hz under consideration that just one sensor can send at a time, a synchronous time division protocol is implemented. Each sensor ① - ④ is triggered displaced by 25 ms. The measurement reading is transmitted in

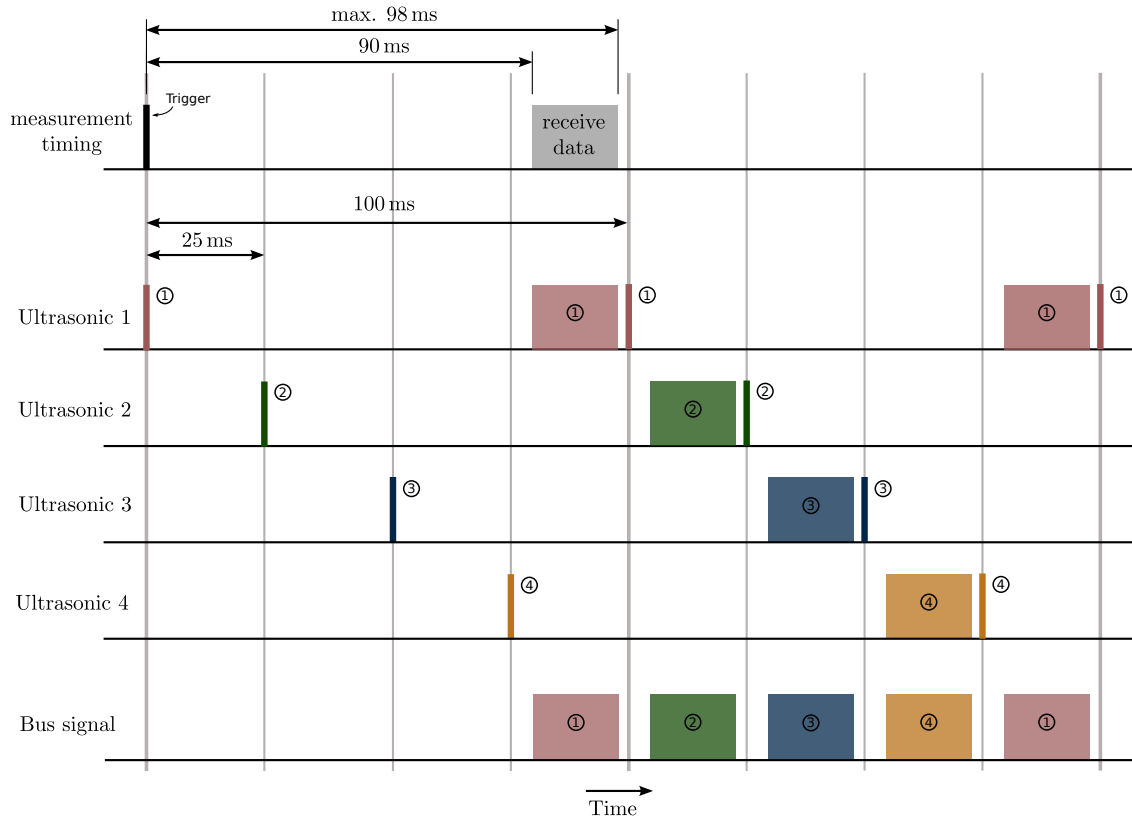


Figure 2.8: Timing of the ultrasonic sensors trigger to avoid multiple access on the serial bus and assignment of the time slots to the corresponding sensors.

the specified time. Thus, each sensor gets a time slot on the bus between 75 ms - 100 ms after it was triggered. This avoids double access of two sensors at a time and allows the assignment of the received measurements to the corresponding sensor.

Driving unit

The rotors are driven by the original motors and motor control of Mikrokopter. The motor controller has no feedback control for setting the rotational speed. The rotational speed is influenced by setting the desired motor control input $S \in [0, 1]$, which is the pulse width of a Pulse Width Modulation (PWM) signal that modulates the battery voltage U_{batt} to an intermediate circuit voltage. The rotational speed of each rotor $i = 1, \dots, 6$ depends on this intermediate circuit voltage. The resulting rotational speed and furthermore the produced rotor thrust

$$f_{m,i} = f(S_i, U_{batt}), \quad i = 1, \dots, 6 \quad (2.4)$$

depends on S_i and U_{batt} . This relation will be further described in a static rotor force model derived in Section 3.2.1.

Communication between the SIB and the motor controllers takes place via the I2C bus. The desired value of the motor control input S_i for each motor is sent as an 11 bit wide integer value and results in

$$\mathcal{S}_i = S_i(2^{11} - 1) . \quad (2.5)$$

Read back values of the motor controllers are status, temperature, rotational speed, current, and voltage of each individual motor. The read back value of the rotational speed offers just 78 increments over the entire rotational speed range. This low resolution makes it impossible to build a low level rotational speed controller without an additional rotational speed sensor.

Radio control

The radio control system consists of the *Graupner MX-20* handset and the *Graupner GR-16 HoTT2.4 GHz 8 Channel* receiver. The handset holds two joysticks and several switches to remotely interact with the Hexacopter. It can be used for manually flying the Hexacopter with the four joysticks and switching between intern states. Further, it is part of a safety system. The receiver provides a Pulse Position Modulation (PPM) signal that enables to read all 16 channels in one signal. The timing of a PPM signal is displayed in Figure 2.9. Information is transmitted in the time difference between two positive edges, which varies between 1 ms and 2 ms. A time difference > 3 ms is used for synchronization and indicates a new data sequence.

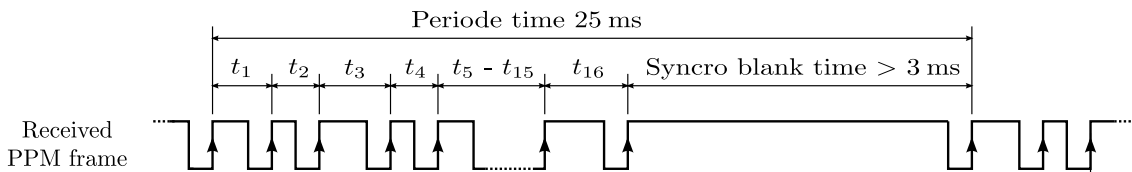


Figure 2.9: Timing and channel assignment for a Pulse Position Modulation signal.

2.3.2 Emergency switch

As already mentioned, the radio control is part of a two level safety system. First, it is possible to remotely deactivate the rotors with a switch on the handset. As this feature is carried out by software it is not reliable. Thus, a hardware emergency switch is implemented as a second safety mechanism. It disconnects all electrical hardware off the battery independently of the microcontroller and the Cube. This emergency shutdown is triggered by a red standard housing emergency switch that is connected to the handset (see Figure 2.10) via cable and allows reliable use in emergency situations.

The emergency switch circuit is illustrated in Figure 2.11. The main power supply of the Hexacopter is conducted via three parallel MOSFETs illustrated as T1. Together they are able to switch off up to 150 A and feature a low on resistance $R_{DS,on} \approx 0.33 \text{ m}\Omega$ that ensures the low maximum ground level voltage lift of 49.9 mV@150 A. The MOSFETs are switched via the inverting gate driver U9 by a standard RC-switch that is connected



Figure 2.10: Picture of the emergency switch connected to the Handset via a cable to allow instant use.

to the RC-receiver. The RC-receiver is powered by the independent DC/DC converter U8 that provides the voltage level $V_{es} = 5\text{ V}$. This independent power supply ensures operation even if all remaining electronics are powered down. As the RC-receiver and the microcontroller are connected to two different ground sources, it is necessary to use an optocoupler for electric-isolated data transmission between them to avoid coupling of unwanted interference voltages. In the default state, when the handset is switched on and the emergency switch is not pushed, the RC-switch is "closed". Hence, the input voltage of the inverting gate driver is low and the common gate voltage of the MOSFETs is set to high. The high gate voltage causes the MOSFETs to connect the SIB to the battery. If the emergency switch is pushed, the RC-switch is "open" and the input voltage of the gate driver is pulled to high. Thus, the MOSFETs disconnect the SIB from the Battery.

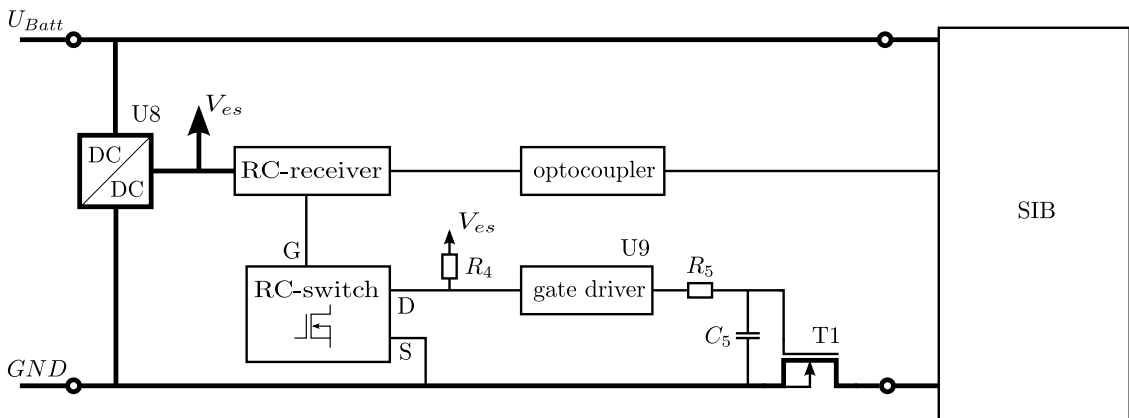


Figure 2.11: Illustration of the emergency switch circuit.

3 Modeling

In the following chapter, a mathematical model of the Hexacopter will be developed. The Hexacopter will be modeled as a rigid body in space with the rotor forces as system inputs. Secondary forces caused by aerodynamic effects and gyroscopic torques of the spinning rotors are modeled as disturbances. A schematic illustration of the Hexacopter model is shown in Figure 3.1. The rotors are located in the height h above the Center of Mass (CM) and in the distance d to the vertical axis. The rotors $i \in \{1, 3, 5\}$ are spinning clockwise, while the rotors $i \in \{2, 4, 6\}$ are spinning counterclockwise. The angle between a rotor and the body frame x -axis $\mathbf{e}_{x,B}$ is expressed by α_i . The distance between the inertial coordinate frame \mathcal{F}_0 and the body-fixed frame \mathcal{F}_B is expressed in the position vector $\mathbf{r} = [r_x \ r_y \ r_z]^T$ where r_x , r_y , and r_z represent the coordinates of the Center of Mass (CM) in \mathcal{F}_0 . In the following, the dynamic equations for position and attitude will be derived based on Newton's second law. Subsequently, a static model for the rotor forces will be presented and the total thrust and torque produced by all rotors derived. The secondary forces, namely the drag effect, the gyroscopic effect, and the ground effect will be modeled as disturbing forces and torques. The dynamic equations together with the external forces of the rotors and disturbances will be assembled to a complete model in form of a single set of differential equations. In the last section of this chapter, unknown parameters will be identified by means of system identification methods and the geometrical parameters will be derived by a CAD tool.

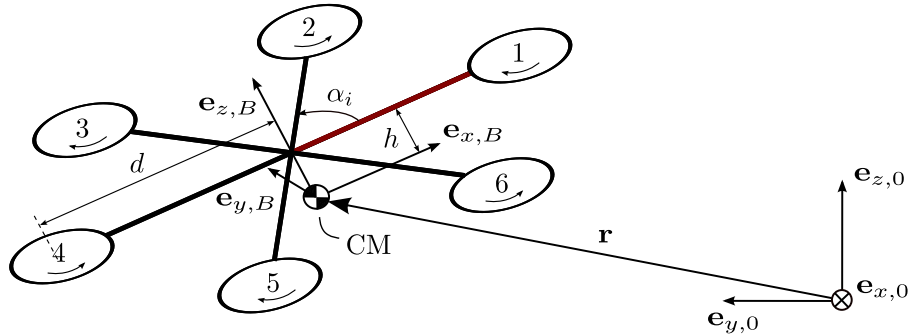


Figure 3.1: Schematic Hexacopter model illustrating the position and relation of the inertial coordinate frame to the body-fixed frame.

3.1 Hexacopter dynamics

The Hexacopter is modeled as rigid body in space. Its kinematics can be described by three degrees of freedom representing the translational motion of the CM to the inertial

coordinate frame \mathcal{F}_0 and three degrees of freedom representing the rotational motion of the body-fixed frame \mathcal{F}_B in relation to \mathcal{F}_0 . The system can be expressed in a nonlinear state space model with twelve state variables and will be derived in the following section.

To this end, the transformation from the inertial frame \mathcal{F}_0 to the body-fixed frame \mathcal{F}_B , where the rotation is represented in the *ZYX-Euler angles*, will be treated first. Let the set of orthogonal unit vectors $\{\mathbf{e}_{x,0}, \mathbf{e}_{y,0}, \mathbf{e}_{z,0}\}$ refer to the inertial frame \mathcal{F}_0 located at a fixed position in the room and its *xy*-plane aligned with the floor. Further, let the set of orthogonal unit vectors $\{\mathbf{e}_{x,B}, \mathbf{e}_{y,B}, \mathbf{e}_{z,B}\}$ refer to the body-fixed frame \mathcal{F}_B located at the Hexacopter's CM with $\mathbf{e}_{x,B}$ aligned with the first motor support boom. The transformation of coordinates from the inertial frame \mathcal{F}_0 to the body-fixed frame \mathcal{F}_B is described by the translational movement \mathbf{r} and the rotation matrix \mathbf{R}_B^0 . Here, the top index of \mathbf{R} denotes the coordinate frame of the origin and the bottom index the coordinate frame of the destination of the rotation. The rotation matrix \mathbf{R}_B^0 is represented by the ZYX-Euler angles (ϕ, θ, ψ) . The ZYX-Euler angles are described by sequentially performing elementary rotations as shown in Figure 3.2.

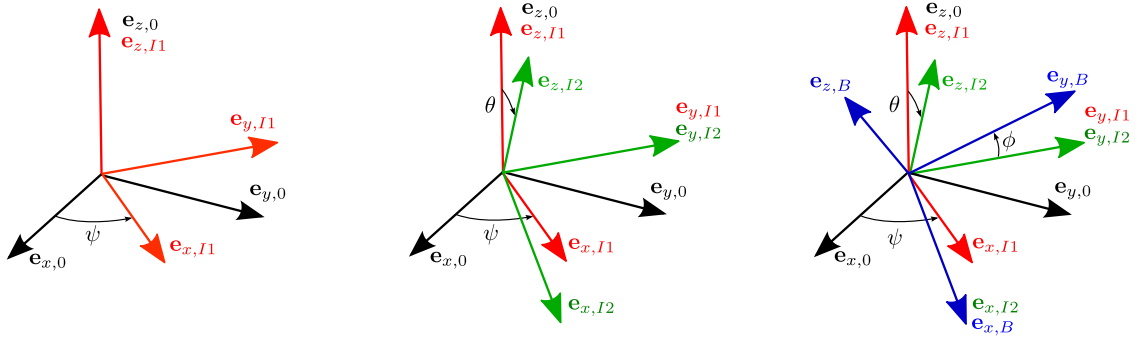


Figure 3.2: Illustration of ZYX-Euler angles by sequentially performing intrinsic rotations.

To this end, the coordinate system of the origin is successive rotated around one axis; first around the *z*-axis, then around the *y*-axis, and at last around the *x*-axis. The used rotations are described by the elementary rotation matrices

$$\mathbf{R}_{I1}^0 = \mathbf{R}_{z,\psi} = \begin{bmatrix} \cos(\psi) & \sin(\psi) & 0 \\ -\sin(\psi) & \cos(\psi) & 0 \\ 0 & 0 & 1 \end{bmatrix} \quad (3.1a)$$

$$\mathbf{R}_{I2}^{I1} = \mathbf{R}_{y,\theta} = \begin{bmatrix} \cos(\theta) & 0 & -\sin(\theta) \\ 0 & 1 & 0 \\ \sin(\theta) & 0 & \cos(\theta) \end{bmatrix} \quad (3.1b)$$

$$\mathbf{R}_B^{I2} = \mathbf{R}_{x,\phi} = \begin{bmatrix} 1 & 0 & 0 \\ 0 & \cos(\phi) & \sin(\phi) \\ 0 & -\sin(\phi) & \cos(\phi) \end{bmatrix}. \quad (3.1c)$$

Here, $\mathbf{R}_{z,\psi}$ describes the rotation of \mathcal{F}_0 by the angle ψ around the *z*-axis into an intermediate frame \mathcal{F}_{I1} , $\mathbf{R}_{y,\theta}$ describes the rotation of \mathcal{F}_{I1} by the angle θ around the *y*-axis into

an intermediate frame \mathcal{F}_{I2} , and $\mathbf{R}_{x,\phi}$ describes the rotation of \mathcal{F}_{I2} by the angle ϕ around the x -axis into the body fixed frame \mathcal{F}_B . Thus, the rotation from the inertial frame \mathcal{F}_0 to the body-fixed frame \mathcal{F}_B is represented by

$$\begin{aligned} \mathbf{R}_B^0 &= \mathbf{R}_{x,\phi} \mathbf{R}_{y,\theta} \mathbf{R}_{z,\psi} = \mathbf{R}_B^{I2} \mathbf{R}_{I2}^{I1} \mathbf{R}_{I1}^0 \\ &= \begin{bmatrix} c_\theta c_\psi & c_\theta s_\psi & -s_\theta \\ s_\phi s_\theta c_\psi - c_\phi s_\psi & s_\phi s_\theta s_\psi + c_\phi c_\psi & s_\phi c_\theta \\ c_\phi s_\theta c_\psi + s_\phi s_\psi & c_\phi s_\theta s_\psi - s_\phi c_\psi & c_\phi c_\theta \end{bmatrix} \end{aligned} \quad (3.2)$$

where, for better readability, the short form $c_\kappa = \cos(\kappa)$ and $s_\kappa = \sin(\kappa)$ is used. The Euler angles ϕ , θ and ψ are further referred to as roll, pitch, and yaw angle and are written together in the vector $\boldsymbol{\phi} = [\phi \ \theta \ \psi]^\top$. The coordinate transformation of a general coordinate vector $\mathbf{q} = [q_x \ q_y \ q_z]^\top$ from the inertial frame \mathcal{F}_0 to the body-fixed frame \mathcal{F}_B results in

$$\mathbf{q}_0 = \mathbf{R}_0^B \mathbf{q}_B + \mathbf{r} \quad (3.3)$$

with the rotation from the body-fixed frame \mathcal{F}_B to the inertial frame \mathcal{F}_0 represented by the matrix

$$\mathbf{R}_0^B = \left(\mathbf{R}_B^0\right)^{-1} = \left(\mathbf{R}_B^0\right)^\top. \quad (3.4)$$

Now, the dynamic equations of motion will be derived. Let $\mathbf{v} = [v_x \ v_y \ v_z]^\top$ be the Hexacopter's velocity in \mathcal{F}_0 and m its constant mass. According to Newton's second law, the change of impulse in the inertial frame \mathcal{F}_0 equals the force acting on the rigid body, i. e.,

$$\left(\frac{d}{dt}\mathbf{p}\right)_{\mathcal{F}_0} = m \frac{d}{dt}\mathbf{v} = \mathbf{f} \quad (3.5)$$

where $\mathbf{p} = m\mathbf{v}$ is the impulse of the Hexacopter and \mathbf{f} is the acting force expressed in \mathcal{F}_0 . Thus, the dynamic equations for the position can be directly written as

$$\dot{\mathbf{r}} = \mathbf{v} \quad (3.6a)$$

$$\dot{\mathbf{v}} = \frac{1}{m} \left(-mg\mathbf{e}_{z,0} + \mathbf{R}_0^B \mathbf{f}_B\right) \quad (3.6b)$$

where $-mg\mathbf{e}_{z,0}$ is the gravitational force and \mathbf{f}_B is a general force acting on the Hexacopter in the body-fixed frame \mathcal{F}_B . The general force \mathbf{f}_B includes the rotor forces and the disturbance forces. Both will be derived in Section 3.2.

Newton's second law for rotation states that the change in angular momentum in the inertial frame \mathcal{F}_0 is equal to the torque acting on the rigid body, i. e.,

$$\left(\frac{d}{dt}\mathbf{l}\right)_{\mathcal{F}_0} = \boldsymbol{\tau} \quad (3.7)$$

where \mathbf{l} represents the angular momentum and $\boldsymbol{\tau}$ the acting torque expressed in \mathcal{F}_0 . Since the angular velocity $\boldsymbol{\omega}_B = [\omega_{x,B} \ \omega_{y,B} \ \omega_{z,B}]^T$ is measured in \mathcal{F}_B , it is useful to transform equation (3.7) to \mathcal{F}_B . Therefore, the transformation for the time derivative of an arbitrary vector \mathbf{j} from the fixed inertial frame \mathcal{F}_0 to the rotating frame \mathcal{F}_B

$$\left(\frac{d}{dt}\mathbf{j}\right)_{\mathcal{F}_0} = \left(\frac{d}{dt}\mathbf{j}\right)_{\mathcal{F}_B} + \boldsymbol{\omega}_B \times \mathbf{j} \quad (3.8)$$

will be used [18]. Applying this transformation to (3.7) and using the angular momentum \mathbf{l}_B expressed in \mathcal{F}_B leads to

$$\left(\frac{d}{dt}\mathbf{l}_B\right)_{\mathcal{F}_B} + \boldsymbol{\omega}_B \times \mathbf{l}_B = \boldsymbol{\tau}_B, \quad (3.9)$$

where $\boldsymbol{\tau}_B$ is a general torque acting on the Hexacopter expressed in \mathcal{F}_B . The general torque $\boldsymbol{\tau}_B$ includes the torque produced by the rotor forces and the torque produced by the disturbance forces and will be derived in Section 3.2.

In the body fixed-frame \mathcal{F}_B , the angular momentum can be expressed as

$$\mathbf{l}_B = \mathbf{I}\boldsymbol{\omega}_B, \quad (3.10)$$

with the constant inertia matrix \mathbf{I} . As the body-fixed frame is located in the CM of the Hexacopter and its axes coincide with the principal axes of inertia, the inertia matrix is a diagonal matrix

$$\mathbf{I} = \begin{bmatrix} I_x & 0 & 0 \\ 0 & I_y & 0 \\ 0 & 0 & I_z \end{bmatrix} \quad (3.11)$$

where I_x , I_y , and I_z represents the inertia around the corresponding axis of \mathcal{F}_B . Using (3.10) in (3.9) yields the so-called *Euler's equations* [19]

$$\mathbf{I}\dot{\boldsymbol{\omega}}_B + \boldsymbol{\omega}_B \times \mathbf{I}\boldsymbol{\omega}_B = \boldsymbol{\tau}_B. \quad (3.12)$$

The rotational subsystem is described by the angular velocity $\boldsymbol{\omega}_B$ in the body-fixed frame \mathcal{F}_B which is directly measured by the gyroscope. Additionally, the change of the ZYX-Euler angles

$$\dot{\boldsymbol{\phi}} = \mathbf{B}\boldsymbol{\omega}_B \quad (3.13)$$

are used. To obtain the relation matrix \mathbf{B} , the rotation of the coordinate frame is investigated in more detail. According to Figure 3.2, every elementary rotation takes place in a different intermediate frame. Thus, the time derivative of the corresponding Euler angles $\dot{\phi}$, $\dot{\theta}$, and $\dot{\psi}$ also have to be rotated from the intermediate frame where they are defined to the body-fixed frame \mathcal{F}_B . To this end, the time derivative of the yaw angle $\dot{\psi}$ is rotated from \mathcal{F}_0 to \mathcal{F}_B , the time derivative of the pitch angle $\dot{\theta}$ is rotated from \mathcal{F}_{I1} to \mathcal{F}_B , and the time derivative of the roll angle $\dot{\phi}$ is rotated from \mathcal{F}_{I2} to \mathcal{F}_B . In the body

fixed frame all rotated time derivatives of ϕ , θ , and ψ can be summed up to the angular velocity

$$\boldsymbol{\omega}_B = \dot{\psi} \mathbf{R}_B^0 \mathbf{e}_{z,0} + \dot{\theta} \mathbf{R}_{I_2}^{I_1} \mathbf{R}_B^{I_2} \mathbf{e}_{y,I_1} + \dot{\phi} \mathbf{R}_B^{I_2} \mathbf{e}_{x,I_2}. \quad (3.14)$$

The relation matrix \mathbf{B} is then given by

$$\mathbf{B} = \left(\frac{\partial \boldsymbol{\omega}_B}{\partial \dot{\boldsymbol{\phi}}} \right)^{-1} = \begin{bmatrix} 1 & \frac{\sin(\theta) \sin(\phi)}{\cos(\theta)} & \frac{\cos(\phi) \sin(\theta)}{\cos(\theta)} \\ 0 & \cos(\phi) & -\sin(\phi) \\ 0 & \frac{\sin(\phi)}{\cos(\theta)} & \frac{\cos(\phi)}{\cos(\theta)} \end{bmatrix}. \quad (3.15)$$

This matrix \mathbf{B} has a singularity at the pitch angle $\theta = \pm 90^\circ$, which corresponds to a sideways attitude of the Hexacopter. In this thesis, no maneuvers leading to such a configuration will be treated and therefore the singularity represents no restriction. However, the singularity can be avoided using a different parametrisation, e. g., with respect to a trajectory, see [20].

Using (3.15), the dynamic equations for the rotation are given by

$$\dot{\boldsymbol{\phi}} = \mathbf{B} \boldsymbol{\omega}_B \quad (3.16a)$$

$$\dot{\boldsymbol{\omega}}_B = \mathbf{I}^{-1} (-\boldsymbol{\omega}_B \times \mathbf{I} \boldsymbol{\omega}_B + \boldsymbol{\tau}_B). \quad (3.16b)$$

3.2 External forces

In the following, the general force \mathbf{f}_B and torque $\boldsymbol{\tau}_B$ will be discussed. Both are composed of the rotor forces and the disturbances. Each rotor is propelled by a Brushless Direct Current (BLDC) motor, which is controlled with the PWM signal S_i , $i = 1, \dots, 6$. To obtain a suitable control input for the feedback controller, a static model of the rotor force $f_{m,i}$ depending on the PWM signal S_i and the battery voltage U_{batt} will be derived. Subsequently, the disturbances will be discussed, which include aerodynamic and gyroscopic effects.

3.2.1 Rotor force model

In the following, the rotor force $f_{m,i}$ for a single motor is derived. For better readability the index i is omitted. The rotors are powered by block commutated sensorless BLDC motors. The BLDC motor is based on a three-phase synchronous motor with permanent magnets. The three-phase windings are supplied by an inverter and produce a rotary field which moves the rotor. The switching of the phases is conducted in a way that it produces the maximum torque. Therefore, the behavior of a BLDC motor is similar to a Direct Current (DC) motor and a DC motor model can be used to describe the motor dynamics (see Figure 3.3). The dynamic equations are given by [21]

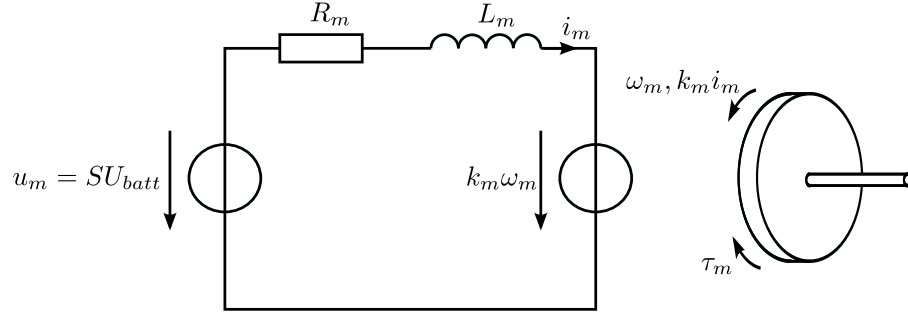


Figure 3.3: DC motor model.

$$\dot{i}_m = \frac{1}{L_m}(-R_m i_m - k_m \omega_m + u_m) \quad (3.17a)$$

$$\dot{\omega}_m = \frac{1}{I_m}(k_m i_m - \tau_m) \quad (3.17b)$$

with the angular velocity ω_m of the motor, the motor current i_m , the inductance L_m and the resistance R_m of the windings, the combined moment of inertia I_m including the rotating part of the motor and the rotor air blade, the motor coefficient k_m , the supply voltage u_m , and the load torque τ_m . For a BLDC motor the supply voltage is produced by the PWM of the battery voltage U_{batt} and reads as

$$u_m = S U_{batt} \quad (3.18)$$

with $S \in [0, 1]$. The steady-state thrust and torque produced by a rotating air plate can be modeled using the momentum theory. The thrust reads as [22, 23]

$$f_m = C_T \rho A_r R_r^2 \omega_m^2 = c_T \omega_m^2, \quad (3.19)$$

where R_r is the air blade radius, A_r the rotor disk area, C_T is a dimensionless rotor thrust coefficient that depends on the air blades geometry, and ρ is the density of air. In practice, a lumped parameter model with $c_T = C_T \rho A_r R_r^2 > 0$ is used. Commonly, c_T is identified by a static thrust test, which will be presented in Section 3.4.1. The reaction torque acting on the motor support is given by [22, 23]

$$\tau_m = C_Q \rho A_r R_r^3 \omega_m^2 = c_Q \omega_m^2, \quad (3.20)$$

with the dimensionless rotor torque coefficient C_Q that depends on the air blades geometry. Again, a lumped parameter $c_Q = C_Q \rho A_r R_r^3 > 0$ is used.

Inserting (3.18) and (3.20) in the motor model (3.17) for the steady-state $\dot{i}_m = 0$ and $\dot{\omega}_m = 0$ leads to the steady-state motor angular velocity

$$\omega_m = -\frac{k_m^2}{2R_m c_Q} \pm \sqrt{\left(\frac{k_m^2}{2R_m c_Q}\right)^2 + \frac{k_m}{R_m c_Q} S U_{batt}}. \quad (3.21)$$

In the following, the positive root of (3.21) will be used as each motor is restricted to spin only in one direction. Thus, it can only produce a positive force in the direction $\mathbf{e}_{z,B}$. Using (3.21) in (3.19) yields the static rotor force model for all rotors $i \in \{1, \dots, 6\}$

$$f_{m,i} = 2a_1^2 - 2a_1\sqrt{a_2S_iU_{batt} + a_1^2} + a_2S_iU_{batt} \quad (3.22)$$

with the coefficients

$$a_1 = \frac{\sqrt{c_T}k_m^2}{2R_m c_Q} \quad (3.23)$$

and

$$a_2 = \frac{c_T k_m}{2R_m c_Q} . \quad (3.24)$$

Rotor forces as input for the rigid body dynamics

The $N = 6$ individual rotor forces $f_{m,i}$, $i \in \{1, \dots, 6\}$ produce a total thrust $\mathbf{f}_{t,B}$ and a total torque $\boldsymbol{\tau}_{t,B}$ acting on the rigid body. As shown in Figure 3.1, the rotors are placed in a star shaped arrangement around the CM and are labeled in anticlockwise direction. Each rotor has a related angle α_i between its supporting air frame boom and the body-fixed x -axis $\mathbf{e}_{x,B}$, which is given by

$$\alpha_i = \frac{2\pi(i-1)}{N} \quad (3.25)$$

for a symmetrical arrangement of the rotors. Further, every rotor is placed in distance d to the vertical axis and height h to the CM. Thus, the position of each rotor i with respect to the CM is expressed by the vector

$$\mathbf{r}_{r,i,B} = \begin{bmatrix} d \cos(\alpha_i) & d \sin(\alpha_i) & h \end{bmatrix}^T . \quad (3.26)$$

Each rotor produces a force $f_{m,i}$ in $\mathbf{e}_{z,B}$ direction. The total thrust is given by the sum of all rotors forces

$$\mathbf{f}_{t,B} = \sum_{i=1}^N f_{m,i} \mathbf{e}_{z,B} . \quad (3.27)$$

Depending on its position $\mathbf{r}_{r,i,B}$ each rotor force $f_{m,i}$ produces a torque around $\mathbf{e}_{x,B}$ and $\mathbf{e}_{y,B}$. This torque can be expressed as the cross product of the rotor position in the body-fixed frame \mathcal{F}_B and the acting rotor force

$$\boldsymbol{\tau}_{m,i,B} = \mathbf{r}_{r,i,B} \times f_{m,i} \mathbf{e}_{z,B} . \quad (3.28)$$

The torque around the axis $\mathbf{e}_{z,B}$ is produced by an imbalance of the reaction torques of the individual rotors. Three rotors are spinning clockwise, while the other three rotors are spinning counterclockwise. Therefore, the rotation direction of the rotor i is defined as

$$\sigma_i = -1^i , \quad (3.29)$$

where $\sigma_i = 1$ corresponds to a counterclockwise and $\sigma_i = -1$ to a clockwise spinning rotor. The torque of a single rotor around $\mathbf{e}_{z,B}$ results in

$$\boldsymbol{\tau}_{c,i,B} = -\sigma_i \tau_{m,i} \mathbf{e}_{z,B}, \quad (3.30)$$

with the rotor reaction torque

$$\tau_{m,i} = \frac{c_Q}{c_T} f_{m,i} \quad (3.31)$$

obtained from (3.19) and (3.20). Thus, the torque produced by each rotor results with (3.28) and (3.30) in

$$\boldsymbol{\tau}_{i,B} = \boldsymbol{\tau}_{m,i,B} + \boldsymbol{\tau}_{c,i,B} = \mathbf{r}_{r,i,B} \times f_{m,i} \mathbf{e}_{z,B} - \sigma_i \tau_{m,i} \mathbf{e}_{z,B}. \quad (3.32)$$

The total torque $\boldsymbol{\tau}_{t,B} = [\tau_{x,B} \ \tau_{y,B} \ \tau_{z,B}]^T$ is composed of the sum of the individual rotor torques

$$\boldsymbol{\tau}_{t,B} = \sum_{i=1}^N \boldsymbol{\tau}_{i,B}. \quad (3.33)$$

The six rotors produce four independent control inputs, namely the torques $\tau_{x,B}$, $\tau_{y,B}$ and $\tau_{z,B}$ around the body-fixed frame axes and the total thrust $f_t = \sum_{i=1}^N f_{m,i}$ acting in the direction of $\mathbf{e}_{z,B}$. For a symmetric arrangement of the six rotors, i. e., $\alpha_i = 60^\circ$ for $i = 1, \dots, 6$, these control inputs can be expressed in the matrix form

$$\begin{bmatrix} f_t \\ \tau_{x,B} \\ \tau_{y,B} \\ \tau_{z,B} \end{bmatrix} = \mathbf{\Gamma} \mathbf{f}_m, \quad (3.34)$$

with the rotor force vector $\mathbf{f}_m = [f_{m,1} \ f_{m,2} \ f_{m,3} \ f_{m,4} \ f_{m,5} \ f_{m,6}]^T$ and the matrix

$$\mathbf{\Gamma} = \begin{bmatrix} 1 & 1 & 1 & 1 & 1 & 1 \\ 0 & d\sqrt{3}/2 & d\sqrt{3}/2 & 0 & -d\sqrt{3}/2 & -d\sqrt{3}/2 \\ -d & -d/2 & d/2 & d & d/2 & -d/2 \\ c_Q/c_T & -c_Q/c_T & c_Q/c_T & -c_Q/c_T & c_Q/c_T & -c_Q/c_T \end{bmatrix}. \quad (3.35)$$

Equation (3.34) is under-determined and has an infinite number of solutions. To obtain a unique solution, the minimization problem

$$\min_{\mathbf{f}_m} \|\mathbf{f}_m\| \quad (3.36)$$

subject to (3.34) is solved. The matrix $\mathbf{\Gamma}$ has full row rank. Thus, $\mathbf{\Gamma}\mathbf{\Gamma}^T$ is invertible and the right inverse $\mathbf{\Gamma}^\dagger$ exists. The closed form solution of (3.36) results in [24]

$$\mathbf{f}_m = \mathbf{\Gamma}^\dagger \begin{bmatrix} f_t \\ \tau_{x,B} \\ \tau_{y,B} \\ \tau_{z,B} \end{bmatrix} \quad (3.37)$$

with the right pseudo inverse

$$\mathbf{\Gamma}^\dagger = \mathbf{\Gamma}^T(\mathbf{\Gamma}\mathbf{\Gamma}^T)^{-1} = \begin{bmatrix} 1/6 & 0 & -1/(3d) & c_T/(6c_Q) \\ 1/6 & \sqrt{3}/(6d) & -1/(6d) & -c_T/(6c_Q) \\ 1/6 & \sqrt{3}/(6d) & 1/(6d) & c_T/(6c_Q) \\ 1/6 & 0 & 1/(3d) & -c_T/(6c_Q) \\ 1/6 & -\sqrt{3}/(6d) & 1/(6d) & c_T/(6c_Q) \\ 1/6 & -\sqrt{3}/(6d) & -1/(6d) & -c_T/(6c_Q) \end{bmatrix}. \quad (3.38)$$

The motor control input S_i , which depends on the required rotor forces $f_{m,i}$, can be obtained by solving (3.22) for S_i yielding

$$S_i = \frac{f_{m,i} + 2a_1\sqrt{f_{m,i}}}{a_2U_{batt}}. \quad (3.39)$$

3.2.2 Secondary forces

In addition to the rotor forces, several other effects act on a propeller lifted motor vehicle. While most of them are negligible for small scale rotor crafts some have to be considered [1], as explained in the following.

Induced drag

The induced drag is a force that opposes the direction of the apparent wind, which is the sum of the true wind and the headwind the Hexacopter would experience in still air. It is caused by the fact that the air blade is not fully rigid. Thus, it experiences different lift depending on its azimuthal position. When a rotor translates through the air, the advancing blade moves in the direction of the translation and produces more lift. The retreating blade moves in the opposite direction of the movement and produces less lift. The imbalance of the produced lift causes the airfoil to bend which results in a force f_d opposite to the apparent wind [25]. In case of indoor flight the true wind is zero. Thus, the apparent wind consists only of the Hexacopter's headwind, which opposes the direction of flight shown in Figure 3.4. The induced drag is modeled as a lumped parameter model similar to the model of the viscous friction. For each rotor i , a force proportional to the velocity opposes the direction of motion

$$\mathbf{f}_{d,i,B} = -\mathbf{D} \underbrace{\mathbf{R}_B^0}_{\mathbf{v}_B} \mathbf{v}, \quad (3.40)$$

with the drag coefficient matrix

$$\mathbf{D} = \begin{bmatrix} \mu_d & 0 & 0 \\ 0 & \mu_d & 0 \\ 0 & 0 & 0 \end{bmatrix}. \quad (3.41)$$

The total drag force results in

$$\mathbf{f}_{d,B} = \sum_{i=1}^N \mathbf{f}_{d,i,B} \quad (3.42)$$

The drag forces act in the plane of the rotors at the height h over the CM. Therefore, they cause a torque

$$\boldsymbol{\tau}_{d,i,B} = \mathbf{r}_{r,i,B} \times \mathbf{f}_{d,i} \quad (3.43a)$$

$$\boldsymbol{\tau}_{d,B} = \sum_{i=1}^N \boldsymbol{\tau}_{d,i,B} , \quad (3.43b)$$

with $\mathbf{r}_{r,i,B}$ from (3.26).

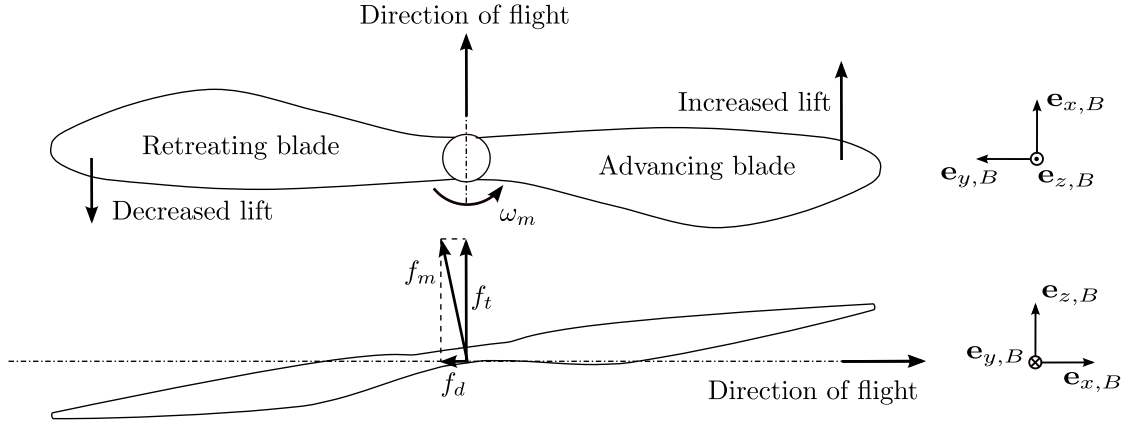


Figure 3.4: Illustration of the induced drag.

Gyroscopic torque of the rotors

The spinning rotors produce a torque that opposes the applied torque $\boldsymbol{\tau}_{t,B}$ due to the gyroscopic effect. Every rotor can be thought as a disk that rotates with the sign true angular speed $\sigma_i \omega_{m,i}$ around $\mathbf{e}_{z,B}$. Its moment of inertia around $\mathbf{e}_{z,B}$ is I_m which yields an angular momentum $\mathbf{l}_{m,i} = I_m \sigma_i \omega_{m,i} \mathbf{e}_{z,B}$. The angular momentum $\mathbf{l}_{m,i}$ is forced to change its direction if an external control torque $\boldsymbol{\tau}_{t,B}$ is applied. According to Newton's second law the torque

$$\boldsymbol{\tau}_{g,i} = \left(\frac{d}{dt} \mathbf{l}_{m,i} \right)_{\mathcal{F}_0} \quad (3.44)$$

is needed to change the direction of the angular momentum $\mathbf{l}_{m,i}$. The rotational frame of the rotors is the body fixed-frame \mathcal{F}_B . Thus, applying (3.8) to (3.44) and rewriting the equation in \mathcal{F}_B leads to the gyroscopic torque

$$\boldsymbol{\tau}_{g,i,B} = \sigma_i I_m (\dot{\omega}_{m,i} \mathbf{e}_{z,B} + \boldsymbol{\omega}_B \times \omega_{m,i} \mathbf{e}_{z,B}) \quad (3.45a)$$

$$\boldsymbol{\tau}_{g,B} = \sum_{i=1}^N \boldsymbol{\tau}_{g,i,B} . \quad (3.45b)$$

The gyroscopic torque $\boldsymbol{\tau}_{g,B}$ opposes the applied torque $\boldsymbol{\tau}_{t,B}$ and is taken into account with a negative sign in the general torque $\boldsymbol{\tau}_B$ acting on the rigid body.

Ground effect

Any propeller lifted aerial vehicle operating close to the ground, i. e., with a height of approximately one rotor diameter or less, experiences a rise in thrust. In momentum theory this is explained by the concept of the induced velocity v_i , which is the velocity of the air that is accelerated by a rotor. In flight conditions with sufficient distance to the floor, the air has enough space to spread. The presence of a ground causes the induced velocity v_i to be zero at the ground. This leads to a higher air pressure and is perceivable in a rise of the thrust factor. The ground effect can be modeled as described in [25, 26]

$$\mathbf{f}_{t,ge,B} = \mathbf{f}_{t,B} \frac{1}{1 - \left(\frac{R_r}{4r_z}\right)^2 \frac{1}{1 + \left(\frac{|\mathbf{v}|}{v_i}\right)^2}}, \quad (3.46)$$

where R_r is again the rotor disc radius, r_z is the height of the Hexacopter and $|\mathbf{v}|$ is the absolute value of the Hexacopter's velocity. For flight maneuvers with low dynamics ($|v_i| \gg |\mathbf{v}|$), the ground effect model (3.46) can be simplified to

$$\mathbf{f}_{t,ge,B} = \mathbf{f}_{t,B} \frac{1}{1 - \left(\frac{R_r}{4r_z}\right)^2}. \quad (3.47)$$

3.3 Complete model

The complete dynamical model, including the rotor force inputs, the drag force, the gyroscopic effect of the rotors and the ground effect, is given by the equations (3.6) and (3.16). Equations (3.6) describe the translational movement, where the general force \mathbf{f}_B is replaced by the sum of the total thrust $\mathbf{f}_{t,ge,B}$ (3.47) and the disturbance $\mathbf{f}_{d,B}$ (3.42). Equations (3.16) describe the rotational motion, where the general torque $\boldsymbol{\tau}_B$ is replaced by the sum of the control torque for the attitude $\boldsymbol{\tau}_{t,B}$ (3.33), the disturbance torque of the drag $\boldsymbol{\tau}_{d,B}$ (3.43b) and the gyroscopic effect $\boldsymbol{\tau}_{g,B}$ (3.45b). This yields the complete model

$$\dot{\mathbf{r}} = \mathbf{v} \quad (3.48a)$$

$$\dot{\mathbf{v}} = \frac{1}{m} \left(-mg\mathbf{e}_{z,0} + \mathbf{R}_0^B (\mathbf{f}_{t,ge,B} + \mathbf{f}_{d,B}) \right) \quad (3.48b)$$

$$\dot{\boldsymbol{\phi}} = \mathbf{B}\boldsymbol{\omega}_B \quad (3.48c)$$

$$\dot{\boldsymbol{\omega}}_B = \mathbf{I}^{-1} (-\boldsymbol{\omega}_B \times \mathbf{I}\boldsymbol{\omega}_B - \boldsymbol{\tau}_{g,B} + \boldsymbol{\tau}_{t,B} + \boldsymbol{\tau}_{d,B}). \quad (3.48d)$$

3.4 Parameter identification

After the mathematical model was established in the previous sections, unknown system parameters have to be determined. The parameters of the rotor force model are identified by means of measurement data, while the geometrical parameters are extracted from a CAD tool.

3.4.1 Rotor force model

In this subsection, the lumped parameters c_T and c_Q of (3.19) and (3.20) will be identified as well as the lumped parameters a_1 and a_2 of the rotor force model (3.22). The identification was carried out for two different air blades. One air blade is made of PVC and the other one is made of CFK. To obtain measurement data for the static rotor force model, a test arrangement was set up where the rotor force is applied to a scale via a lever, see Figure 3.5. The setup allows to measure the rotor force $f_{m,j}$, the motor current $i_{m,j}$, and the motor angular velocity $\omega_{m,j}$ for a motor control input S_j and battery voltage $U_{batt,j}$, with $j = 1, \dots, N_m$ measurements. Again, the index $i = 1, \dots, 6$ for the motor is omitted.

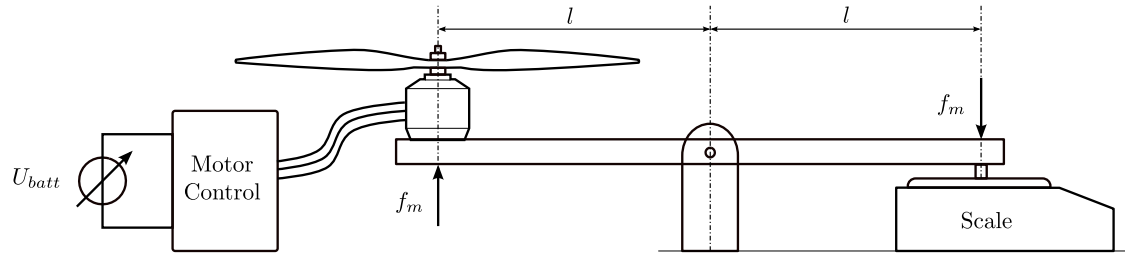


Figure 3.5: Test setup to obtain measurement data for the static rotor force model.

For a model with one parameter

$$\mathbf{b} = a\mathbf{s} , \quad (3.49)$$

the least squares approximation is given by [27]

$$a = (\mathbf{s}^T \mathbf{s})^{-1} \mathbf{s}^T \mathbf{b} . \quad (3.50)$$

Here, a is the unknown parameter, $\mathbf{s} = [s_1 \ \dots \ s_{N_m}]^T$ is the measurement vector for the model input and $\mathbf{b} = [b_1 \ \dots \ b_{N_m}]^T$ is the measurement vector for the model output.

The lumped thrust coefficient c_T can be identified using the least squares method for the rotor thrust equation (3.19). Therefore, the measurement vector for the model input $\mathbf{s} = [\omega_{m,1}^2 \ \dots \ \omega_{m,N_m}^2]^T$ and the measurement vector for the model output $\mathbf{b} = [f_{m,1} \ \dots \ f_{m,N_m}]^T$ is used in (3.50). Figure 3.6(a) shows the identified model (3.19) and the measured data samples of f_m as blue stars. The maximal error between the measurement and the model is 2.1% with respect to the maximum thrust $f_{m,max}$. Thus, the model is a good representation of the reality.

Further, the momentum theory provides a relation between the dimensionless thrust coefficient C_Q of (3.20) and the dimensionless torque coefficient C_T of (3.19) [23]

$$C_Q = C_T \sqrt{\frac{C_T}{2}} . \quad (3.51)$$

Together with (3.19) and (3.20), the relation

$$c_Q = c_T \sqrt{\frac{c_T}{2\rho A_r}} \quad (3.52)$$

is obtained.

To identify a_1 and a_2 of the rotor force model (3.22), a different approach is needed, as it is not a function with linear parameters. The main idea is to find a parameter vector $\mathbf{a} = [a_1 \ a_2]^T$ that minimizes the error $\boldsymbol{\varepsilon}(\mathbf{a}) = [\varepsilon_1(\mathbf{a}) \ \dots \ \varepsilon_{N_m}(\mathbf{a})]^T$ between the measured model output $\mathbf{b} = [f_{m,1} \ \dots \ f_{m,N_m}]^T$ and the simulated model output

$$\mathbf{b}_{model}(\mathbf{a}) = [f_{m,1}(S_1, U_{batt,1}, a_1, a_2) \ \dots \ f_{t,N_m}(S_{N_m}, U_{batt,N_m}, a_1, a_2)]^T, \quad (3.53)$$

with $f_{m,j}$ according to (3.22). Therefore, the quadratic cost function

$$J(\mathbf{a}) = \sum_{j=1}^{N_m} \varepsilon_j^2(\mathbf{a}), \quad (3.54)$$

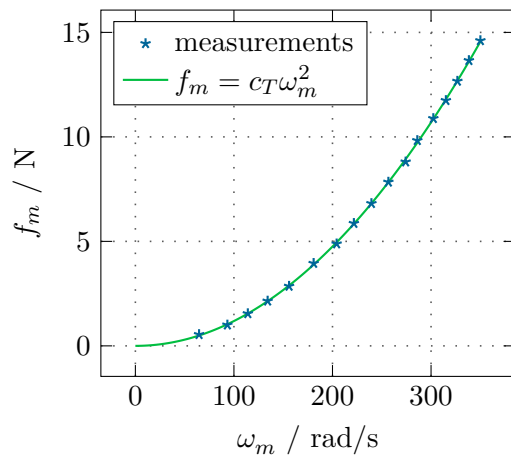
with the error

$$\varepsilon_j(\mathbf{a}) = f_{m,j} - (2a_1^2 - 2a_1 \sqrt{a_2 S_j U_{batt,j} + a_1^2} + a_2 S_j U_{batt,j}) \quad (3.55)$$

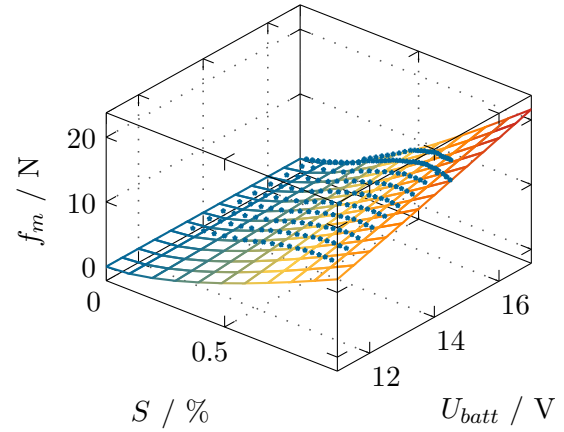
is minimized with respect to \mathbf{a} . The minimization problem was solved with the trust region optimization method of MATLAB. Figure 3.6(b) shows the identified rotor force model (3.22) for the PVC rotor blade where the measured data samples of f_m are plotted as blue stars. The maximal error between the measurement and the model is 2.2% with respect to the maximum thrust $f_{m,max}$. Again, the model is a good approximation of the reality. Table A.3 and Table A.4 in Appendix A present a list of all rotor parameters for the CFK air blade and the PVC air blade, respectively.

3.4.2 Mechanical parameters

The mechanical parameters, namely the position of the CM and the moment of inertia \mathbf{I} , are identified using a CAD tool. A CAD drawing of the Hexacopter was constructed in *Solid Edge*. Defining all parts with their dimensions and physical properties, Solid Edge is able to calculate the position of the CM and the moment of inertia of the Hexacopter. To achieve a high accuracy, most parts of the Hexacopter were disassembled and weighted. Because a uniform density of mass of each part is used, there will be a certain deviation from reality. Nevertheless, the spatial distribution of the parts in the assembly drawing is accurate and therefore the inhomogeneous mass distribution over the whole Hexacopter is reproduced in a sufficiently accurate manner. Thus, the position of the CM and the moment of inertia \mathbf{I} is supposed to be an accurate representation of the real values. Figure 3.7(a) shows a rendering of the assembly drawing and Figure 3.7(b) depicts the position of the body frame \mathcal{F}_B . It is located in the center of rotation around the vertical axis and in a distance $h_s = 27.7$ mm under the bottom plane of the motor support booms. Table A.5 in Appendix A presents a list of all mechanical parameters.

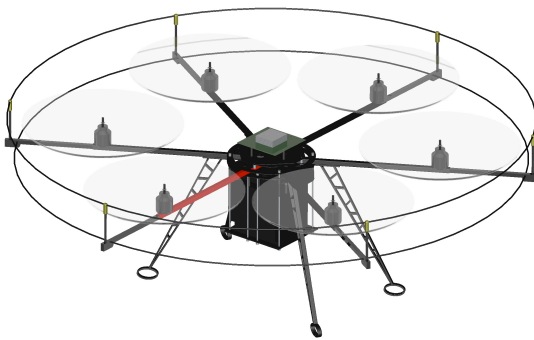


(a) Rotor force f_m depending on ω_m in comparison to the measurement.

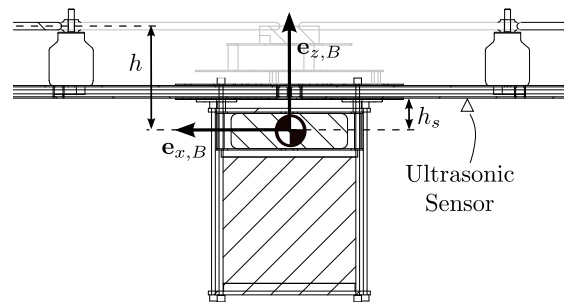


(b) Rotor force f_m (3.22) depending on the motor control input S and the battery voltage U_{batt} in comparison to the measurement.

Figure 3.6: Identified characteristics for the rotor force.



(a) Rendering of the assembly drawing

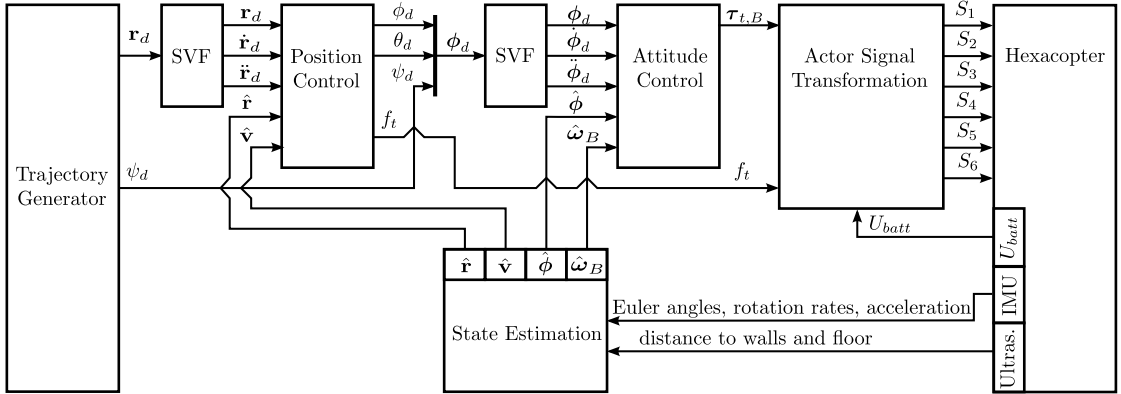


(b) Detail cut showing the position of the construction frame and the CM

Figure 3.7: CAD drawing of the Hexacopter.

4 Control

In this chapter, a control strategy to stabilize the Hexacopter at a desired position trajectory $\mathbf{r}_d(t) = [r_{x,d}(t) \ r_{y,d}(t) \ r_{z,d}(t)]^T$ in space will be derived. The strategy is based on an outer position control with an inner attitude control as shown in Figure 4.1. The system (3.48) is under-actuated, resulting in no direct system input for the position in the xy -plane. An acceleration in the xy -plane is only possible if the Hexacopter tilts. This is considered by a position control, which sets the total thrust f_t and the desired roll angle ϕ_d and pitch angle θ_d for the underlying attitude control. The desired yaw angle ψ_d for the attitude control is set directly by the trajectory generator. The position and attitude control require the first two derivatives of their reference signals, which is provided by a linear Set-point Value Filter (SVF). The rotational subsystem (3.48c) - (3.48d) is fully actuated and stabilization at the desired attitude trajectory $\phi_d(t) = [\phi_d(t) \ \theta_d(t) \ \psi_d(t)]^T$ is done by the underlying attitude control that uses the torque $\tau_{t,B}$ as control variable. The requested control variables $\tau_{t,B}$ and f_t are then transformed into the individual motor control inputs S_i for the motors $i \in \{1, \dots, 6\}$ using (3.37) and (3.39) with the measured battery voltage U_{batt} . The required state information is obtained using measurements from the ultrasonic sensors and the IMU. Therefore, two different approaches for state estimation will be applied. The estimated states are the position $\hat{\mathbf{r}}$, the velocity $\hat{\mathbf{v}}$, the ZYX-Euler angles $\hat{\phi}$, and the angular velocity $\hat{\omega}_B$. The two state estimation approaches will be described first, followed by the linear SVF, and the design of the attitude and position control.



SVF ... Setpoint Value Filter

Figure 4.1: Overview of the applied control strategy.

4.1 State estimation

For the state estimation, two different approaches will be employed. First, a simple approach which uses direct measurement data in combination with a complementary filter for some crucial states is presented. This direct approach has the advantage of only a few tunable parameters. It is used in a first step to gather flight data and test the control strategy. The recorded flight data can then be used to tune a more advanced state estimation strategy, namely an Extended Kalman Filter (EKF). The EKF fuses all available information of the sensors under the consideration of the dynamical model. Before the two different state estimation approaches will be discussed the relation of the distance measurement to the Hexacopter's position and rotation around the vertical axis will be derived, and the use of the IMU-intern EKF will be described.

4.1.1 Measurements

For measuring the pose and the attitude of the Hexacopter, four ultrasonic sensors and an IMU are available. The ultrasonic sensors measure the distance to the front wall, to the side wall and to the floor as shown in Figure 4.2. Sensor ① and ② point forward and measure the distance to the front wall. They are mounted on the second and sixth motor support boom. Sensor ③ points to the right and measures the distance to the side wall. It is mounted on the fourth motor support boom. Sensor ④ points downward and measures the distance to the floor. The motor supporting booms are mounted in an angle α_i , $i \in \{1, \dots, 6\}$ to the $\mathbf{e}_{x,B}$ axis. The sensors measuring the range to the adjacent walls are mounted in a distance d_s to the CM and the sensor measuring the distance to the floor is mounted in a height h_s to the CM. In general, ultrasonic sensors measure the shortest distance to an object in their field of view. Thus, the measured position of the Hexacopter's CM in relation to the inertial frame \mathcal{F}_0 results in

$$r_{x,u} = -\frac{s_1 + s_2 + d_s(\cos(\alpha_2 + \psi_u) + \cos(\alpha_6 + \psi_u))}{2} \quad (4.1a)$$

$$r_{y,u} = (s_3 - d_s \sin(\alpha_5 + \psi_u)) \quad (4.1b)$$

$$r_{z,u} = (s_4 - h_s) , \quad (4.1c)$$

where the tuple $(r_{x,u}, r_{y,u}, r_{z,u})$ denotes the measured position of the CM in \mathcal{F}_0 and ψ_u the measured yaw angle. The distance to the front wall is measured with two independent sensors displaced by the distance $d_d = d_s(\sin(\alpha_2) - \sin(\alpha_6))$. They are used to determine the yaw angle around the horizontal axis

$$\psi_u = \text{asin} \left(\frac{s_1 - s_2}{d_d} \right) . \quad (4.2)$$

The IMU contains a factory calibrated EKF that fuses the information of the gyroscope and the accelerometer to an estimated attitude provided as a rotation matrix $\mathbf{R}_{imu} = \mathbf{R}_B^{0,imu}$. Here, $\mathcal{F}_{0,imu}$ is an IMU-intern reference coordinate frame that is set at the

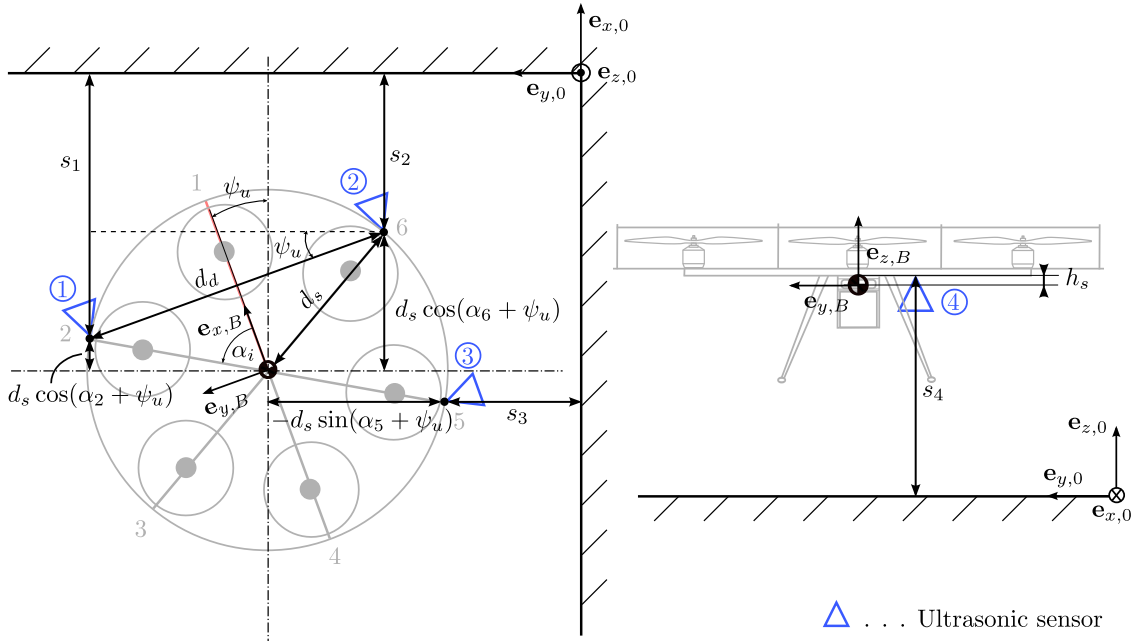


Figure 4.2: Placement of the ultrasonic sensors and the relation between the measurements and the position of the CM.

power up process of the IMU and \mathcal{F}_B is the body-fixed frame. The IMU-internal reference coordinate frame $\mathcal{F}_{0,imu}$ may be at an arbitrary position and is not necessarily horizontally aligned. The attitude control requires Euler angles ϕ in relation to a horizontally aligned inertial frame \mathcal{F}_0 . Thus, a defined inertial frame \mathcal{F}_0 , which is aligned with the floor plane is set before take-off. Therefore, the body-fixed frame when the Hexacopter is standing on the floor is set as the inertial frame $\mathcal{F}_0 = \mathcal{F}_B|_{t=0}$. To this end, the initial rotation matrix $\mathbf{R}_0 = \mathbf{R}_{imu}|_{t=0}$ is measured before take-off. With the initial rotation $\mathbf{R}_0 = \mathbf{R}_0^{0,imu}$ the rotation \mathbf{R}_B^0 results in

$$\mathbf{R}_B^0 = \mathbf{R}_{imu} \mathbf{R}_0^{-1} = \mathbf{R}_B^{0,imu} \mathbf{R}_0^{0,imu} . \quad (4.3)$$

The rotation matrix \mathbf{R}_B^0 (3.2) is an attitude representation with more than one solution for the ZYX-Euler angles. One solution is given by

$$\phi_{imu} = \text{atan} \left(\frac{\mathbf{R}_B^0(2,3)}{\mathbf{R}_B^0(3,3)} \right) \quad (4.4a)$$

$$\theta_{imu} = -\text{asin} \left(\mathbf{R}_B^0(1,3) \right) \quad (4.4b)$$

$$\psi_{imu} = \text{atan} \left(\frac{\mathbf{R}_B^0(1,2)}{\mathbf{R}_B^0(1,1)} \right) , \quad (4.4c)$$

where $\mathbf{R}_B^0(i,j)$ denotes the matrix element in row i and column j .

4.1.2 Complementary filter

In the complementary filter estimation approach, the measurements will be used directly as state information except for some crucial states. Crucial states in this context are states where the corresponding measurement does not yield the required accuracy or speed for the control concept. These states will be estimated by using linear complementary filters. The basic concept of a complementary filter is to fuse a high bandwidth state measurement that suffers from drift with a second low bandwidth measurement of the same state that does not suffer from drift. In this way, the advantages of both measurements can be fused to a stable estimation of the state with high bandwidth.

For the Hexacopter, two states are deemed crucial, namely the height r_z and the yaw angle ψ . First, the height r_z will be investigated. The maximum thrust which can be used for ascending is $f_{t,max} = 105$ N (evaluated by measurements) and with the weight of $m = 3.4$ kg, the maximum vertical acceleration is given by $a_{z,max} = f_{t,max}/m = 30.89$ m/s². With the sampling time of the ultrasonic sensors of $T_u = 100$ ms, the maximum position deviation between two ultrasonic sensor samples results in

$$\Delta r_{z,max} = \frac{a_{z,max} T_u^2}{2} = 0.15 \text{ m} . \quad (4.5)$$

This maximum deviation is considered to be too high for precise control and therefore a higher sampling rate for the height r_z is needed. It is achieved by fusing the measurement data of the acceleration sensor and the ultrasonic sensors in terms of a complementary filter. The second crucial state is the yaw angle ψ . The IMU-intern EKF uses the gravity vector measured by the acceleration sensor to correct an attitude error caused by the drift of the gyroscopes. The correction is only possible for the pitch and the roll angle but not for the yaw angle, as the rotational axis of the yaw angle is nearly parallel to the gravity vector while hovering. To compensate the drift in the yaw angle ψ , it is estimated by the fusion of the gyroscopic measurement and the yaw angle (4.2) measured by the ultrasonic sensors.

The the following, the concept of the complementary filter for the yaw angle is presented. The same procedure can be applied to the height r_z . The yaw angle can be measured in two ways. The first measurement for the yaw angle is via the ultrasonic sensors (4.2), which has no drift but a very low sampling rate with a sampling time of $T_u = 100$ ms. Thus, according to the Nyquist - Shannon sampling theorem, its bandwidth is limited to $\frac{1}{2T_u} = 5$ Hz. The second measurement for the yaw angle is the integration of the rotation rate $\omega_{z,B}$ around the vertical axis measured by the gyroscope. The gyroscope measurement is sampled at the system sampling time T_a and has a sensor specific bandwidth of 300 Hz. The problem with the integration of the gyroscope is that the gyroscope measurement suffers from drift so that the measurement of the angle deviates from its real value with increasing time. The complementary filter uses the low frequency domain of the ultrasonic measurement and the high frequency domain of the gyroscope measurement to obtain a drift-less measurement with high bandwidth. To this end, a low pass filter $G_{lp,\psi}(s)$ for the ultrasonic measurement and a high pass with an additional integration filter $G_{hp,\psi}(s)$ for the gyroscope measurement is designed. The perfect measurement transfer function is a

unity gain frequency response without phase-delay. Thus, the sum of both complementary filters has to match the condition [28]

$$G_{lp,\psi}(s) + sG_{hp,\psi}(s) = 1 . \quad (4.6)$$

For the transfer function of the ultrasonic measurement $G_{lp,\psi}(s)$ a low pass filter extended with a high pass that lifts the gain at the crossover frequency ω_0

$$G_{lp,\psi}(s) = \frac{1 + 2\frac{s}{\omega_0}}{\left(1 + \frac{s}{\omega_0}\right)^2} \quad (4.7)$$

is used. This gain lift is necessary as it compensates for the gain drop of $sG_{hp,\psi}(s)$ at the crossover frequency. For the transfer function of the gyroscopic measurement $G_{hp,\psi}(s)$ a second order high pass with an additional integrator is used

$$G_{hp,\psi}(s) = \frac{1}{s} \frac{\left(\frac{s}{\omega_0}\right)^2}{\left(1 + \frac{s}{\omega_0}\right)^2} . \quad (4.8)$$

These two filters fulfill the desired condition (4.6) for an arbitrary crossover frequency ω_0 as shown in Figure 4.3 where the bode diagram of both complementary filters and their combination (4.6) is shown. The sum of the complementary filters results in a unity gain frequency response without phase-delay as claimed before. The filter design requires just one parameter ω_0 . This parameter is set empirically to $\omega_0 = 1.26$ rad/s.

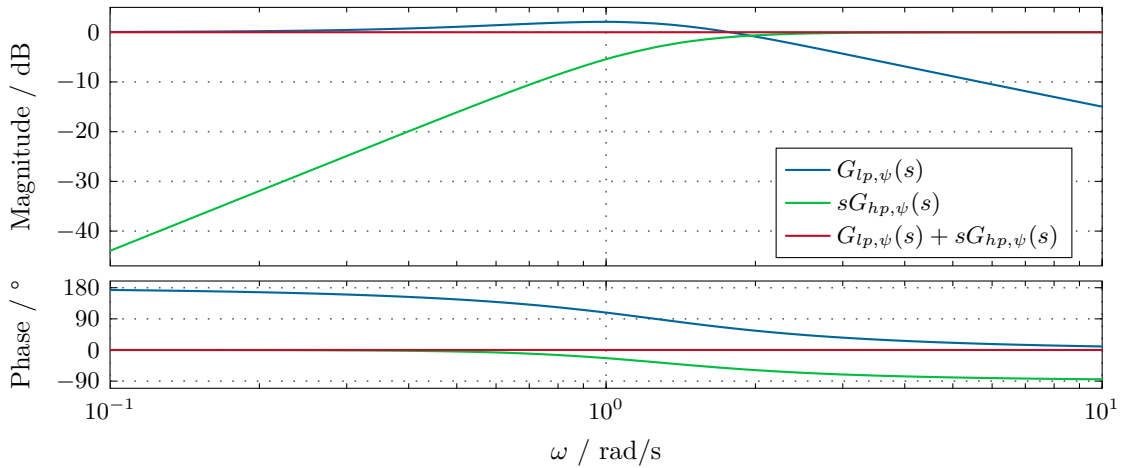


Figure 4.3: Bode diagram illustrating the complementary filter condition (4.6).

With the same concept, the transfer functions for the complementary filter for the height r_z are given by

$$G_{lp,z}(s) = \frac{1 + 2\frac{s}{\omega_0}}{\left(1 + \frac{s}{\omega_0}\right)^2} \quad \text{and} \quad G_{hp,z}(s) = \frac{1}{s^2} \frac{\left(\frac{s}{\omega_0}\right)^2}{\left(1 + \frac{s}{\omega_0}\right)^2} . \quad (4.9)$$

The estimated signals are obtained by adding the low-pass filtered and high-pass filtered signal in the time domain, respectively, yielding

$$\psi_{cf} = g_{lp,\psi} * \psi_u + g_{hp,\psi} * \omega_{z,imu,B} \quad \text{and} \quad r_{z,cf} = g_{lp,z} * r_{z,u} + g_{hp,z} * a_z . \quad (4.10)$$

Here, $*$ is the convolution operator that is used to describe a filter operation in the time domain, ψ_{cf} is the estimation of ψ , and $g_{lp,\psi}$ and $g_{hp,\psi}$ are the impulse responses of the two complementary filters. The same notation applies to the estimated height $r_{z,cf}$. Further, a linear integration filter is used to get an estimation of the vertical velocity v_z . The integration filter is enhanced by a high-pass filter

$$G_{hp,v_z}(s) = \frac{1}{s} \frac{\left(\frac{s}{\omega_0}\right)^6}{\left(1 + \frac{2\delta s}{\omega_0} + \left(\frac{s}{\omega_0}\right)^2\right)^3} \quad (4.11)$$

of 6th order with a low cut off frequency of $\omega_0 = 0.02$ rad/s and the damping factor $\delta = \frac{1}{\sqrt{2}}$. The high order is needed to efficiently suppress an offset in the measured gravity. The estimated velocity is given by

$$v_{z,f} = g_{hp,v_z} * a_z , \quad (4.12)$$

where a_z is the vertical acceleration in the initial frame \mathcal{F}_0 . The same approach applied to the horizontal velocities v_x and v_y does not yield reliable estimations. Thus, the estimation of v_x and v_y will be taken into account using a Luenberger observer when designing the position control in Section 4.4. The complete estimated state vector yields

$$\hat{\mathbf{r}}_{cf} = \begin{bmatrix} r_{x,u} \\ r_{y,u} \\ r_{z,cf} \end{bmatrix} \quad \hat{\mathbf{v}}_{cf} = \begin{bmatrix} \times \\ \times \\ v_{z,f} \end{bmatrix} \quad \hat{\boldsymbol{\phi}}_{cf} = \begin{bmatrix} \phi_{imu} \\ \theta_{imu} \\ \psi_{cf} \end{bmatrix} \quad \hat{\boldsymbol{\omega}}_{cf,B} = \begin{bmatrix} \omega_{x,imu,B} \\ \omega_{y,imu,B} \\ \omega_{z,imu,B} \end{bmatrix} , \quad (4.13)$$

where the index u denotes a measurement with the ultrasonic sensors, the index imu with the IMU and a \times indicates that the corresponding state is not estimated.

4.1.3 Extended Kalman Filter

The second state estimation approach is to use an Extended Kalman Filter (EKF). It fuses the measurement of different sensors to estimate the states under consideration of the system dynamics and a known noise distribution. It is an optimal state observer under the condition that the measurement error and the process noise are independent and Gaussian-distributed. Under these conditions it calculates the optimum solution with respect to the minimum squared error. In the following, the linear Kalman filter will be described first and extended to the EKF, subsequently. The description of the Kalman filter and the EKF are based on [27]. Due to the fact that the ultrasonic measurements are not available at every time step, the EKF will be modified to the so called Continuous-Discrete Extended Kalman Filter (CD-EKF) [29].

Let us consider a linear time-discrete model

$$\mathbf{x}_{k+1} = \Phi \mathbf{x}_k + \Gamma \mathbf{u}_k + \mathbf{G} \mathbf{w}_k \quad (4.14a)$$

$$\mathbf{y}_k = \mathbf{C} \mathbf{x}_k + \mathbf{v}_k, \quad (4.14b)$$

with the state vector \mathbf{x}_k , the input vector \mathbf{u}_k , and the output vector \mathbf{y}_k , as well as the state-transition matrix Φ , the input matrix Γ and the output matrix \mathbf{C} . Moreover, \mathbf{w}_k is a zero-mean Gaussian process noise with the covariance \mathbf{Q} representing unmodeled dynamics. Its influence on the system is represented by the matrix \mathbf{G} , and \mathbf{v}_k is the zero-mean Gaussian measurement noise with the covariance matrix \mathbf{R} . The Kalman filter estimates the state with a prediction and an update step. At the prediction step, the filter predicts the state variables based on the system model and its current system inputs under consideration of $k - 1$ measurements. This is called *a priori estimation* and is denoted by $\hat{\mathbf{x}}_k^- = \hat{\mathbf{x}}(k|k-1)$ where $\hat{\mathbf{x}}(k|k-1)$ indicates that $k - 1$ measurements are considered for the estimation of the state vector \mathbf{x} at the time $t = kT_a$. The second step is the update where the predicted states are corrected based on k measurements. This is called *posteriori estimation* which is denoted by $\hat{\mathbf{x}}_k^+ = \hat{\mathbf{x}}(k|k)$. The prediction equations are given by the copy of the system and an estimation of the covariance

$$\hat{\mathbf{x}}_{k+1}^- = \Phi \hat{\mathbf{x}}_k^+ + \Gamma \mathbf{u}_k \quad (4.15a)$$

$$\mathbf{P}_{k+1}^- = \Phi \mathbf{P}_k^+ \Phi^T + \mathbf{G} \mathbf{Q} \mathbf{G}^T, \quad (4.15b)$$

where $\hat{\mathbf{x}}_k$ is the estimated state and \mathbf{P}_k is the estimated covariance matrix of the states. The update equations are given by a correction where the correction gain is determined by the covariance and the measurement noise of the sensors

$$\hat{\mathbf{L}}_k = \mathbf{P}_k^- \mathbf{C}^T (\mathbf{C} \mathbf{P}_k^- \mathbf{C}^T + \mathbf{R})^{-1} \quad (4.16a)$$

$$\hat{\mathbf{x}}_k^+ = \hat{\mathbf{x}}_k^- + \hat{\mathbf{L}}_k (\mathbf{y}_k - \mathbf{C} \hat{\mathbf{x}}_k^-) \quad (4.16b)$$

$$\mathbf{P}_{k+1}^- = (\mathbf{E} - \hat{\mathbf{L}}_k \mathbf{C}) \mathbf{P}_k^- . \quad (4.16c)$$

Here, $\hat{\mathbf{L}}_k$ is the correction gain that weights the measurement against the prediction and \mathbf{E} is the identity matrix.

The presented Kalman filter is only able to predict the state of a linear system. To address nonlinear systems a so-called EKF can be used. Here, a nonlinear time-discrete model

$$\mathbf{x}_{k+1} = \mathbf{F}_k(\mathbf{x}_k, \mathbf{u}_k, \mathbf{w}_k) \quad (4.17a)$$

$$\mathbf{y}_k = \mathbf{h}_k(\mathbf{x}_k, \mathbf{u}_k, \mathbf{v}_k), \quad (4.17b)$$

is considered. Usually, \mathbf{F}_k has to be approximated by an appropriate integration method. In the following, the Euler method

$$\mathbf{F}_k = \mathbf{x}_k + T_a \mathbf{f}(\mathbf{x}_k, \mathbf{u}_k, \mathbf{w}_k) \quad (4.18)$$

will be used where $\mathbf{f}(\mathbf{x}_k, \mathbf{u}_k, \mathbf{w}_k)$ refers to the corresponding nonlinear time-continuous system of the form $\dot{\mathbf{x}} = \mathbf{f}(\mathbf{x}, \mathbf{u}, \mathbf{w})$, $\mathbf{y} = \mathbf{h}(\mathbf{x}, \mathbf{u}, \mathbf{v})$. The EKF is a time-variant version of the Kalman filter that linearizes the nonlinear time-discrete system equation at every time step about the posteriori estimation $\hat{\mathbf{x}}_k^+$

$$\Phi_k = \frac{\partial}{\partial \mathbf{x}} \mathbf{F}_k(\hat{\mathbf{x}}_k^+, \mathbf{u}_k, \mathbf{0}) = \mathbf{E} + T_a \frac{\partial}{\partial \mathbf{x}} \mathbf{f}(\hat{\mathbf{x}}_k^+, \mathbf{u}_k, \mathbf{0}) \quad (4.19a)$$

$$\mathbf{G}_k = \frac{\partial}{\partial \mathbf{w}_k} \mathbf{F}_k(\hat{\mathbf{x}}_k^+, \mathbf{u}_k, \mathbf{0}) \quad (4.19b)$$

and the nonlinear output functions about the a priori estimation $\hat{\mathbf{x}}_k^-$

$$\frac{\partial}{\partial \mathbf{x}} \mathbf{h}_k(\hat{\mathbf{x}}_k^-, \mathbf{u}_k, \mathbf{0}) = \mathbf{C}_k . \quad (4.20)$$

Applying a similar procedure as before leads to the filter equations

$$\hat{\mathbf{x}}_{k+1}^- = \mathbf{F}_k(\hat{\mathbf{x}}_k^+, \mathbf{u}_k, \mathbf{0}) \quad (4.21a)$$

$$\mathbf{P}_{k+1}^- = \Phi_k \mathbf{P}_k^+ \Phi_k^T + \mathbf{G}_k \mathbf{Q} \mathbf{G}_k^T \quad (4.21b)$$

$$\hat{\mathbf{L}}_k = \mathbf{P}_k^- \mathbf{C}_k^T (\mathbf{C}_k \mathbf{P}_k^- \mathbf{C}_k^T + \mathbf{R})^{-1} \quad (4.21c)$$

$$\hat{\mathbf{x}}_k^+ = \hat{\mathbf{x}}_k^- + \hat{\mathbf{L}}_k (\mathbf{y}_k - \mathbf{h}_k(\hat{\mathbf{x}}_k^-, \mathbf{u}_k, \mathbf{0})) \quad (4.21d)$$

$$\mathbf{P}_k^+ = (\mathbf{E} - \hat{\mathbf{L}}_k \mathbf{C}_k) \mathbf{P}_k^- . \quad (4.21e)$$

Here, the process noise $\mathbf{w}_k = \mathbf{0}$ in the prediction step and the measurement noise $\mathbf{v}_k = \mathbf{0}$ in the update step are both Gaussian distributed around zero.

The implementation of the EKF is based on the system, compare (3.48)

$$\begin{aligned} \dot{\hat{\mathbf{x}}} &= \mathbf{f}(\hat{\mathbf{x}}, \mathbf{u}, \mathbf{w}) \\ &= \begin{bmatrix} \dot{\hat{\mathbf{r}}} \\ \dot{\hat{\mathbf{v}}} \\ \dot{\hat{\phi}} \end{bmatrix} = \begin{bmatrix} \hat{\mathbf{v}} + \mathbf{w}_r \\ \frac{1}{m} \left[-mg\mathbf{e}_{z,0} + \hat{\mathbf{R}}_0^B (\mathbf{f}_{l,B}(S_1, \dots, S_6, U_{batt}) + \hat{\mathbf{f}}_{d,B}(\hat{\phi}, \hat{\mathbf{v}})) \right] + \mathbf{w}_v \\ \hat{\mathbf{B}}\boldsymbol{\omega}_{imu,B} + \mathbf{w}_\phi \end{bmatrix} \end{aligned} \quad (4.22)$$

with the additive process noise \mathbf{w}_r , \mathbf{w}_v , and \mathbf{w}_ϕ , the state

$$\hat{\mathbf{x}} = [\hat{r}_x \quad \hat{r}_y \quad \hat{r}_z \quad \hat{v}_x \quad \hat{v}_y \quad \hat{v}_z \quad \hat{\phi} \quad \hat{\theta} \quad \hat{\psi}]^T , \quad (4.23)$$

and the system input

$$\mathbf{u} = [\boldsymbol{\omega}_{imu,B} \quad S_1 \dots S_6 \quad U_{batt}]^T . \quad (4.24)$$

Here, $\boldsymbol{\omega}_{imu,B} = [\omega_{x,imu,B} \quad \omega_{y,imu,B} \quad \omega_{z,imu,B}]^T$ is the measured rotation rate, S_1, \dots, S_6 are the motor control inputs, and U_{batt} is the battery voltage. The system inputs S_1, \dots, S_6 and U_{batt} are needed to calculate the total thrust $\mathbf{f}_{l,B}(S_1, \dots, S_6, U_{batt})$ of (3.27). The model (4.22) is a reduced and simplified version of the complete model (3.48). It is reduced

by the state ω_B , as ω_B is directly measured by the gyroscope $\omega_{imu,B}$. Thus, $\omega_{imu,B}$ is used as a system input. The ground effect (3.47) is neglected as its influence decreases significantly with the height and the Hexacopter is intended to fly mainly at a height where the ground effect can be omitted. The drag force (3.42) is included in the model as it improves the estimation of the horizontal velocity [4, 30].

For the update step, the measurement

$$\mathbf{y} = \begin{bmatrix} a_{x,imu,B} & a_{y,imu,B} & r_{x,u} & r_{y,u} & r_{z,u} & \psi_u \end{bmatrix}^T, \quad (4.25)$$

is used where $a_{x,imu,B}$ and $a_{y,imu,B}$ are the horizontal acceleration components measured by the IMU and $r_{\iota,u}$, $\iota \in \{x, y, z\}$ and ψ_u are from (4.1) and (4.2). The model output used in the update step is given by

$$\mathbf{h} = \begin{bmatrix} \hat{a}_{x,B} & \hat{a}_{y,B} & \hat{r}_x & \hat{r}_y & \hat{r}_z & \hat{\psi} \end{bmatrix}^T, \quad (4.26)$$

where $\hat{a}_{x,B}$ and $\hat{a}_{y,B}$ are the horizontal components of the estimated acceleration sensor output $\hat{\mathbf{a}}_B = \begin{bmatrix} \hat{a}_{x,B} & \hat{a}_{y,B} & \hat{a}_{z,B} \end{bmatrix}^T$ derived by the estimated states. An accelerometer measures the difference between the objects acceleration and the gravity. Thus, the function for the estimation of the acceleration sensor output yields

$$\begin{aligned} \hat{\mathbf{a}}_B &= \hat{\mathbf{R}}_B^0 \left(\dot{\hat{\mathbf{v}}} - (-g\mathbf{e}_{z,0}) \right) = \frac{1}{m} \left(\hat{\mathbf{f}}_{t,B} + \hat{\mathbf{f}}_{d,B} \right) \\ &= \frac{1}{m} \begin{bmatrix} -6\mu_d \hat{v}_{x,B} \\ -6\mu_d \hat{v}_{y,B} \\ f_t(S_1, \dots, S_6, U_{batt}) \end{bmatrix}. \end{aligned} \quad (4.27)$$

where $\hat{v}_{x,B}$ and $\hat{v}_{y,B}$ are the horizontal velocities in the body fixed frame \mathcal{F}_B . By considering the drag model, the measured acceleration is direct proportional to the velocity in the body-fixed xy -plane. Thus, the horizontal components of the acceleration measurement can be used to measure the horizontal velocity and improve the observability of the horizontal velocity components [4, 30].

As mentioned before, the measurement of the ultrasonic sensors are only available at a lower sampling frequency compared to the system execution rate. Therefore, the observer is implemented as Continuous-Discrete Extended Kalman Filter (CD-EKF) [29]. The CD-EKF consists of a prediction phase and an update step. In the prediction phase, when there is no measurement available, the state is propagated according to the system equations (4.21a) - (4.21b). In the update step, performed if a measurement of a sensor is available, the update (4.21c) - (4.21e) is performed for the corresponding sensor. Algorithm 1 explains the CD-EKF with a pseudo code. The measurement of the IMU is sampled at every time step, hence the acceleration sensor is updated continuously. The measurement of the ultrasonic sensors is sampled at a lower frequency and is updated only if a new measurement is available. It is noted here that a strong deviation of the model to the reality causes discrete steps in the estimated state at every measurement update of a ultrasonic sensor.

Algorithm 1 Implementation of the CD-EKF.

init: $\hat{\mathbf{x}}_k^-, \mathbf{P}_k^-, \mathbf{Q}, \mathbf{R}$
repeat
 if a measurement has been received from sensor i **then**
 update step: measurement update for the sensor i
 end if
 prediction phase: propagate the system equation.
end repeat

4.2 Set point value filter

The following control concept requires the first two time derivatives of their reference signals. To obtain these time derivatives during runtime, the reference signals are filtered by a linear Set-point Value Filter (SVF) which provides the filtered reference signal and its time derivatives. Further, the SVF is used to limit the maximum dynamics of the reference signal. For this reason it is realised as a linear low pass filter with a triple pole at $s_0 = \frac{2\pi}{T_f}$ where T_f is the filter time constant. The transfer function reads as

$$G_{svf}(s) = \frac{1}{\left(s + \frac{2\pi}{T_f}\right)^3} = \frac{\bar{a}_0}{s^3 + \bar{a}_2 s^2 + \bar{a}_1 s + \bar{a}_0} \quad (4.28)$$

with the coefficients

$$\bar{a}_0 = \frac{8\pi^3}{T_f^3}, \quad \bar{a}_1 = \frac{12\pi^2}{T_f^2}, \quad \text{and} \quad \bar{a}_2 = \frac{6\pi}{T_f}. \quad (4.29)$$

To get the derivatives of the low pass filter, the SVF is expressed in its canonical state space representation

$$\dot{\mathbf{x}} = \mathbf{A}\mathbf{x} + \mathbf{b}u \quad (4.30a)$$

$$\mathbf{y} = \mathbf{C}\mathbf{x} \quad (4.30b)$$

with the matrices

$$\mathbf{A} = \begin{bmatrix} 0 & 1 & 0 \\ 0 & 0 & 1 \\ -\bar{a}_0 & -\bar{a}_1 & -\bar{a}_2 \end{bmatrix}, \quad \mathbf{b} = \begin{bmatrix} 0 \\ 0 \\ 1 \end{bmatrix}, \quad \text{and} \quad \mathbf{C} = \begin{bmatrix} \bar{a}_0 & 0 & 0 \\ 0 & \bar{a}_0 & 0 \\ 0 & 0 & \bar{a}_0 \end{bmatrix}. \quad (4.31)$$

The SVF is applied to all reference signals of the position and attitude controller. The time constants T_f for the different reference signals are set empirically and listed in Table A.6 in Appendix A.

4.3 Attitude control

The attitude control stabilizes the tilt and the twist of the Hexacopter at a desired trajectory of Euler angles $\phi_d(t) = [\phi_d(t) \quad \theta_d(t) \quad \psi_d(t)]^T$. To stabilize the fully actuated

rotational subsystem (3.48c) and (3.48d), a backstepping control approach based on the Lyapunov theory is used. The following description of the Lyapunov theory and the backstepping control is based on [31]. The Lyapunov theory states that an autonomous time invariant system

$$\dot{\mathbf{x}} = \mathbf{f}(\mathbf{x}) \quad (4.32)$$

is stable at an equilibrium \mathbf{x}_{ss} if there exists a Lyapunov function $V(\mathbf{x})$ that is positive definite and its time derivative $\dot{V}(\mathbf{x})$ is negative semidefinite. Further, the system is asymptotically stable if the time derivative $\dot{V}(\mathbf{x})$ is negative definite. Let us consider a system in the strict-feedback form

$$\dot{\mathbf{x}}_1 = \mathbf{f}_1(\mathbf{x}_1) + \mathbf{g}_1(\mathbf{x}_1)\mathbf{x}_2 \quad (4.33a)$$

$$\dot{\mathbf{x}}_2 = \mathbf{f}_2(\mathbf{x}_1, \mathbf{x}_2) + \mathbf{g}_2(\mathbf{x}_1, \mathbf{x}_2)\mathbf{u} , \quad (4.33b)$$

with the states \mathbf{x}_1 and \mathbf{x}_2 and the system input \mathbf{u} . The subsystem (4.33a) is for control purposes only accessible via an integrator step. The idea of backstepping is to find first a virtual feedback law $\mathbf{x}_2 = \boldsymbol{\alpha}(\mathbf{x}_1)$, which stabilizes the closed-loop system of the subsystem (4.33a). Based on this, the control \mathbf{u} is designed to stabilize the equilibrium of the whole closed-loop system (4.33).

The attitude control design is based on a simplified model of the rotational subsystem (3.48c) and (3.48d). In this model the gyroscopic effect $\boldsymbol{\tau}_{g,B}$ and the drag effect $\boldsymbol{\tau}_{d,B}$ are neglected as their influence is small in comparison to the control input $\boldsymbol{\tau}_{t,B}$. Additionally, a bias torque $\boldsymbol{\tau}_0$ is included in the system equations. This torque was identified during experiments and is most likely caused by an asymmetrical behavior of the motor controllers. However, the bias torque $\boldsymbol{\tau}_0$ is assumed to be constant and is therefore included in the model for the backstepping design. Later on an estimation of $\boldsymbol{\tau}_0$ will be systematically included in the controller design. The system equations for the simplified model of the rotating subsystem are given by

$$\dot{\boldsymbol{\phi}} = \mathbf{B}(\boldsymbol{\phi})\boldsymbol{\omega}_B \quad (4.34a)$$

$$\dot{\boldsymbol{\omega}}_B = \mathbf{I}^{-1}(-\boldsymbol{\omega}_B \times \mathbf{I}\boldsymbol{\omega}_B + \boldsymbol{\tau}_{t,B} + \boldsymbol{\tau}_0) . \quad (4.34b)$$

For the control design, it is convenient to work with a system that uses $\boldsymbol{\phi}$ and its time derivative $\dot{\boldsymbol{\phi}}$ as states. Thus, $\boldsymbol{\omega}_B$ is substituted by an expression of $\boldsymbol{\phi}$ which results in

$$\boldsymbol{\omega}_B = \mathbf{B}^{-1}(\boldsymbol{\phi})\dot{\boldsymbol{\phi}} \quad (4.35a)$$

$$\dot{\boldsymbol{\omega}}_B = \frac{d}{dt}\mathbf{B}^{-1}(\boldsymbol{\phi})\dot{\boldsymbol{\phi}} + \mathbf{B}^{-1}(\boldsymbol{\phi})\ddot{\boldsymbol{\phi}} . \quad (4.35b)$$

Inserting (4.35) into (4.34) and using the state variables $\mathbf{x}_1 = \boldsymbol{\phi}$ and $\mathbf{x}_2 = \dot{\boldsymbol{\phi}}$, the system input $\mathbf{u} = \boldsymbol{\tau}_{t,B}$, and the parameter $\mathbf{v}_0 = \boldsymbol{\tau}_0$ yields the system in strict-feedback form [3]

$$\dot{\mathbf{x}}_1 = \mathbf{x}_2 \quad (4.36a)$$

$$\begin{aligned} \dot{\mathbf{x}}_2 = & \mathbf{B}(\mathbf{x}_1) \left(\underbrace{\mathbf{I}^{-1} \left(-\mathbf{B}^{-1}(\mathbf{x}_1)\mathbf{x}_2 \times \mathbf{I}\mathbf{B}^{-1}(\mathbf{x}_1)\mathbf{x}_2 \right) - \frac{d}{dt}\mathbf{B}^{-1}(\mathbf{x}_1)\mathbf{x}_2}_{\mathbf{f}(\mathbf{x}_1, \mathbf{x}_2)} \right) \\ & + \underbrace{\mathbf{B}(\mathbf{x}_1)\mathbf{I}^{-1}}_{\mathbf{g}(\mathbf{x}_1)} (\mathbf{u} + \mathbf{v}_0) . \end{aligned} \quad (4.36b)$$

The parameter \mathbf{v}_0 fulfills the *matching condition* which states that the unknown parameter \mathbf{v}_0 influences the system in the same way as the system input \mathbf{u} . In a first step, the parameter \mathbf{v}_0 is assumed to be known and the feedback law $\mathbf{u} = \boldsymbol{\alpha}(\mathbf{x}_1, \mathbf{x}_2)$ is derived. In a second step, the difference of the estimation $\hat{\mathbf{v}}_0$ to the real parameter \mathbf{v}_0 , i. e., the estimation error $\tilde{\mathbf{v}}_0 = \hat{\mathbf{v}}_0 - \mathbf{v}_0$, is considered and a differential equation for the parameter estimation will be derived.

The controller has to stabilize the attitude at a desired trajectory $\mathbf{x}_{1,d}$. Thus, the tracking error is defined as

$$\boldsymbol{\varepsilon}_1 = \mathbf{x}_1 - \mathbf{x}_{1,d} . \quad (4.37)$$

The error system for the error $\boldsymbol{\varepsilon}_1$ results in

$$\dot{\boldsymbol{\varepsilon}}_1 = \dot{\mathbf{x}}_1 - \dot{\mathbf{x}}_{1,d} = \mathbf{x}_2 - \dot{\mathbf{x}}_{1,d} . \quad (4.38)$$

With \mathbf{x}_2 as virtual control input for the error system (4.38), the state feedback law

$$\mathbf{x}_2 = \boldsymbol{\alpha}(\boldsymbol{\varepsilon}_1) = \dot{\mathbf{x}}_{1,d} - \mathbf{C}_1\boldsymbol{\varepsilon}_1 , \quad (4.39)$$

with the positive definite diagonal matrix \mathbf{C}_1 , stabilizes (4.38) at $\boldsymbol{\varepsilon}_{1,ss} = \mathbf{0}$. The closed loop error system of (4.38) yields

$$\dot{\boldsymbol{\varepsilon}}_1 = -\mathbf{C}_1\boldsymbol{\varepsilon}_1 \quad (4.40)$$

which is obviously asymptotically stable. This can be shown using the positive definite Lyapunov function

$$V_1 = \frac{1}{2}\boldsymbol{\varepsilon}_1^T\boldsymbol{\varepsilon}_1 > 0 . \quad (4.41)$$

Its time derivative

$$\dot{V}_1 = \frac{1}{2}\boldsymbol{\varepsilon}_1^T\dot{\boldsymbol{\varepsilon}}_1 = \boldsymbol{\varepsilon}_1^T(\boldsymbol{\alpha}(\boldsymbol{\varepsilon}_1) - \dot{\mathbf{x}}_{1,d}) = -\boldsymbol{\varepsilon}_1^T\mathbf{C}_1\boldsymbol{\varepsilon}_1 < 0 \quad (4.42)$$

is negative definite and hence the error system (4.38) is asymptotically stable.

In a second step, the error between the state \mathbf{x}_2 and the virtual control input $\boldsymbol{\alpha}(\boldsymbol{\varepsilon}_1)$

$$\boldsymbol{\varepsilon}_2 = \mathbf{x}_2 - \boldsymbol{\alpha}(\boldsymbol{\varepsilon}_1) = \underbrace{\overbrace{\mathbf{x}_2}^{\dot{\mathbf{x}}_1} - \dot{\mathbf{x}}_{1,d}}_{\dot{\boldsymbol{\varepsilon}}_1} + \mathbf{C}_1\boldsymbol{\varepsilon}_1 \quad (4.43)$$

is defined. Thus, the error system of $\boldsymbol{\varepsilon}_1$ and $\boldsymbol{\varepsilon}_2$ yields

$$\dot{\boldsymbol{\varepsilon}}_1 = -\mathbf{C}_1\boldsymbol{\varepsilon}_1 + \boldsymbol{\varepsilon}_2 \quad (4.44a)$$

$$\dot{\boldsymbol{\varepsilon}}_2 = \tilde{\mathbf{f}}(\boldsymbol{\varepsilon}_1, \boldsymbol{\varepsilon}_2) + \tilde{\mathbf{g}}(\boldsymbol{\varepsilon}_1)(\mathbf{u} + \mathbf{v}_0) - \left(\ddot{\mathbf{x}}_{1,d} + \mathbf{C}_1^2\boldsymbol{\varepsilon}_1 - \mathbf{C}_1\boldsymbol{\varepsilon}_2\right). \quad (4.44b)$$

Using the positive definite Lyapunov function

$$V_2 = \frac{1}{2}\boldsymbol{\varepsilon}_1^T\boldsymbol{\varepsilon}_1 + \frac{1}{2}\boldsymbol{\varepsilon}_2^T\boldsymbol{\varepsilon}_2 > 0 \quad (4.45)$$

yields the time derivative

$$\begin{aligned} \dot{V}_2 &= \boldsymbol{\varepsilon}_1^T\dot{\boldsymbol{\varepsilon}}_1 + \boldsymbol{\varepsilon}_2^T\dot{\boldsymbol{\varepsilon}}_2 \\ &= \boldsymbol{\varepsilon}_1^T(-\mathbf{C}_1\boldsymbol{\varepsilon}_1 + \boldsymbol{\varepsilon}_2) + \boldsymbol{\varepsilon}_2^T\left(\tilde{\mathbf{f}}(\boldsymbol{\varepsilon}_1, \boldsymbol{\varepsilon}_2) + \tilde{\mathbf{g}}(\boldsymbol{\varepsilon}_1)(\mathbf{u} + \mathbf{v}_0) - \left(\ddot{\mathbf{x}}_{1,d} + \mathbf{C}_1^2\boldsymbol{\varepsilon}_1 - \mathbf{C}_1\boldsymbol{\varepsilon}_2\right)\right) \\ &= -\boldsymbol{\varepsilon}_1^T\mathbf{C}_1\boldsymbol{\varepsilon}_1 \\ &\quad + \underbrace{\boldsymbol{\varepsilon}_2^T\left(\boldsymbol{\varepsilon}_1 + \tilde{\mathbf{f}}(\boldsymbol{\varepsilon}_1, \boldsymbol{\varepsilon}_2) + \tilde{\mathbf{g}}(\boldsymbol{\varepsilon}_1)(\mathbf{u} + \mathbf{v}_0) - \left(\ddot{\mathbf{x}}_{1,d} + \mathbf{C}_1^2\boldsymbol{\varepsilon}_1 - \mathbf{C}_1\boldsymbol{\varepsilon}_2\right)\right)}_{\mathbf{T}_u} < 0. \end{aligned} \quad (4.46)$$

The control law for the backstepping algorithm is obtain by ensuring that the time derivative of V_2 is negative definite. This can be achieved by setting

$$\mathbf{T}_u = -\mathbf{C}_2\boldsymbol{\varepsilon}_2 \quad (4.47)$$

with a positive definite diagonal matrix \mathbf{C}_2 . Thus, the control law can be directly written as

$$\mathbf{u} = \frac{1}{\tilde{\mathbf{g}}(\boldsymbol{\varepsilon}_1)} \left(-\tilde{\mathbf{f}}(\boldsymbol{\varepsilon}_1, \boldsymbol{\varepsilon}_2) + \ddot{\mathbf{x}}_{1,d} + \left(\mathbf{C}_1^2 - \mathbf{E}\right)\boldsymbol{\varepsilon}_1 - \left(\mathbf{C}_1 + \mathbf{C}_2\right)\boldsymbol{\varepsilon}_2\right) - \mathbf{v}_0. \quad (4.48)$$

The closed-loop error system of (4.44) results in

$$\dot{\boldsymbol{\varepsilon}}_1 = -\mathbf{C}_1\boldsymbol{\varepsilon}_1 + \boldsymbol{\varepsilon}_2 \quad (4.49a)$$

$$\dot{\boldsymbol{\varepsilon}}_2 = -\boldsymbol{\varepsilon}_1 - \mathbf{C}_2\boldsymbol{\varepsilon}_2. \quad (4.49b)$$

Hence, with the positive definite Lyapunov function (4.45) and its negative definite time derivative the closed-loop tracking error system (4.49) is asymptotically stable.

So far, the parameter \mathbf{v}_0 is assumed to be known. In the next step, a parameter estimator for the unknown parameter $\hat{\mathbf{v}}_0$ will be derived. Inserting the feedback law (4.48) with $\mathbf{v}_0 = \hat{\mathbf{v}}_0$ in (4.44) yields

$$\dot{\boldsymbol{\varepsilon}}_1 = -\mathbf{C}_1\boldsymbol{\varepsilon}_1 + \boldsymbol{\varepsilon}_2 \quad (4.50a)$$

$$\dot{\boldsymbol{\varepsilon}}_2 = -\boldsymbol{\varepsilon}_1 - \mathbf{C}_2\boldsymbol{\varepsilon}_2 - \tilde{\mathbf{g}}(\boldsymbol{\varepsilon}_1)\underbrace{(\hat{\mathbf{v}}_0 - \mathbf{v}_0)}_{\tilde{\mathbf{v}}_0}. \quad (4.50b)$$

To derive an estimator for \mathbf{v}_0 , the Lyapunov function V_2 is extended by a term related to the estimation error $\tilde{\mathbf{v}}_0$

$$V_{2e} = V_2 + \frac{1}{2\gamma} \tilde{\mathbf{v}}_0^T \tilde{\mathbf{v}}_0 > 0 \quad (4.51)$$

where $\gamma > 0$ is an estimation parameter. The time derivative of the extended Lyapunov function V_{2e} yields

$$\begin{aligned} \dot{V}_{2e} &= \boldsymbol{\varepsilon}_1^T (-\mathbf{C}_1 \boldsymbol{\varepsilon}_1 + \boldsymbol{\varepsilon}_2) + \boldsymbol{\varepsilon}_2^T (-\boldsymbol{\varepsilon}_1 - \mathbf{C}_2 \boldsymbol{\varepsilon}_2 - \tilde{\mathbf{g}}(\boldsymbol{\varepsilon}_1) \tilde{\mathbf{v}}_0) + \frac{1}{\gamma} \tilde{\mathbf{v}}_0^T \dot{\tilde{\mathbf{v}}}_0 \\ &= -\boldsymbol{\varepsilon}_1^T \mathbf{C}_1 \boldsymbol{\varepsilon}_1 - \boldsymbol{\varepsilon}_2^T \mathbf{C}_2 \boldsymbol{\varepsilon}_2 - \underbrace{\tilde{\mathbf{v}}_0^T \left(-\tilde{\mathbf{g}}^T(\boldsymbol{\varepsilon}_1) \boldsymbol{\varepsilon}_2 + \frac{1}{\gamma} \dot{\tilde{\mathbf{v}}}_0 \right)}_{\mathbf{T}_v} \leq 0. \end{aligned} \quad (4.52)$$

To eliminate the influence of the unknown parameter error $\tilde{\mathbf{v}}_0$ in (4.52) the term \mathbf{T}_v is set to zero and the estimation equation results in

$$\dot{\tilde{\mathbf{v}}}_0 = \dot{\hat{\mathbf{v}}}_0 - \underbrace{\dot{\tilde{\mathbf{v}}}_0}_{=0} = \dot{\hat{\mathbf{v}}}_0 = \gamma \tilde{\mathbf{g}}^T(\boldsymbol{\varepsilon}_1) \boldsymbol{\varepsilon}_2 \quad (4.53)$$

for parameter \mathbf{v}_0 , which is assumed to be unknown but constant.

In practice, it is common to tune a gain of the proportional and derivative of the error of the desired trajectory. Therefore, the errors

$$\boldsymbol{\varepsilon}_p = \mathbf{x}_1 - \mathbf{x}_{1,d} = \boldsymbol{\varepsilon}_1 \quad \text{and} \quad \boldsymbol{\varepsilon}_d = \mathbf{x}_2 - \dot{\mathbf{x}}_{1,d} = \boldsymbol{\varepsilon}_2 - \mathbf{C}_1 \boldsymbol{\varepsilon}_1 \quad (4.54)$$

are introduced. Using these errors and including the estimated parameter $\hat{\mathbf{v}}_0$ it is possible to rewrite the feedback law (4.48) to

$$\mathbf{u} = \frac{1}{\tilde{\mathbf{g}}(\boldsymbol{\varepsilon}_1)} \left(-\tilde{\mathbf{f}}(\boldsymbol{\varepsilon}_1, \boldsymbol{\varepsilon}_2) + \ddot{\mathbf{x}}_{1,d} - \mathbf{C}_p \boldsymbol{\varepsilon}_p - \mathbf{C}_d \boldsymbol{\varepsilon}_d \right) - \hat{\mathbf{v}}_0. \quad (4.55)$$

The relation between the proportional and differential gain matrices \mathbf{C}_p and \mathbf{C}_d to the parameter matrices \mathbf{C}_1 and \mathbf{C}_2 is given by

$$\mathbf{C}_p = \mathbf{E} + \mathbf{C}_1 \mathbf{C}_2 \quad (4.56a)$$

$$\mathbf{C}_d = \mathbf{C}_1 + \mathbf{C}_2. \quad (4.56b)$$

As \mathbf{C}_1 , \mathbf{C}_2 , \mathbf{C}_p , and \mathbf{C}_d are all diagonal matrices, the following expressions are applied to their diagonal elements, which justifies the matrix notation. Solving (4.56) for the parameter matrices \mathbf{C}_1 and \mathbf{C}_2 results in

$$\mathbf{C}_1 = \frac{\mathbf{C}_d}{2} + \sqrt{\left(\frac{\mathbf{C}_d}{2}\right)^2 - \mathbf{C}_p + \mathbf{E}} \quad (4.57a)$$

$$\mathbf{C}_2 = \frac{\mathbf{C}_d}{2} - \sqrt{\left(\frac{\mathbf{C}_d}{2}\right)^2 - \mathbf{C}_p + \mathbf{E}}, \quad (4.57b)$$

and the system is asymptotically stable at the trajectory ϕ_d as long as

$$\mathbf{C}_d^2 > 4(\mathbf{C}_p - \mathbf{E}) . \quad (4.58)$$

With (4.57) the parameter estimation of \mathbf{v}_0 is given by

$$\dot{\mathbf{v}}_0 = \gamma \tilde{\mathbf{g}}^T(\boldsymbol{\varepsilon}_1) \left[\boldsymbol{\varepsilon}_d + \left(\frac{\mathbf{C}_d}{2} + \sqrt{\left(\frac{\mathbf{C}_d}{2} \right)^2 - \mathbf{C}_p + \mathbf{E}} \right) \boldsymbol{\varepsilon}_p \right] . \quad (4.59)$$

4.4 Position control

The position control stabilizes the Hexacopter at a desired trajectory of the position $\mathbf{r}_d(t) = [r_{x,d}(t) \ r_{y,d}(t) \ r_{z,d}(t)]^T$. To stabilize the underactuated translational subsystem (3.48a) and (3.48b), a controller based on the flatness property of the Hexacopter is used. A system

$$\dot{\mathbf{x}} = \mathbf{f}(\mathbf{x}, \mathbf{u}) \quad (4.60a)$$

$$\mathbf{y} = \mathbf{h}(\mathbf{x}) \quad (4.60b)$$

is called differential flat if the output \mathbf{y} is differentially independent and all system variables, namely state and input variables, can be parameterized in the output variable \mathbf{y} and its time derivatives [31]

$$\begin{bmatrix} \mathbf{x} \\ \mathbf{u} \end{bmatrix} = \boldsymbol{\chi}(\mathbf{y}, \dot{\mathbf{y}}, \ddot{\mathbf{y}}, \dots, \mathbf{y}^{(n)}) . \quad (4.61)$$

A system output \mathbf{y} that satisfies these conditions is called a flat output of the system. This property can be used for an exact feedforward linearisation of the system at a certain trajectory \mathbf{y}_d . The required control variable \mathbf{u}_d to follow the desired trajectory \mathbf{y}_d can be algebraically computed from the flat output reference signal and its time derivatives. An additional linear controller is used to stabilize the trajectory error system.

The position control design is based on a simplified model of the translational subsystem (3.48a) and (3.48b). In this model, the drag force $\mathbf{f}_{d,B}$ is neglected as its influence is small in comparison to the controlling force $\mathbf{R}_0^B(\phi, \theta, \psi) f_t \mathbf{e}_{z,B}$. Additionally, the ground effect (3.47) is neglected as its influence decreases significantly with the height and the Hexacopter is intended to fly mainly at a height where the ground effect can be omitted. The system equations for the simplified model of the translational subsystem are given by

$$\dot{\mathbf{r}} = \mathbf{v} \quad (4.62a)$$

$$\dot{\mathbf{v}} = \frac{1}{m} \left(-mg \mathbf{e}_{z,0} + \mathbf{R}_0^B(\phi, \theta, \psi) f_t \mathbf{e}_{z,B} \right) , \quad (4.62b)$$

with the system input $\mathbf{u} = [\phi \ \theta \ f_t]^T$ and the known disturbance ψ . The position $\mathbf{y} = \mathbf{r}$ is a flat output of the system (4.62). The state vector $\mathbf{x}_{pc} = [r_x \ r_y \ r_z \ v_x \ v_y \ v_z]^T$

consists of the position \mathbf{r} and the velocity $\mathbf{v} = \dot{\mathbf{r}}$ of the Hexacopter, hence the state vector \mathbf{x}_{pc} is a function of the flat output \mathbf{r} and its derivatives. Further, the system input \mathbf{u} can be expressed in the derivatives of \mathbf{r} as shown in the following. For this, (4.62b) is written in components which results in the set of equations

$$\ddot{r}_x = \dot{v}_x = \frac{f_t}{m} (\cos(\phi) \sin(\theta) \cos(\psi) + \sin(\phi) \sin(\psi)) \quad I \quad (4.63a)$$

$$\ddot{r}_y = \dot{v}_y = \frac{f_t}{m} (\cos(\phi) \sin(\theta) \sin(\psi) - \sin(\phi) \cos(\psi)) \quad II \quad (4.63b)$$

$$\ddot{r}_z = \dot{v}_z = -g + \frac{f_t}{m} (\cos(\phi) \cos(\theta)) \quad III . \quad (4.63c)$$

The set of equations (4.63) is solved for the system input \mathbf{u} by using $I \cdot \sin(\psi) - II \cdot \cos(\psi)$ and $I \cdot \cos(\psi) + II \cdot \sin(\psi)$. That results in the intermediate result

$$\sin(\phi) = \frac{m (\ddot{r}_x \sin(\psi) - \ddot{r}_y \cos(\psi))}{f_t} \quad (4.64a)$$

$$\sin(\theta) \cos(\phi) = \frac{m (\ddot{r}_x \cos(\psi) - \ddot{r}_y \sin(\psi))}{f_t} . \quad (4.64b)$$

Together with the absolute value of f_t

$$f_t = m \left| \dot{\mathbf{v}} + g \mathbf{e}_{z,0} \right| , \quad (4.65)$$

the system inputs $\mathbf{u} = [\phi \quad \theta \quad f_t]^T$ can be expressed by the flat output \mathbf{r} and its first two derivatives by [2]

$$\phi = \text{asin} \left(\frac{\ddot{r}_x \sin(\psi) - \ddot{r}_y \cos(\psi)}{\sqrt{\ddot{r}_x^2 + \ddot{r}_y^2 + (\ddot{r}_z + g)^2}} \right) \quad (4.66a)$$

$$\theta = \text{asin} \left(\frac{\ddot{r}_x \cos(\psi) + \ddot{r}_y \sin(\psi)}{\sqrt{\ddot{r}_x^2 + \ddot{r}_y^2 + (\ddot{r}_z + g)^2} \cos \left(\text{asin} \left(\frac{\ddot{r}_x \sin(\psi) - \ddot{r}_y \cos(\psi)}{\sqrt{\ddot{r}_x^2 + \ddot{r}_y^2 + (\ddot{r}_z + g)^2}} \right) \right)} \right) \quad (4.66b)$$

$$f_t = m \sqrt{\ddot{r}_x^2 + \ddot{r}_y^2 + (\ddot{r}_z + g)^2} . \quad (4.66c)$$

The concept of the flatness-based exact feedforward linearisation is to use the second derivative of the flat output $\ddot{\mathbf{r}}$ as a virtual input $\boldsymbol{\nu}$, so that system (4.62) can be described by the linear system

$$\dot{\mathbf{r}} = \mathbf{v} \quad (4.67a)$$

$$\dot{\mathbf{v}} = \ddot{\mathbf{r}} = \boldsymbol{\nu} . \quad (4.67b)$$

The linear system (4.67) with the virtual input $\boldsymbol{\nu}$ is decoupled in the directions $\mathbf{e}_{x,0}$, $\mathbf{e}_{y,0}$ and $\mathbf{e}_{z,0}$. Thus, each independent subsystem can be written as

$$\underbrace{\begin{bmatrix} \dot{r}_\iota \\ \dot{v}_\iota \end{bmatrix}}_{\dot{\mathbf{x}}_\iota} = \underbrace{\begin{bmatrix} 0 & 1 \\ 0 & 0 \end{bmatrix}}_{\mathbf{A}} \underbrace{\begin{bmatrix} r_\iota \\ v_\iota \end{bmatrix}}_{\mathbf{x}_\iota} + \underbrace{\begin{bmatrix} 0 \\ 1 \end{bmatrix}}_{\mathbf{b}} \nu_\iota \quad (4.68)$$

where $\iota \in \{x, y, z\}$ indicates the subsystem for the corresponding direction. Further, the virtual input ν_ι is a combination of the feedforward of the desired trajectory $\ddot{r}_{\iota,d}$ and the control input of the linear controller $\nu_{\iota,c}$

$$\nu_\iota = \ddot{r}_{\iota,d} + \nu_{\iota,c} . \quad (4.69)$$

In the following, it will be distinguished between the vertical subsystem $\iota = z$ and the horizontal subsystem $\iota \in \{x, y\}$. The reason is that the flight tests were carried out using the state estimation of the complementary filter approach. This estimation approach does not provide state information of the horizontal velocity, so that the two subsystems need different approaches for the control of their trajectory error system. Moreover, the flight tests showed an additional dynamics between the tilt of the Hexacopter and the observed acceleration in the horizontal plane. This additional dynamics is only considered in the horizontal subsystem.

Vertical subsystem

The vertical subsystem $\iota = z$ is given by

$$\dot{\mathbf{x}}_z = \mathbf{A}\mathbf{x}_z + \mathbf{b}\nu_z \quad (4.70a)$$

$$\mathbf{y}_z = \mathbf{C}_z\mathbf{x}_z \quad \mathbf{C}_z = \begin{bmatrix} 1 & 0 \\ 0 & 1 \end{bmatrix} \quad (4.70b)$$

and the trajectory error to the desired trajectory $\mathbf{r}_{z,d} = [r_{z,d} \quad \dot{r}_{z,d}]^T$ results in

$$\boldsymbol{\varepsilon}_z = \mathbf{y}_z - \mathbf{r}_{z,d} . \quad (4.71)$$

The complementary filter estimation approach provides an estimation of the vertical position and velocity. Thus, the subsystem can be controlled by the linear state feedback control law

$$\nu_{z,c} = \mathbf{k}_z^T \boldsymbol{\varepsilon}_z . \quad (4.72)$$

The feedback gain \mathbf{k}_z can be determined by the use of Ackermann's formula [32]. This enables to set the eigenvalues λ_z of the closed-loop system to a desired value. The control of the vertical subsystem is illustrated in Figure 4.4

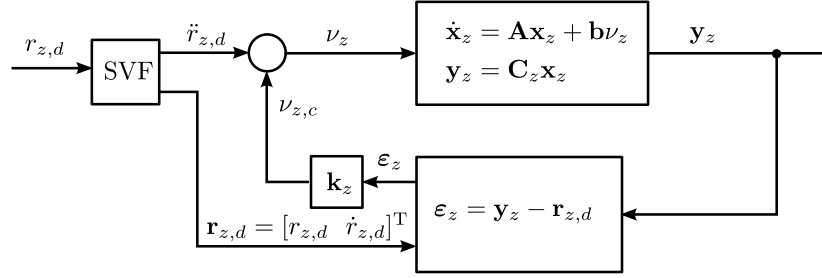


Figure 4.4: Linear control of the vertical subsystem.

Horizontal subsystem

In the model (4.62), the total thrust f_t acts in the direction of $\mathbf{e}_{z,B}$ and leads to an instant acceleration if the Hexacopter tilts to a side. During flight tests it was observed that this assumption does not hold for low altitude flights. A dynamics between the tilt of the Hexacopter and the acceleration in the corresponding horizontal direction was observed. It is assumed that this dynamics arises from an aerodynamic force acting in the horizontal plane that is caused by ground disturbances, but an exact physical interpretation is topic of future investigations. Due to safety reasons, all flight tests were carried out at low proximity to the ground. Thus, an evaluation at a height where no ground disturbances occur was not possible. To take into account this dynamics between the tilt of the Hexacopter and the resulting acceleration, as a first order low-pass was identified and included in the linear model (4.68). Therefore, the state vector \mathbf{x}_ι of the horizontal subsystem $\iota \in \{x, y\}$ expands by the horizontal acceleration a_ι to $\mathbf{x}_{e,\iota} = [r_\iota \ v_\iota \ a_\iota]^T$. The system equations of the expanded horizontal subsystem are given by

$$\dot{\mathbf{x}}_{e,\iota} = \mathbf{A}_h \mathbf{x}_{e,\iota} + \mathbf{b}_h \nu_\iota \quad (4.73a)$$

$$y_\iota = \mathbf{c}_h^T \mathbf{x}_{e,\iota} = r_\iota, \quad (4.73b)$$

with

$$\mathbf{A}_h = \begin{bmatrix} 0 & 1 & 0 \\ 0 & 0 & 1 \\ 0 & 0 & c_d \end{bmatrix}, \quad \mathbf{b}_h = \begin{bmatrix} 0 \\ 0 \\ c_d \end{bmatrix} \quad \text{and} \quad \mathbf{c}_h = \begin{bmatrix} 1 \\ 0 \\ 0 \end{bmatrix}, \quad (4.74)$$

where $c_d = -1.72$ is the pole of the first-order low pass dynamics. The flight tests were conducted with the complementary filter estimation. This estimation provides no information about the velocity in the horizontal plane. To damp the system, a controller based on observer feedback was designed with the Luenberger observer

$$\dot{\hat{\mathbf{x}}}_{e,\iota} = \mathbf{A}_h \hat{\mathbf{x}}_{e,\iota} + \mathbf{b}_h \nu_\iota + \mathbf{L}_h (\hat{y}_\iota - y_\iota) \quad (4.75a)$$

$$\hat{y}_\iota = \mathbf{c}_h^T \hat{\mathbf{x}}_{e,\iota} = \hat{r}_\iota, \quad (4.75b)$$

where \mathbf{L}_h is the observer gain. Again, \mathbf{L}_h is determined with the formula of Ackermann for all eigenvalues of the estimation error set to $\hat{\lambda}_\iota$. The trajectory error results in

$$\hat{\boldsymbol{\varepsilon}}_\iota = \hat{\mathbf{x}}_{e,\iota} - \mathbf{r}_{\iota,d}, \quad (4.76)$$

with the trajectory $\mathbf{r}_{\iota,d} = [r_{\iota,d} \ \dot{r}_{\iota,d} \ \ddot{r}_{\iota,d}]^T$. To account for model uncertainties, the controller is extended with an integral term

$$\dot{\varepsilon}_{\iota,I} = \hat{y}_{\iota} - r_{\iota,d} . \quad (4.77)$$

Thus, the state feedback controller for the horizontal subsystem reads as

$$\nu_{\iota,c} = \underbrace{\begin{bmatrix} \mathbf{k}_{h,c}^T & k_{h,I} \end{bmatrix}}_{\mathbf{k}_h^T} \begin{bmatrix} \varepsilon_{\iota} \\ \varepsilon_{\iota,I} \end{bmatrix} . \quad (4.78)$$

Again, the feedback gain \mathbf{k}_h is determined by the use of Ackermann's formula for all eigenvalues of the closed-loop system set to λ_{ι} . The control of the horizontal subsystem is illustrated in Figure 4.5

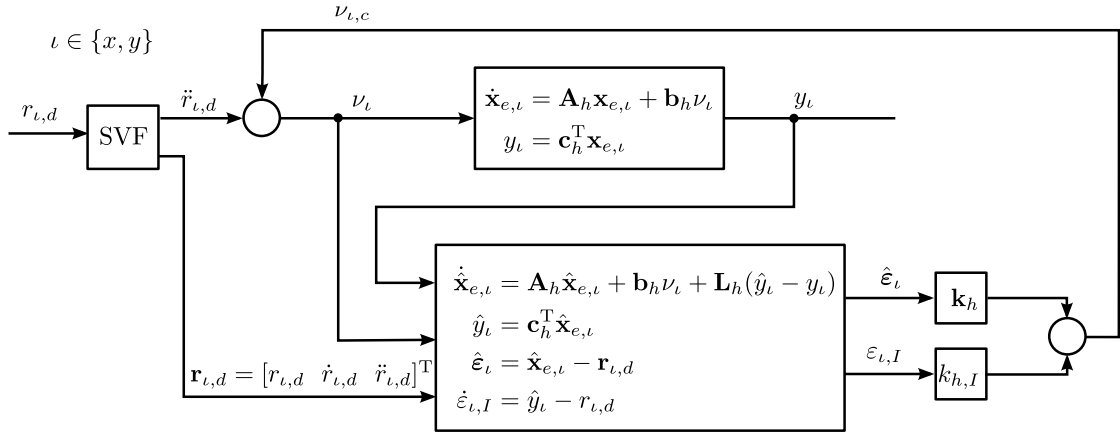


Figure 4.5: Linear control of the horizontal subsystem.

5 Simulation studies and experimental validation

In the following chapter, the previously derived EKF and the control strategy will be verified by means of simulation studies and experiments on the Hexacopter. As already mentioned in Section 4.4, the flight tests had to be carried out at low proximity to the ground due to safety reasons. During these low altitude flights, a dynamics between the tilt of the Hexacopter and the acceleration in the corresponding horizontal direction was observed, which is assumed to be caused by ground disturbances. This dynamics is not included in the model of the EKF as its physical explanation is not clear and the Hexacopter is intended to fly mainly at a height without ground disturbances. For these reasons, the EKF will be verified by a simulation of the complete model (3.48). The control strategy will be validated by two experiments. First, the attitude control will be verified separately by using a test bench. This test bench locks all degrees of freedom except for the rotation around the $\mathbf{e}_{x,B}$ axis. Thus, the attitude control of the roll and pitch angle can be treated separately. Second, the position control will be validated by means of a free-flight test using the complementary filter estimation approach for state estimation.

5.1 Extended Kalman filter

To validate the EKF, it is simulated with the complete model (3.48). The model is stabilized at the reference trajectories of the position $\mathbf{r}_d(t)$ and the yaw angle $\psi_d(t)$. The goal of the simulation is to evaluate the performance of the EKF. To this end, the simulated states are directly used for feedback control. Further, the vertical and horizontal subsystem of Section 4.4 will be treated equally and the state feedback controller (4.72) will be used for the subsystems $\iota \in \{x, y, z\}$. The SVF time constants T_f of the horizontal position reference signals $r_{x,d}(t)$ and $r_{y,d}(t)$ are set to a faster dynamics to allow for faster position changes which leads to higher values of the velocity \mathbf{v} and Euler angles ϕ . An additive noise corresponding to the noise characteristics of the sensors is used to simulate realistic measurements. All parameters used in the simulation are listed in Table A.7 in Appendix A.

The EKF was tuned by the following approach. First, the covariance matrix of the measurements

$$\mathbf{R} = \text{diag} \left(\sigma_{acc}^2, \sigma_{acc}^2, \sigma_u^2, \sigma_u^2, \sigma_u^2, \sigma_u^2 \right) \quad (5.1)$$

was set to the measured variance of the acceleration sensor $\sigma_{acc}^2 = 2.14 \cdot 10^{-4} \text{ (m/s}^2\text{)}^2$ and the measured variance of the ultrasonic sensors $\sigma_u^2 = 1.81 \cdot 10^{-4} \text{ m}^2$. Subsequently, the covariance matrix of the process noise was tuned to

$$\mathbf{Q} = 1 \cdot 10^{-4} \text{diag} (1, 1, 1000, 100, 100, 1000, 1, 1, 10) . \quad (5.2)$$

The first three diagonal entries of \mathbf{Q} correspond to the process noise of the position, the second three to the velocity, and the last three to the Euler-angles. The model of the EKF (4.22) does not include the ground effect. Thus, the deviation between the model of the EKF and the complete model were considered by high entries of $\mathbf{Q}(3, 3)$ and $\mathbf{Q}(6, 6)$. The remaining entries were tuned empirically. For the start values of the covariance matrix \mathbf{P} , the simulation was run once with the start value $\mathbf{P}_0 = \mathbf{E}$. The covariance matrix at the end of the simulation \mathbf{P}_{end} is then used as start value for all further simulations $\mathbf{P}_0 = \mathbf{P}_{end}$. For the simulation, initial errors of the estimated position $|\hat{\epsilon}_{r,0}| = 0.3 \text{ m}$, of the estimated velocity $|\hat{\epsilon}_{v,0}| = 0.1 \text{ m/s}$, and of the estimated Euler-angles $|\hat{\epsilon}_{\phi,0}| = 5^\circ$ were introduced.

Figure 5.1 shows the estimated state $\hat{\mathbf{x}}$ of the EKF in green and the simulated state in blue. The states which are available by direct measurement are displayed in red. It can be observed that after the initial error is decayed, the estimated states are a good representation of the simulated ones. Figure 5.2 shows the estimation error $\hat{\epsilon}_r = [\hat{\epsilon}_{r_x} \ \hat{\epsilon}_{r_y} \ \hat{\epsilon}_{r_z}]^T$ of the position \mathbf{r} , the estimation error $\hat{\epsilon}_v = [\hat{\epsilon}_{v_x} \ \hat{\epsilon}_{v_y} \ \hat{\epsilon}_{v_z}]^T$ of the velocity \mathbf{v} , and the estimation error $\hat{\epsilon}_\phi = [\hat{\epsilon}_\phi \ \hat{\epsilon}_\theta \ \hat{\epsilon}_\psi]^T$ of the Euler angles ϕ for the entire simulation on the left side and for the first 3 s on the right side. It can be seen that all estimation errors asymptotically go to zero in the first 20 s except for the estimation error of the vertical velocity $\hat{\epsilon}_{v_z}$. The error $\hat{\epsilon}_{v_z}$ decreases, but a constant yet small estimation error remains. The reason is that there is no direct measurement available for v_z and due to neglecting the ground effect in the EKF model it differs from the complete model. The estimation errors of the horizontal velocities increase before they start to decrease. This is caused by the start values of the Euler angles. According to the model, there is an acceleration in the horizontal plane if the Hexacopter is tilted causing a rise in the horizontal velocity. In the right part of Figure 5.2, a zigzagging of the position estimation error, the velocity estimation error, and the yaw angle estimation error is observable. This zigzagging is caused by the measurement update of the CD-EKF implementation. Here, the update step is performed at a lower frequency than the processing rate of the EKF.

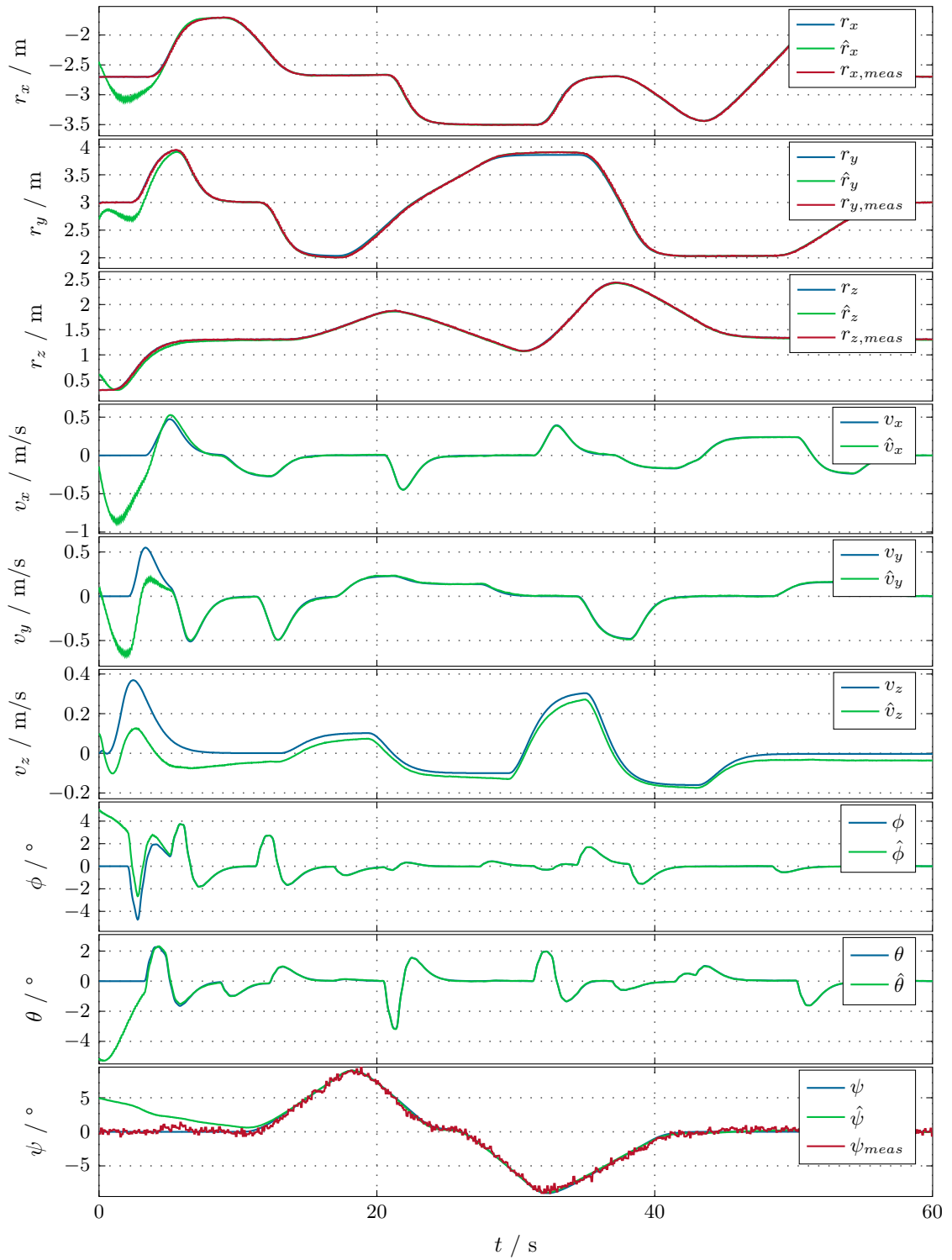


Figure 5.1: Estimated states of the EKF in comparison to the real states.

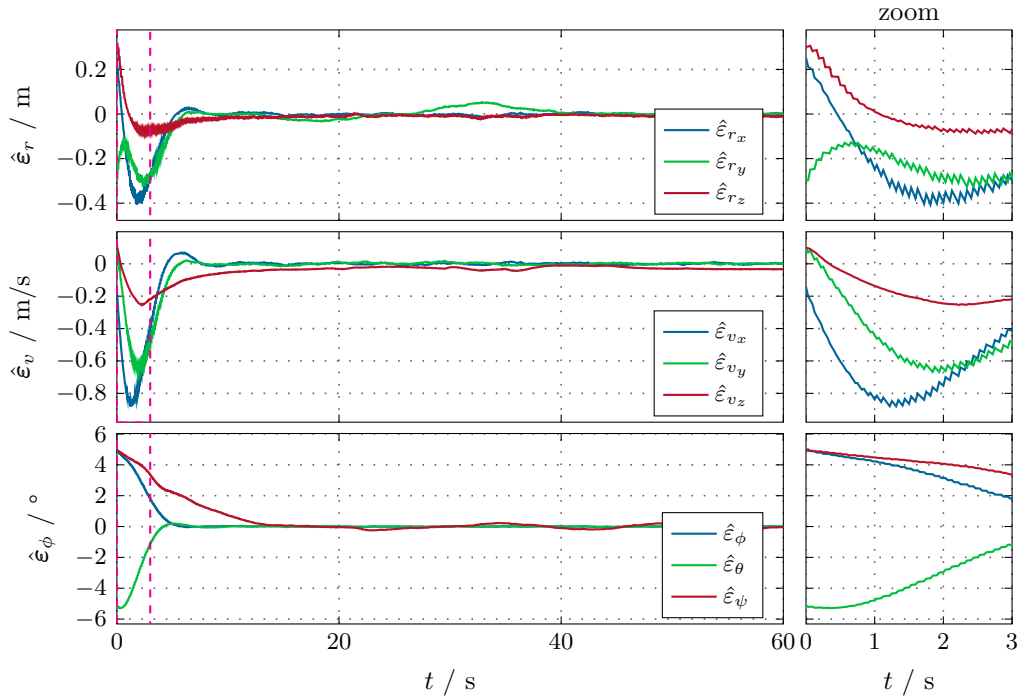


Figure 5.2: Illustration of the estimation errors of the EKF.

5.2 Attitude control

For the verification of the attitude control, a test bench was built which locks all degrees of freedom except for the rotation around the $\mathbf{e}_{x,B}$ axis. Thus, the dynamic system consists solely of two states, the roll angle ϕ and the rotation rate $\omega_{x,B}$ as shown in Figure 5.3. The Hexacopter is pivot-mounted on two opposite motor support booms with its rotational axis aligned to the CM. This allows to independently evaluate the controller of the roll angle.

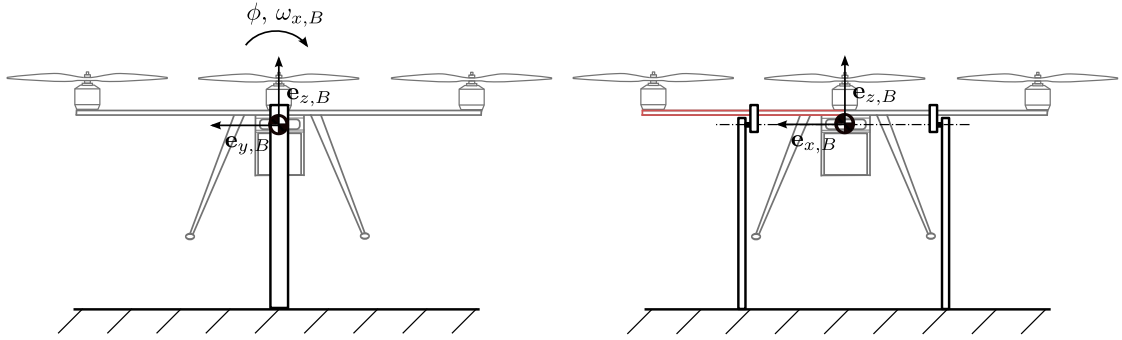


Figure 5.3: Schematic illustration of the test bench used for the attitude control verification.

For the experiment at the test bench, the parameter matrices (4.56) were set to $\mathbf{C}_p = \text{diag}(c_p, 0, 0)$ and $\mathbf{C}_d = \text{diag}(c_d, 0, 0)$. Here, the parameters which weight the errors of the locked rotational degrees of freedom are chosen as zero. The remaining control parameters of the control law (4.53) and (4.55) were empirically set to $c_p = 110$, $c_d = 30$ and $\gamma = 0.03$.

Figure 5.4 shows the step response of the roll control with the desired roll angle ϕ_d in blue and the roll angle ϕ measured by the IMU-intern EKF in green. Further, it shows the tracking error ε_ϕ between ϕ_d and ϕ , the estimated bias torque τ_0 , and the used motor controller inputs S_i for $i \in \{1, \dots, 6\}$. A step of 20° can be followed within 1 s. The error stays within 2° deviation from the desired value. The bias torque estimation is nearly constant at $\tau_0 = 0.3 \text{ N m}$.

Figure 5.5 is structured in the same way as Figure 5.4 and shows the reference tracking behavior of the roll control for a chirp signal from 0.1-1.5 Hz. The first deviation of the desired value is caused by the fixation of the Hexacopter before the experiment started. The desired signal can be followed without phase delay with a maximum error of approximately 3° . The maximum error appears at the turning points for higher frequencies. The bias torque estimation is not constant but stays within $0.3 \pm 0.1 \text{ N m}$.

Since the dynamics of the roll and pitch angle is the same, the same control parameters can be used. The control parameter concerning the yaw angle ψ cannot be tuned with this test bench. It was empirically tuned by a free-flight experiment and the entire parameter matrices of the attitude controller are obtained as

$$\mathbf{C}_p = \begin{bmatrix} 110 & 0 & 0 \\ 0 & 110 & 0 \\ 0 & 0 & 7 \end{bmatrix} \quad \text{and} \quad \mathbf{C}_d = \begin{bmatrix} 30 & 0 & 0 \\ 0 & 30 & 0 \\ 0 & 0 & 6 \end{bmatrix}. \quad (5.3)$$

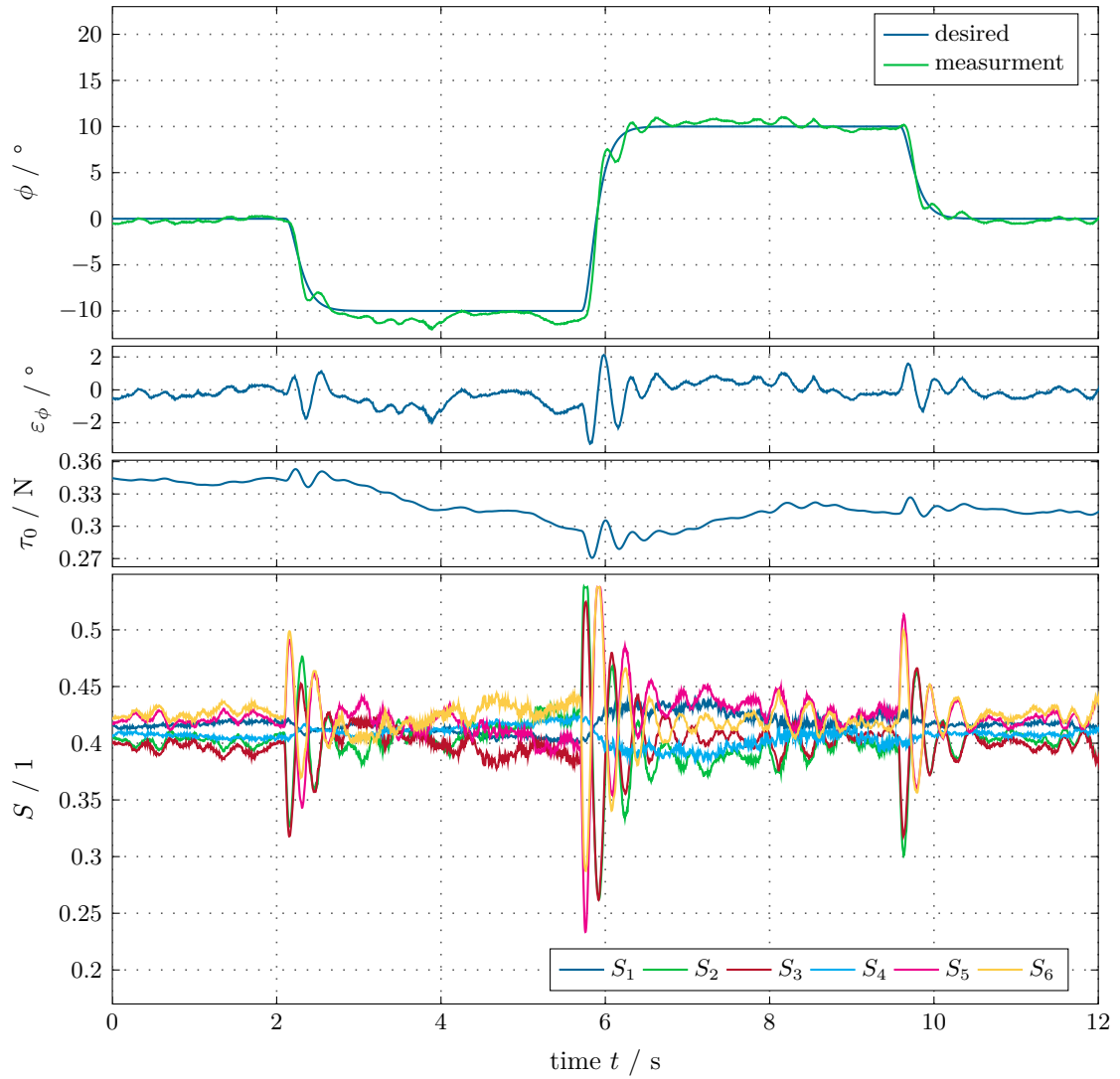


Figure 5.4: Step response of the roll angle.

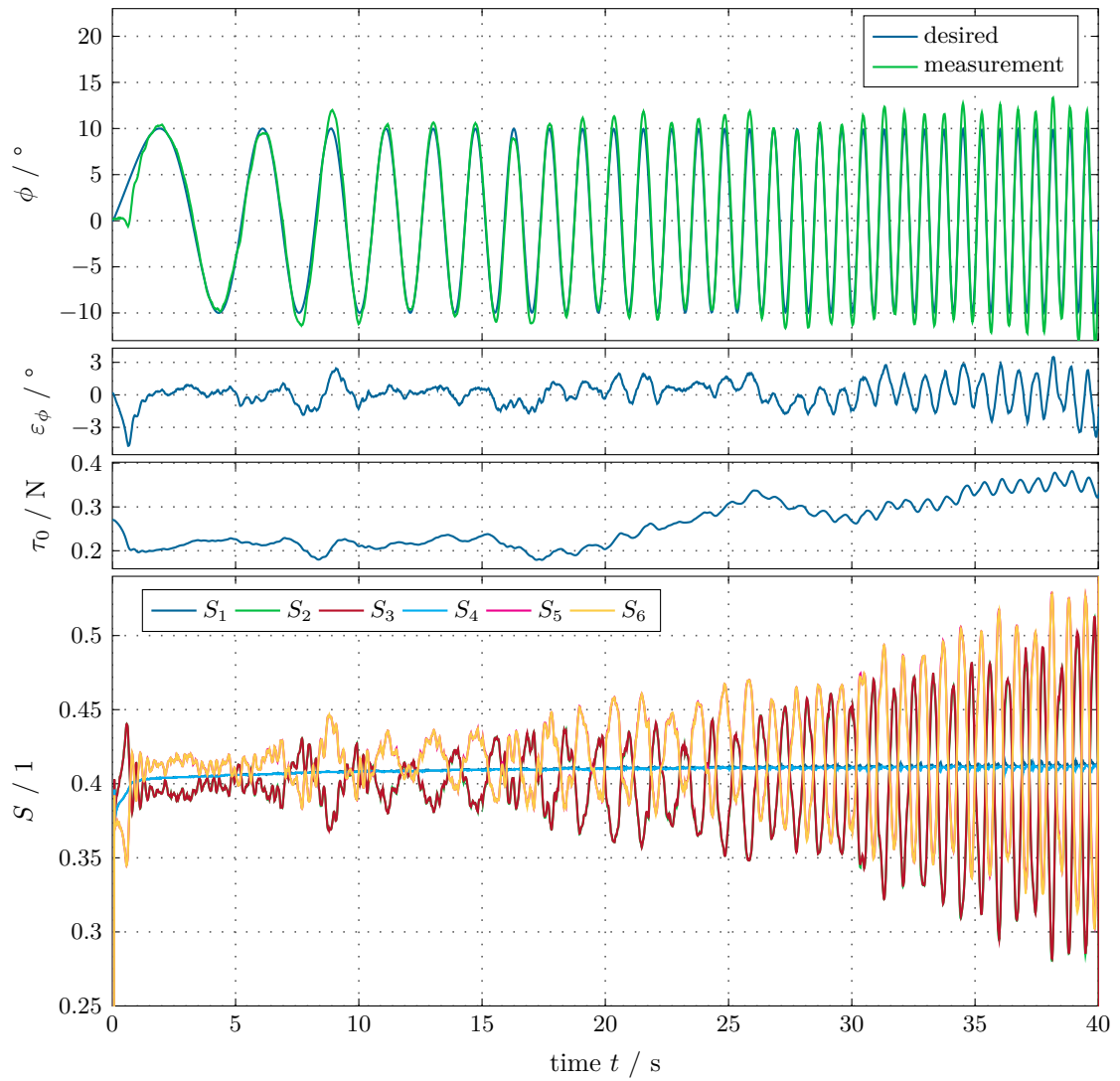


Figure 5.5: Reference tracking behavior of the roll angle for a chirp signal from 0.1-1.5 Hz.

5.3 Position control

The position control and the performance of the entire system is evaluated by a free-flight experiment. For safety reasons, the Hexacopter is connected to the floor with strings mounted on its legs as shown in Figure 5.6. This arrangement limits the flight height of the CM to approximately 0.5 m and the horizontal displacement to about 0.2 m. The safety arrangement is necessary because the ultrasonic sensors are not very reliable and occasionally deliver false measurements. These wrong position information can cause instability of the Hexacopter.

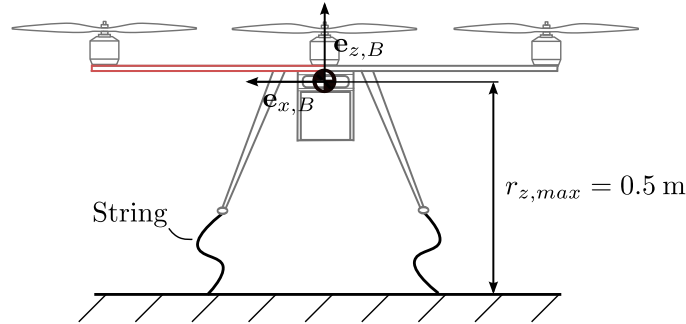


Figure 5.6: Safety arrangement for the free-flight experiment.

The parameters of the attitude control were set to the same values as for the test bench experiment in Section 5.2. The parameters for the position control were set empirically. The eigenvalues of the estimation error of the observer (4.75) are set to $\hat{\lambda}_i = -3$. The eigenvalues for the closed-loop system of the vertical subsystem (4.70) are set to $\lambda_z = -7$ and the eigenvalues for the closed-loop system of the horizontal subsystem (4.73) are set to $\lambda_\iota = -1.2$ for $\iota \in \{x, y\}$.

Figure 5.7 shows the results of the free-flight experiment. The measured position \mathbf{r} in comparison to the desired position \mathbf{r}_d and the control variables of the position control, i. e., the pitch and roll angle ϕ and θ and the total thrust f_t , as well as the yaw angle ψ are shown. The Euler angles of the attitude ϕ are also compared to their desired values ϕ_d . The desired value is shown in green and the measured value in blue. Further, the position error $\boldsymbol{\varepsilon}_r = [\varepsilon_{r_x} \ \varepsilon_{r_y} \ \varepsilon_{r_z}]^T$ between \mathbf{r}_d and \mathbf{r} as well as the attitude error $\boldsymbol{\varepsilon}_\phi = [\varepsilon_\phi \ \varepsilon_\theta \ \varepsilon_\psi]^T$ between ϕ_d and ϕ are illustrated in this figure. The vertical subsystem is well stabilized at the desired trajectory. The measured position of the horizontal subsystem follows the desired position with an oscillation around the desired value. This oscillation is assumed to be caused by the ground disturbances, which occur at low flight heights. However, the position error stays within approximately 0.1 m. The measured pitch and roll angles follow the desired value with an error below 2° , as also observed at the attitude test bench. The desired value of the yaw angle is set to 0° and its control parameters are not aggressively tuned. Its error stays between $\pm 5^\circ$. The desired total thrust f_t is nearly constant at approximately 34 N.

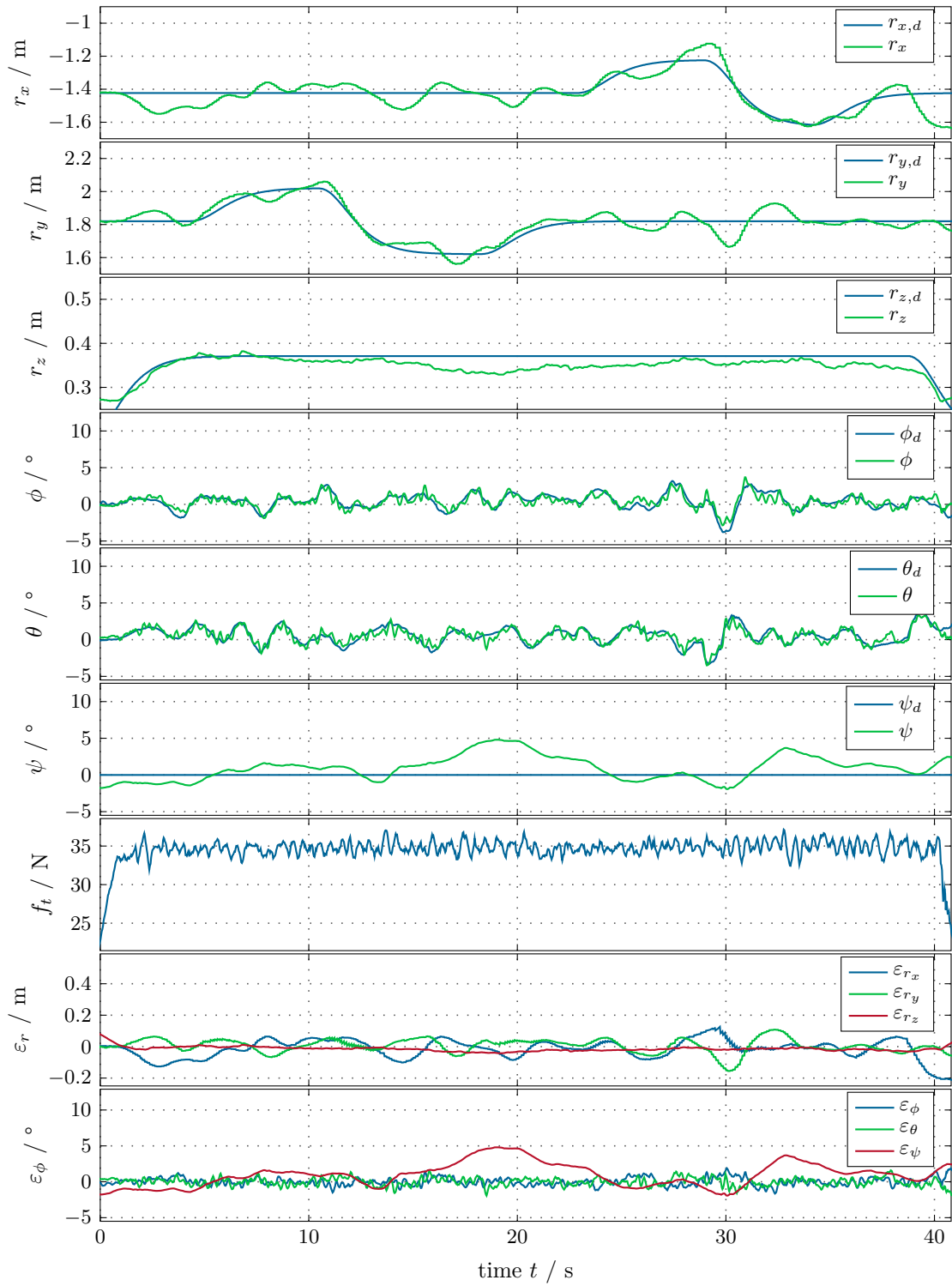


Figure 5.7: Results of the free-flight experiment.

6 Summary and Outlook

In the course of this thesis, a multicopter platform for rapid testing of different control algorithms was built. It is based on the commercially available *Mikrokopter Hexa XL* that is capable of lifting sufficient payload. The electronics mainly consists of a computer which performs the computation of the control algorithm and a microcontroller board which is used as gateway between the computer and all sensors and actuators. Ultrasonic sensors are used for position determination and an IMU for determination of the attitude. Further, a mathematical model of the Hexacopter was derived. The Hexacopter is assumed as a rigid body in free space and based on Newton's second law the dynamic equations of the Hexacopter were derived. The external forces acting on the Hexacopter are the rotor forces and secondary effects. As secondary effects the drag force, the ground effect and the gyroscopic effect of the rotors are considered. These effects result in an accurate model of the Hexacopter's dynamics as long as the Hexacopter translates slowly in the air. For fast dynamic movements, additional effects such as the blade flapping effect have to be considered. The motor controller generates a PWM signal of the battery voltage and uses the pulse wide as motor control input. To describe the rotor force, a static model that considers the motor controller input and the battery voltage was derived and identified. However, the rotor force depends on the angular velocity of the rotors. Thus, an underlying feedback controller which directly imposes the angular velocity of the rotors would improve the model accuracy.

For the stabilization of the Hexacopter at a reference position, a hierarchical control structure with non-linear control algorithms is applied. The inner attitude controller is based on a backstepping approach and controls the attitude of the Hexacopter to a desired reference signal. The outer position control based on a flatness-based feedforward linearization uses the desired roll and pitch angle of the attitude control and the total thrust as control variables. For state estimation, two different approaches are proposed. The first approach uses direct measurements in combination with complementary filters for some crucial states. It has the advantage that it does not need any information of the model and has just one parameter, which is intuitive to tune. The second approach is an EKF that uses the information of the model and the noise characteristics of the sensors, which improves the estimation results. During free-flight experiments at low heights, a dynamics between the tilt of the Hexacopter and the acceleration in the horizontal plane was observed, which is not included in the underlying model of the EKF. Thus, the complementary filter approach was used for these experiments. In this low flight height, the complementary filter approach works well as it does not need any model information. A possible improvement would be to develop a safety system, which allows the Hexacopter to fly freely in space and prevents damage in case of a crash. Such a safety system would allow to fly at higher altitudes where the EKF could be applied, which

would provide more accurate state information as has been shown in the simulation results.

The ultrasonic sensors which are used for position determination provide a position measurement with a good accuracy. However, they are not very reliable as they occasionally deliver false readings. Thus, for safety reasons the Hexacopter had to be secured by a string to the floor. This limits the flight to heights where the Hexacopter is still strongly influenced by ground disturbances. Moreover, the system is limited to an experimental setup with two adjacent flat walls, one to the front and one to the side of the Hexacopter. A possible improvement for the position determination would be a laser scanner or an external optical tracking system instead of the ultrasonic sensors.

A Additional tables

In this appendix, the electronic components, the model parameters, and the control parameters are listed. In particular, Table A.1 lists all field bus interfaces that are able to connect to the Cube via the SIB and all permanently connected devices. Table A.2 lists all components used on the SIB. Table A.3 lists the rotor parameters for the CFK air blade and Table A.3 for the PVC air blade. Table A.5 lists all mechanical parameters of the Hexacopter. Table A.5 lists all time constants of the SVF for the different reference signals of position and attitude control and Table A.5 provides all parameters used for the simulation of the EKF.

connected devices	SIB	unexploited interfaces	SIB	Cube direct
Sonar Sensors	4	I2C	1	1/-
IMU	1	UART	1	1/2
MC BLC	1	CAN	1	-
RC - Receiver	1	SPI	1	-
LED	1	Analog In	6	-
		GPIO	8	8/-

Table A.1: List of possible field bus interfaces that are able to connect to the Cube via the SIB and all permanently connected devices.

Label	Description	Company	Name
U1	Microcontroller	Microchip	dsPIC33EP512MU806
U2	IMU	Analog Devices	ADIS16480
U3	Serial to I2C gateway	NXP	SC18IM700
U4	Linetranceivers	Maxim	MAX13433EESD+
U5	Comperator	STMicroelectronics	TS3021
U6	Supply	Recom	R-783.3-1.0
U7	Supply	Recom	R-785.0-1.0
-	Ultrasonic Sensors	MaxSonar	HRLV-EZ1

Table A.2: List of the components on the SIB.

r_r	$165 \cdot 10^{-3}$	m	rotor radius
A_r	$85.5 \cdot 10^{-3}$	m^2	rotor area
c_T	$1.19 \cdot 10^{-4}$	$N s^2 / rad^2$	lumped rotor force parameter
C_T	$4.31 \cdot 10^{-2}$	-	dimensionless rotor thrust coefficient
c_Q	$2.88 \cdot 10^{-6}$	$N m s^2 / rad^2$	lumped rotor torque parameter
C_Q	$6.3 \cdot 10^{-3}$	-	dimensionless rotor torque coefficient
a_1	2.13	\sqrt{N}	rotor force model parameter
a_2	$1.2 \cdot 10^{-3}$	N/V	rotor force model parameter

Table A.3: Rotor parameters for the CFK air blade.

r_r	$165 \cdot 10^{-3}$	m	rotor radius
A_r	$85.5 \cdot 10^{-3}$	m^2	rotor area
c_T	$1.3 \cdot 10^{-4}$	$N s^2 / rad^2$	lumped rotor force parameter
C_T	$4.72 \cdot 10^{-2}$	-	dimensionless rotor thrust coefficient
c_Q	$3.29 \cdot 10^{-6}$	$N m s^2 / rad^2$	lumped rotor torque parameter
C_Q	$7.3 \cdot 10^{-3}$	-	dimensionless rotor torque coefficient
a_1	2.18	\sqrt{N}	rotor force model parameter
a_2	$1.3 \cdot 10^{-3}$	N/V	rotor force model parameter

Table A.4: Rotor parameters for the PVC air blade.

m	3.4	kg	mass
d	0.345	m	distance of a rotor to the CM
h	$77 \cdot 10^{-3}$	m	distance of a rotor hub to the CM
I_x	$8.91 \cdot 10^{-2}$	$kg m^2$	moment of inertia around $\mathbf{e}_{x,B}$
I_y	$8.64 \cdot 10^{-2}$	$kg m^2$	moment of inertia around $\mathbf{e}_{y,B}$
I_z	$14.14 \cdot 10^{-2}$	$kg m^2$	moment of inertia around $\mathbf{e}_{z,B}$

Table A.5: Mechanical parameters.

T_{f,r_x}	4.4	s	time constant of the SVF for the reference signal $r_{x,d}$
T_{f,r_y}	4.4	s	time constant of the SVF for the reference signal $r_{y,d}$
T_{f,r_z}	4.4	s	time constant of the SVF for the reference signal $r_{z,d}$
T_{f,r_ϕ}	$62.8 \cdot 10^{-3}$	s	time constant of the SVF for the reference signal $r_{\phi,d}$
T_{f,r_θ}	$62.8 \cdot 10^{-3}$	s	time constant of the SVF for the reference signal $r_{\theta,d}$
T_{f,r_ψ}	3.2	s	time constant of the SVF for the reference signal $r_{\psi,d}$

Table A.6: Parameters of the SVF for the different reference signals of position and attitude control.

T_a	$1.3 \cdot 10^{-3}$	s	sampling time
T_s	0.1	s	sampling time of the sonar sensors
N	6	-	number of rotors
μ_d	0.0167	1 /s	drag coefficient
λ_x	-1	-	eigenvalue of closed loop for the horizontal subsystem
λ_y	-1	-	eigenvalue of closed loop for the horizontal subsystem
λ_z	-7	-	eigenvalue of closed loop for the vertical subsystem
T_{f,r_x}	3	s	time constant for the SVF of the desired x -position
T_{f,r_y}	3	s	time constant for the SVF of the desired y -position

Table A.7: Model parameters for the EKF simulation.

Bibliography

- [1] R. Mahony, V. Kumar, and P. Corke, „Multirotor aerial vehicles: modeling, estimation, and control of quadrotor,“ *Robotics Automation Magazine, IEEE*, vol. 19, no. 3, pp. 20–32, Sep. 2012.
- [2] S. Formentin and M. Lovera, „Flatness-based control of a quadrotor helicopter via feedforward linearization,“ in *50th IEEE Conference on Decision and Control and European Control Conference (CDC-ECC)*, Orlando, Dec. 2011, pp. 6171–6176.
- [3] T. Madani and A. Benallegue, „Backstepping control for a quadrotor helicopter,“ in *IEEE/RSJ International Conference on Intelligent Robots and Systems (IROS)*, Beijing, Oct. 2006, pp. 3255–3260.
- [4] R. Leishman, J. Macdonald, R. Beard, and T. McLain, „Quadrotors and accelerometers: state estimation with an improved dynamic model,“ *Control Systems, IEEE*, vol. 34, no. 1, pp. 28–41, Feb. 2014.
- [5] A. Nishi and H. Miyagi, „Mechanism and control of propeller type wall-climbing robot,“ in *IEEE/RSJ International Conference on Intelligent Robots and Systems (IROS)*, vol. 3, Munich, Sep. 1994, pp. 1724–1729.
- [6] A. Albers, S. Trautmann, T. Howard, T. A. Nguyen, M. Frietsch, and C. Sauter, „Semi-autonomous flying robot for physical interaction with environment,“ in *IEEE Conference on Robotics Automation and Mechatronics (RAM)*, Singapore, Jun. 2010, pp. 441–446.
- [7] D. Lee and C. Ha, „Mechanics and control of quadrotors for tool operation,“ in *ASME Conference on Dynamics Systems and Control (DSC)*, Florida, 2012, pp. 177–184.
- [8] F. Forte, R. Naldi, A. Macchelli, and L. Marconi, „Impedance control of an aerial manipulator,“ in *American Control Conference (ACC)*, Montreal, Jun. 2012, pp. 3839–3844.
- [9] L. Marconi, R. Naldi, A. Torre, J. Nikolic, C. Huerzeler, G. Caprari, E. Zwicker, B. Siciliano, V. Lippiello, R. Carloni, and S. Stramigioli, „Aerial service robots: an overview of the airobots activity,“ in *2nd International Conference on Applied Robotics for the Power Industry (CARPI)*, Zürich, Sep. 2012, pp. 76–77.
- [10] S. Lupashin, M. Hehn, M. W. Mueller, A. P. Schoellig, M. Sherback, and R. D’Andrea, „A platform for aerial robotics research and demonstration: the flying machine arena,“ *Mechatronics*, vol. 24, pp. 41–54, 2014.
- [11] D. Brescianini, M. Hehn, and R. D’Andrea, „Quadrocopter pole acrobatics,“ in *IEEE/RSJ International Conference on Intelligent Robots and Systems (IROS)*, Tokyo, 2013, pp. 3472–3479.

- [12] F. Augugliaro, S. Lupashin, M. Hamer, C. Male, M. Hehn, M. Mueller, J. Willmann, F. Gramazio, M. Kohler, and R. D'Andrea, „The flight assembled architecture installation: cooperative construction with flying machines,“ *Control Systems, IEEE*, vol. 34, no. 4, pp. 46–64, Aug. 2014.
- [13] Q. Lindsey, D. Mellinger, and V. Kumar, „Construction with quadrotor teams,“ *Autonomous Robots*, vol. 33, no. 3, pp. 323–336, 2012.
- [14] J. C. Macdonald Jr, „Efficient estimation for autonomous multi-rotor helicopters operating in unknown, indoor environment,“ PhD thesis, Brigham Young University, Jul. 2012.
- [15] Ascending Technologies GmbH, *Asctec research line /// catalogue 2014*. [Online]. Available: http://www.asctec.de/downloads/public/AscTec-Research-Line_Catalogue.pdf (visited on 01/10/2014).
- [16] Mathworks, *Real-time execution in external mode*. [Online]. Available: <http://de.mathworks.com/help/rtwin/ug/simulink-external-mode.html> (visited on 12/17/2014).
- [17] S. Grzonka, G. Grisetti, and W. Burgard, „Towards a navigation system for autonomous indoor flying,“ in *IEEE International Conference on Robotics and Automation (ICRA)*, Kobe, May 2009, pp. 2878–2883.
- [18] K. R. Symon, *Mechanics*, 3. ed. Reading, Massachusetts: Addison-Wesley, 1971.
- [19] J. L. MacCauley, *Classical mechanics; transformations, flows, integrable, and chaotic dynamics*, 1. ed. Cambridge: Cambridge Univ. Press, 1997.
- [20] Konz M. and Rudolph J., „Quadrotor tracking control based on a moving frame,“ in *9th IFAC Symposium on Nonlinear Control Systems (NOLCOS)*, Toulouse, Sep. 2013, pp. 80–85.
- [21] R. Fischer, *Elektrische Maschinen*, 9. Überarb. und erw. Aufl. München: Hanser, 1995.
- [22] J. G. Leishman, *Principles of helicopter aerodynamics*. Cambridge: Cambridge University Press, 2002.
- [23] R. W. Prouty, *Helicopter performance, stability, and control*. Malabar, Florida: Krieger Publishing Company, 2005.
- [24] G. Calafiore and L. El Ghaoui, *Optimization Models*. Cambridge: Cambridge University Press, 2014.
- [25] R. M. Moses Bangura, „Nonlinear dynamic modeling for high performance control of a quadrotor,“ in *Australasian Conference on Robotics and Automation (ACRA)*, Wellington, 2012, pp. 1–10.
- [26] S. Bouabdallah, „Design and control of quadrotors with application to autonomous flying,“ PhD thesis, École Polytechnique Fédérale de Lausanne, 2007.
- [27] W. Kemmetmüller and A. Kugi, *Skriptum zur VO Regelungssysteme 1 (WS 2014)*, Automation and Control Institute (ACIN), TU Wien, 2014.

-
- [28] A.-J. Baerveldt and R. Klang, „A low-cost and low-weight attitude estimation system for an autonomous helicopter,“ in *IEEE International Conference on Intelligent Engineering Systems (INES)*, Budapest, Sep. 1997, pp. 391–395.
 - [29] F. Rinaldi, „Automatic control of a multicopter,“ PhD thesis, Polytechnic University of Turin, 2014.
 - [30] J. Macdonald, R. Leishman, R. Beard, and T. McLain, „Analysis of an improved IMU-based observer for multicopter helicopters,“ *Journal of Intelligent & Robotic Systems*, vol. 74, no. 3-4, pp. 1049–1061, 2014.
 - [31] A. Kugi, *Skriptum zur VO Regelungssysteme 2 (SS 2014)*, Automation and Control Institute (ACIN), TU Wien, 2014.
 - [32] A. Kugi, *Skriptum zur VU Automatisierung (WS 2014)*, Automation and Control Institute (ACIN), TU Wien, 2014.

Eidesstattliche Erklärung

Hiermit erkläre ich, dass die vorliegende Arbeit gemäß dem Code of Conduct – Regeln zur Sicherung guter wissenschaftlicher Praxis (in der aktuellen Fassung des jeweiligen Mitteilungsblattes der TU Wien), insbesondere ohne unzulässige Hilfe Dritter und ohne Benutzung anderer als der angegebenen Hilfsmittel, angefertigt wurde. Die aus anderen Quellen direkt oder indirekt übernommenen Daten und Konzepte sind unter Angabe der Quelle gekennzeichnet. Die Arbeit wurde bisher weder im In- noch im Ausland in gleicher oder in ähnlicher Form in anderen Prüfungsverfahren vorgelegt.

Vienna, April 2015

Michael Buder